Atom probe reconstruction with a locally varying tip shape

Von der Fakultät für Chemie der Universität Stuttgart
zur Erlangung der Würde eines Doktors der
Naturwissenschaften (Dr. rer. nat.) genehmigte Abhandlung

Vorgelegt von
Daniel Beinke
aus Herford

Hauptberichter:	**Prof. Dr. Dr.h.c. Guido Schmitz**
Mitberichter:	**Prof. Dr. Dr.h.c. Siegfried Schmauder**
Vorsitzender:	**Prof. Dr. Joris van Slageren**

Tag der mündlichen Prüfung: **14.01.2020**

Institut für Materialwissenschaft der Universität Stuttgart

– 2019 –

Contents

Abbreviations

APT	Atom probe tomography
FIM	Field ion microscopy
MOSFET	Metal-oxide-semiconductor field-effect transistor
FinFET	Fin Field-effect transistor
FEV	Field evaporation
FOV	Field-of-view

List of Figures

Zusammenfassung

Diese Arbeit beschäftigt sich mit der Entwicklung eines neuartigen Algorithmus zur Rekonstruktion von Messdaten in der Atomsondentomographie. Ziel ist es, die bekannten Schwierigkeiten des herkömmlichen und auf dem Gebiet der Atomsondentomographie weit verbreiteten Algorithmus zu überwinden. Diese Schwierigkeiten treten insbesondere in Fällen inhomogener Spitzenstrukturen (d.h. verschiedene Atomspezies mit verschiedenen Verdampfungsfeldern) auf. Außerdem soll der Algorithmus einfach anzuwenden und hinreichend schnell sein, sodass die Anwendung auf experimentelle Datensätze mit einer typischen Größe von einigen Millionen gemessenen Ionen möglich ist.

Die ursprüngliche Idee für den neuen Algorithmus basiert auf der bereits bestehenden Möglichkeit, ein komplettes Atomsonden-Experiment auf einer realistischen Längenskala zu simulieren. Ein bereits bestehendes Simulationspaket erlaubt die sukzessive Feldverdampfung mit anschließender Berechnung einer realistischen Trajektorie für jedes Ion, welche von der Spitzenoberfläche bis zum Detektor in einigen Zentimetern Entfernung verläuft. Das grundlegende Konzept dieses Simulationsprogramms erlaubt es außerdem, die simulierte Feldverdampfung umzukehren. Diese Umkehrung entspricht einer Rekonstruktion des Spitzenvolumens.

Dabei wird das gemessene Spitzenvolumen in umgekehrter Reihenfolge verglichen mit der Verdampfung, also beginnend mit spät detektierten Ionen, rekonstruiert. In einem ersten Schritt wird dieses Konzept am Beispiel einiger charakteristischer Spitzen mit teilweise stark unterschiedlichen Verdampfungsfeldern der involvierten Spezies getestet. Dabei arbeitet der Algorithmus zunächst ausschließlich auf einem festen Gitter. Dies hat zur Folge, dass in jeden Schritt der Rekonstruktion nur bestimmte Gitterplätze als mögliche Positionen für ein detektiertes Atom in Frage kommen.

Im zweiten Schritt wird die Beschränkung auf ein festes Gitter fallen gelassen. Hierdurch nähert man sich einer realistischen Situation der Auswertung experimenteller Daten an, da im Allgemeinen die Gitterstruktur bzw. deren Orientierung a-priori nicht bekannt ist. Dabei stellt sich heraus, dass der Algorithmus sehr instabil gegenüber kleinen Ungenauigkeiten bzgl. der Platzierung einzelner Atome ist. Um die Stabilität zu erhöhen, wird daher ein interatomares Wechselwirkungspotenzial in die Berechnung einbezogen. Dieses dient als Filter, welcher nur solche Positionen auf der momentanen Spitzenoberfläche zulässt, welche

eine hinreichend große Anzahl an direkten Nachbaratomen aufweisen. Mit Hilfe des Wechselwirkungspotenzials kann der Rekonstruktionsalgorithmus deutlich stabilisiert werden. Die Ergebnisse für eine Detektionseffizienz von 100% erscheinen vielversprechend, jedoch zeigt sich bei einer Reduzierung der Detektionseffizienz ein nicht zu vernachlässigender Einfluss auf die Qualität der Rekonstruktion.

Als Reaktion auf diese Beobachtung, wird in einem dritten Schritt ein neuer Algorithmus entwickelt, welcher auf die Trajektorienberechnung verzichtet. Hierdurch soll der Algorithmus sowohl stabiler als auch schneller werden. Der neue Ansatz setzt zunächst eine Rotationssymmetrie der Spitzenstruktur bzgl. der Spitzenachse voraus. Der entscheidende Vorteil dieser Technik ist die Fähigkeit, die Form der Spitzenoberfläche direkt aus der lokalen Dichte der detektierten Ionen zu extrahieren. Dies ist ein entscheidender Fortschritt im Gegensatz zur herkömmlichen Rekonstruktionsmethode, da diese eine konstante halbkugelförmige Spitzenform voraussetzt.

Der neue Algorithmus wird an verschiedenen simulierten, jedoch realistischen Spitzenstrukturen getestet. Diese Teststrukturen enthalten entweder eine kugelförmige Ausscheidung oder eine planare Schicht mit einem stark unterschiedlichen Verdampfungsfeld im Bezug auf die umgebende Matrix. Die mit der neuen Technik verbundenen Verbesserungen hinsichtlich der Rekonstruktion werden durch direkten Vergleich mit der konventionellen Methode herausgearbeitet. Es zeigt sich eine enorm verbesserte Rekonstruktion der sphärischen Ausscheidungen bei stark unterschiedlichen Verdampfungsfeldern (44% bzw. 56%) und außerdem eine wesentlich konstantere Dicke der rekonstruierten Schichtstruktur.

Zusätzlich wird durch eine leichte Modifikation der Technik eine enorme Verbesserung hinsichtlich der Homogenität der Atomdichte erzielt. Während ohne diese Modifikation die Atomdichte noch starken Schwankungen unterliegt, lassen sich diese Schwankungen beeindruckend homogenisieren, wenn die Spitzenoberfläche nicht wie üblich als starres Gebilde behandelt wird, sondern sich einzelne Teile der Oberfläche unabhängig voneinander entwickeln dürfen.

Schließlich wird dieser neue Ansatz für die Rekonstruktion auf den allgemeinen Fall einer Spitzenstruktur ohne Rotationssymmetrie erweitert. Dabei bleibt die grundsätzliche Idee der Extraktion der Oberflächenform der Spitze aus der lokalen Dichte gemessener Ionen auf dem Detektor erhalten. Entscheidend für diesen letzten Entwicklungsschritt ist die Verknüpfung der Detektordichte mit der gaußschen Krümmung der Spitzenoberfläche. Ein iteratives Verfahren ermöglicht in diesem Fall die Einstellung der gewünschten Krümmung an verschiedenen Stellen der Spitzenoberfläche, woraus sich schließlich eine zufriedenstellende Beschreibung der Spitzenform ergibt. Das Konzept wird an einem ausgesuchten simulierten Datensatz getestet und diskutiert.

Abstract

In this thesis, a new approach for the reconstruction of data taken from an atom probe tomography experiment is presented. The goal of the study is to develop an algorithm, which is able to overcome well-known drawbacks of the conventional reconstruction technique, mainly caused by local magnification effects. At the same time, the algorithm should be easy to use and also fast enough, so that it might be routinely used as an improved alternative to the established reconstruction technique.

The idea is based on the already existing possibility to simulate an entire atom probe experiment on a realistic length. Since the successive calculation of ion trajectories starting at the emitter surface and hitting the detector after a flight of a few centimeters can be realized, the concept is designed to invert the field evaporation process by making use of this trajectory calculation. To this end, the detected emitter volume needs to be rebuilt from the bottom to the top, which is an important difference compared to the conventional technique.

In a first test, this inversion of the simulated experiment is demonstrated for a few prominent example cases. The decisive criterion for the positioning of an atom at a specific lattice site on the current emitter surface is the accordance of the impact position of the corresponding calculated trajectory with the measured coordinates on the detector. For every possible surface position, first an ion trajectory is calculated and its detector impact position is compared to the measured impact position. Finally, the best-matching trajectory defines the reconstruction coordinates.

The approach is performed for some prominent example emitter structures with strongly varying evaporation fields of the involved material, which is known for causing tremendous artifacts in the reconstruction derived by the standard technique. In this first attempt, the algorithm is restricted to a rigid lattice, which means that detected atoms can only be positioned at sites belonging to the former lattice of the emitter.

In a second step, the restriction to a rigid lattice is dropped. In this way, the reconstruction algorithm describes a more realistic scenario, since the exact lattice structure and its orientation might be unknown in the majority of experiments. The possibilities and limitations of the approach are discussed. It is found that an additional criterion for the determination of the reconstruction coordinates is needed in this case, since the algorithm is

very sensitive to the misplacement of atoms. The stability can be significantly improved by the consideration of an inter-atomic potential, which acts as a filter that exclusively allows surface sites with a sufficiently high amount of neighbor atoms. For a perfect detector efficiency the algorithm yields promising results, but a decrease of the efficiency towards realistic values gives rise to artifacts.

As a consequence of these numerical experiments, a new concept has been developed, which neglects the consideration of exact ion trajectories in order to make the algorithm more stable and fast. This third approach assumes rotational symmetry for the investigated emitter volume. An absolutely new characteristic of the technique is the capability to extract the shape of a field emitter directly from the observed pattern of ion impacts on the detector. This feature is a very important difference to the conventional technique, which assumes a constant spherical emitter shape. To the best of the authors knowledge, such a technique with this capability did not exist before. The promising features are demonstrated for several simulated but nevertheless realistic emitter structures. The improved quality of the reconstruction that can be achieved by the application of the here developed technique is shown by direct comparison to the result of the established reconstruction approach.

The impressive benefits are illustrated for relevant emitter structures containing either precipitates or layers of different materials with strongly varying evaporation fields (44% or 56% relative variation). In addition, a simple modification of the technique is described, which yields homogenized atomic densities in the reconstructed volumes. Without this modification, the emitter surface is treated like a rigid curved plane, which is shifted upwards with every reconstructed atom during reconstruction. Once the surface is no longer considered to be rigid, individual parts can be lifted separately, yielding a significantly homogenized atomic density.

Finally, the new concept of shape extraction is extended for the application to arbitrary emitter structures. The main idea of extracting the information about the emitter shape from the local density of measured events on the detector is maintained. In order to extend the approach to the application to structures without rotational symmetry, a relation between the local density of events on the detector and the Gaussian curvature on the emitter surface is derived. With the help of an iterative finite difference method, the Gaussian curvature at several positions on the tip surface is set. Consequently, a reasonable description of the emitter surface can be obtained and the reconstruction of an arbitrary data set can be performed. The concept is tested and discussed for a simulated example emitter structure.

Chapter 1.

Introduction

The development of high resolution microscopy techniques has been one of the most influential contributions to modern materials science. Standard techniques like transmission electron microscopy (TEM) or scanning electron microscopy (SEM) have enabled researchers to gain a steadily increasing understanding of complex solid state reactions at the micro- or even nanoscale. Among these well-established microscopy tools, atom probe tomography (APT) can be seen as a unique technique with very interesting key properties.

Since basically all other microscopy approaches exclusively deliver information about the surface and its immediate vicinity, APT is a very exceptional tool because it also gives access to information about the bulk of the investigated materials. Due the permanent field evaporation of the atom probe specimen, former bulk regions automatically appear at the surface at some point of the experiment and can therefore be accessed.

In the beginning, the range of possible materials for APT investigations was limited to metallic specimens, since a sufficiently large electric conductivity was required. Major improvements of the experimental setup, namely the introduction of a laser-assisted field evaporation [1, 2], drastically changed this situation. In addition, the amount of recorded data was increased and also the operation time has been massively reduced. Nowadays, the range of materials contains semiconductors, insulators and composite materials [3]. There is also a large interest in the analyses of nanoelectronic devices (Metal-oxide-semiconductor field-effect transistor (MOSFET) and Fin Field-effect transistor (FinFET) devices) [4–6].

Beside the many promising instrumental features of APT, characteristic drawbacks of the technique still exist. The most important part of an atom probe experiment is the *reconstruction* of the analyzed volume from the measured data set. Since the middle of the 1990's, the common reconstruction approach has only slightly been improved. Well-known artifacts in the reconstructed emitter volume, mainly caused by *local magnification effects*, still could not be sufficiently overcome. In order to deal with these challenges, the understanding of the dynamic development of the shape of the specimen apex has been improved with the help of numerical simulations of field evaporation (FEV) on

a realistic length scale [7]. The strong influence of largely varying thresholds in the required evaporation field, necessary to induce field evaporation, on the emitter shape could impressively be observed in these simulations.

The possibility to simulate an entire atom probe experiment also gives rise to the development of improved reconstruction algorithms. Since in the case of a simulated atom probe analysis the former volume is perfectly known before a simulation, any kind of newly designed reconstruction approach can immediately be evaluated by comparing the initial tip volume with the result of the reconstruction of the simulated data set.

Thanks to the previous work by Oberdorfer et al. [8], which enables the user to calculate realistic ion trajectories starting from arbitrarily shaped specimen surfaces, the idea of including the calculation of such ion trajectories in the reconstruction has led to this work. In addition to the trajectory calculation, the range of emitter structures that can be simulated is no longer restricted to simple cubic lattices, as it has been in previous attempts [9, 10]. The examined structures can contain an arbitrary amount of different atomic species with potentially strongly varying evaporation fields, which allow the investigation of the capability of the reconstruction tool to deal with such challenging conditions.

Following a brief introduction into the principle of APT in chapter 2, the development of an improved reconstruction approach is presented. The ultimate goal of this work is to find a new concept for the reconstruction of atom probe data, which can routinely be used as an alternative to the conventional reconstruction technique.

The concept of a completely new reconstruction technique, which is intended to rebuild the former volume of the atom probe tip from the bottom to the top based on the trajectory calculation of field-evaporated ions is outlined in section 3.1. In a first step towards a new reconstruction tool, this idea is tested on a rigid lattice for several characteristic emitter structures. The concept has been published in [11]. In order to make this technique applicable to realistic cases, this idea is further enhanced to work without a predefined lattice in section 3.2. The advantages and limitations of the designed algorithm are discussed and necessary conclusions are drawn. As a consequence of the observed limitations, the algorithm needs to be made more robust against the inevitable influence of missing information caused by the limited detection efficiency, which is still an issue of modern detectors.

To this end, an alternative reconstruction approach that is more robust against the loss of information is presented in chapter 4 and 5. First, an improved technique exclusively designed for the reconstruction of emitter structures with rotational symmetry is introduced in chapter 4. The concept behind this method has been published in [12]. This technique is able to identify the emitter shape during field evaporation by simply taking into account the local density of measured events on the detector. This feature can be seen as one of the key

improvements compared to the commonly used reconstruction technique. In section 4.1.3 and 4.1.5, the promising results of this technique are presented.

Finally, the remaining requirements for a "complete" reconstruction approach, applicable to arbitrarily shaped field emitters, are discussed in chapter 5. The final concept for a versatile reconstruction technique, based on the idea of deriving the emitter shape from the local density of detected events on the detector, is presented in section 5.1. Within the scope of this work, an article describing the concept has been submitted [13].

Chapter 2.

Atom Probe Tomography

2.1. The principle of atom probe tomography

In this chapter, the basic principle of APT will be introduced. Atom probe tomography is a microscopy technique, which images field-evaporated ions from the specimen surface on a position sensitive detector. The ultimate goal of an atom probe experiment is the generation of a three-dimensional map of the former tip volume, which contains chemical information. The technique has first been introduced by Erwin Müller [14] and can be seen as a further development of *field ion microscopy* (see section 2.1.1) [15]. Field evaporation stands for the field-induced removal of individual atoms from the surface of the investigated material (further details are given in section 2.1.2). In order to trigger the emission of an ion, very high electric fields are required. They need to be in the order of several tens of volts per nanometer. Those extraordinary high field strengths can only be achieved by reducing the dimension of the specimen. Consequently, an atom probe specimen is a very sharp needle-shaped tip with a radius in the range of $10 - 100\,\mathrm{nm}$. The necessary electric field is finally achieved by applying a base voltage of $3 - 15\,\mathrm{kV}$ between the tip and the detector. In classical APT, this base voltage is further supported by short voltage pulses, each one finally inducing the triggered field evaporation of individual atoms. Later, laser-pulse-assisted APT was introduced [1, 16], which gave access to the investigation of a much wider range of materials.

In section 2.1.1 an overview on the APT predecessor field ion microscopy is given. Subsequently, the process of field evaporation is further described in section 2.1.2 and finally the basic principle of APT is introduced in section 2.1.3. For any further detailed information, the reader is referred to some of the most commonly known textbooks [17–21].

2.1.1. The Field Ion Microscope

In field ion microscopy, which was first introduced by Bahadur and Müller [22], the surface of a charged needle-shaped metallic specimen is imaged on a phosphor screen or nowadays on a detector consisting of micro-channel-plates combined with an imaging screen. The ions are formed by ionizing neutral *imaging gas* atoms. For the imaging gas, which is filled into the chamber prior to the experiment, typically He or Ne is used. The tip is cooled down to a cryogenic temperature in the range of $20 - 60\,\mathrm{K}$. The field-induced ions starting at the specimen surface are accelerated towards the detector and generate a characteristic pattern, which provides a magnified image of the surface with detailed information about the crystallography. The ionization is achieved by applying a high positive voltage in the range of several kilovolts to the specimen/tip. In order to achieve an ion image of sufficient quality, a certain voltage, the so-called *best image voltage* (inducing the *best image field* respectively) is applied. In figure 2.3, the influence of the applied voltage can be seen for the example of a tungsten tip. The quality of the observable image for an applied voltage of 12 kV in figure 2.3b), appears to be much better, than the image quality achieved with a voltage of 8.2 kV (see figure 2.3a)).

Other experiments have also shown that the quality of a FIM image is highly dependent on the applied voltage [23]. Due to the small tip radius, extraordinary high fields ($\sim$ V/nm) are formed in close vicinity of the tip surface. The process of ionization starts with the polarization of image gas atoms, which is caused by the presence of the electric field. Since the field is strongly inhomogeneous, the polarized atoms (light blue in figure 2.2) experience a force, which initiates the atoms to approach the charged tip surface. Once the atom has reached a certain distance to the tip surface, it accommodates to the temperature of the tip by a few hopping steps on the surface until it finally attaches to the emitter. At this point, an electron might be lost to the specimen via a tunneling process. The energy barrier that has to be overcome in this tunneling process was described by Gomer [24]. For metals, the critical distance d_{crit} for ionization between tip and gas atom depends on the work function Φ_0 of the tip material, the strength E of the present electric field and the ionization energy E_I of the gas atom (see figure 2.1):

$$d_{crit} = \frac{E_I - \Phi_0}{e\,E}. \tag{2.1}$$

Once the ionization has taken place, the positively charged ions are strongly repelled by the tip surface and consequently accelerated towards the phosphor screen (see figure 2.2). On the screen, the hitting ions produce a pronounced contrast in the magnified image of the tip surface. This contrast stems from the considerably large difference in the electric

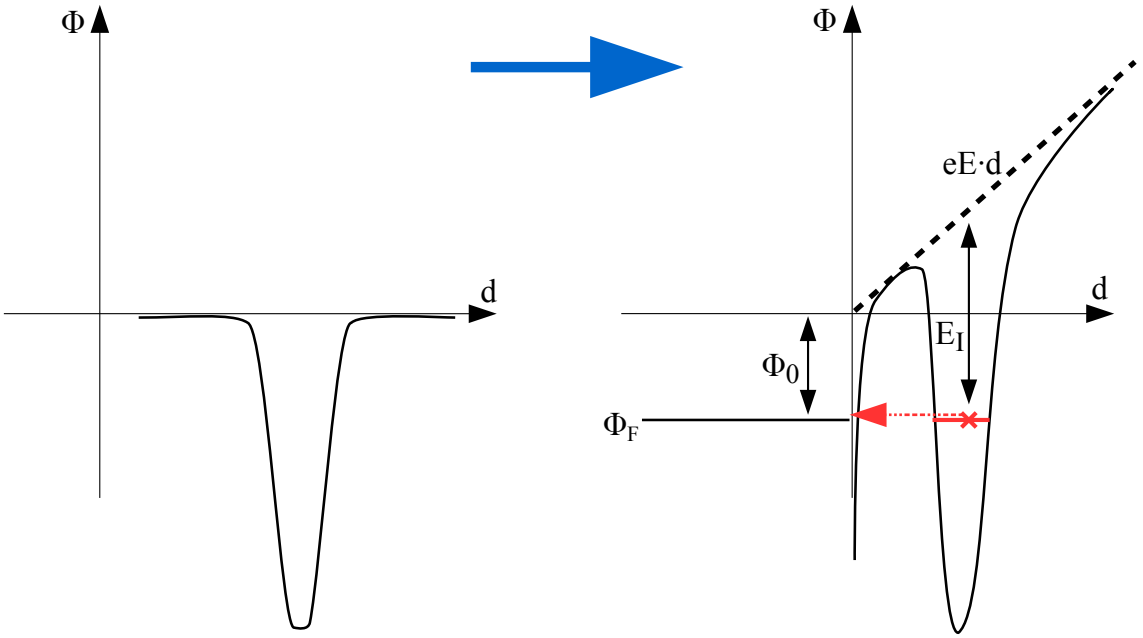

Figure 2.1.: Ionization of an image gas atom by tunneling. On the left, the potential well of an electron belonging to an image gas atom without an external field is shown. Once the image gas atom approaches a charged surface, the potential well bends and an energy barrier with a finite width between the charged surface and the potential well is formed (plot on the right). Electrons belonging to the image gas atom might be able to tunnel through this barrier (red arrow) and occupy an energy level above the Fermi level Φ_F, if its distance to the surface matches the critical distance d_{crit} according to equation (2.1).

field at the edges of crystallographic planes and in the center of such planes. At the edges of a crystallographic plane, the electric field is higher, which directly causes an increased probability for the ionization of gas atom. Therefore, these positions appear relatively bright in the resulting image on the screen, while places with a lower electric field appear darker.

A further increase of the field enables the possibility to even remove individual atoms located on the tip itself, rather than just ionizing gas ions in the vicinity. This process is called *field evaporation* and can be seen as the essential step towards APT.

2.1.2. Field evaporation

The term *field evaporation* (FEV) describes the field-induced removal and ionization of surface atoms of the needle-shaped tip. For FEV, the removed atoms have to belong to the bulk of the tip, which means the removal of adatoms is excluded. The general term that includes the removal of adatoms is *field desorption*. A very detailed theoretical work on this topic is given in [25]. The theory behind FEV is mainly intended to describe the field evaporation in metals.

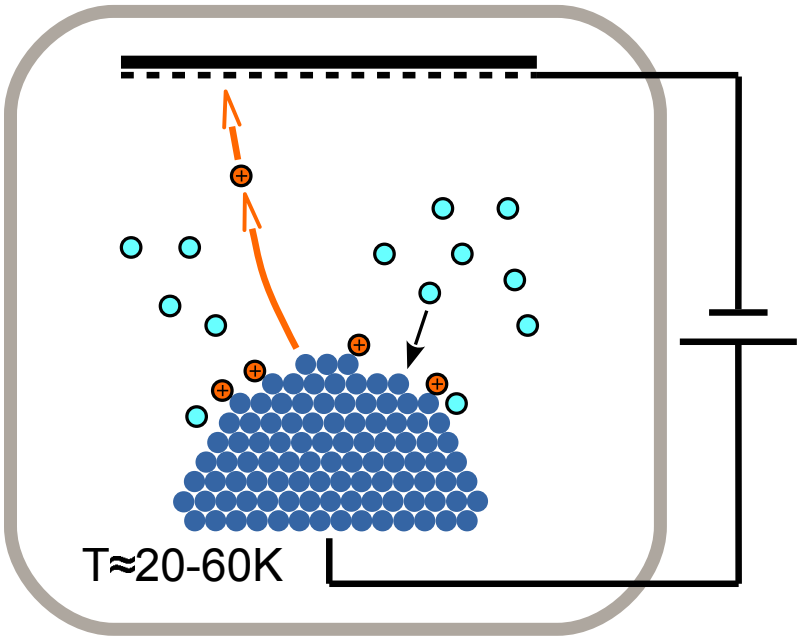

Figure 2.2.: Sketch of a field ion microscope. The imaging gas atoms (light blue) are approaching the tip surface (dark blue) due to the polarization in the electric field. In close vicinity to the surface, the gas atoms are ionized (orange) and repelled by the tip surface. As a result, they are accelerated towards the detector/phosphor screen on the top, yielding a magnified image of the tip surface morphology.

In order to trigger the FEV of a surface atom, very high electric fields in the range of several volts per nanometer are required. In APT, this can be achieved by the reduction of the specimen to a needle-shaped tip with an apex radius in the range of $10 - 100\,\mathrm{nm}$, as explained above.

The process of FEV can be assumed to be thermally activated for temperatures above 40 K. An atom has to overcome a certain energy barrier in order to leave the surface. The rate-constant k, which indicates the time for an atom to be field-evaporated on the surface (unit s^{-1}), can be described as

$$k = A \cdot e^{-\frac{Q(E)}{k_B T}}. \tag{2.2}$$

Here, the prefactor A is related to the vibrational frequency of an atom in its potential well, trying to escape. k_B is Boltzmann's constant and $Q(E)$ is the field dependent activation energy for field desorption. In addition, it is also possible for surface atoms that experience a sufficiently high field, to tunnel through the barrier of the potential energy well they are located in [25–27]. Below a temperature of approximately 40 K, experimental results [28] and theoretical predictions [29] have indicated that the tunneling process of the evaporating atom may become more important than the thermally activated process for light atoms.

(a)

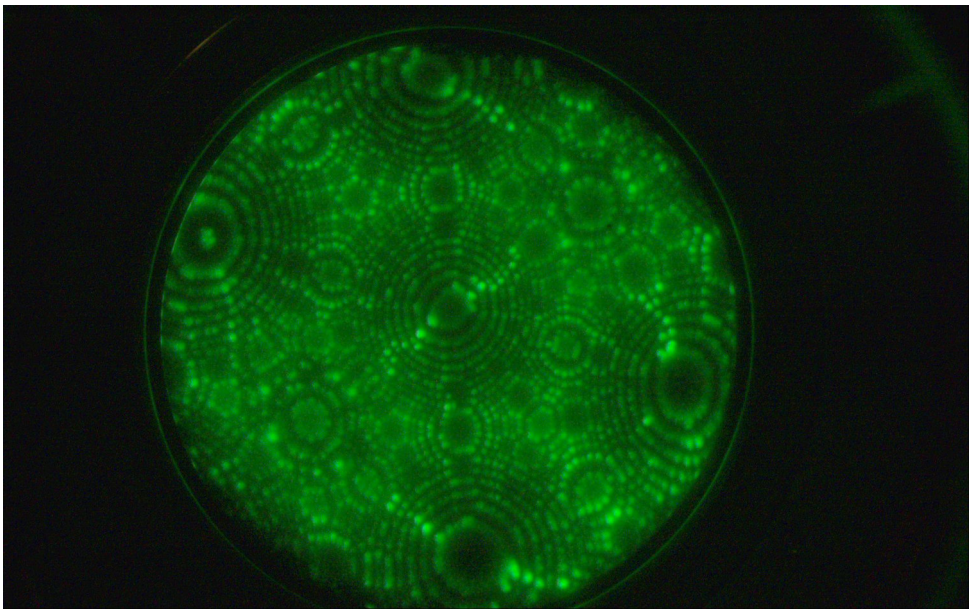

(b)

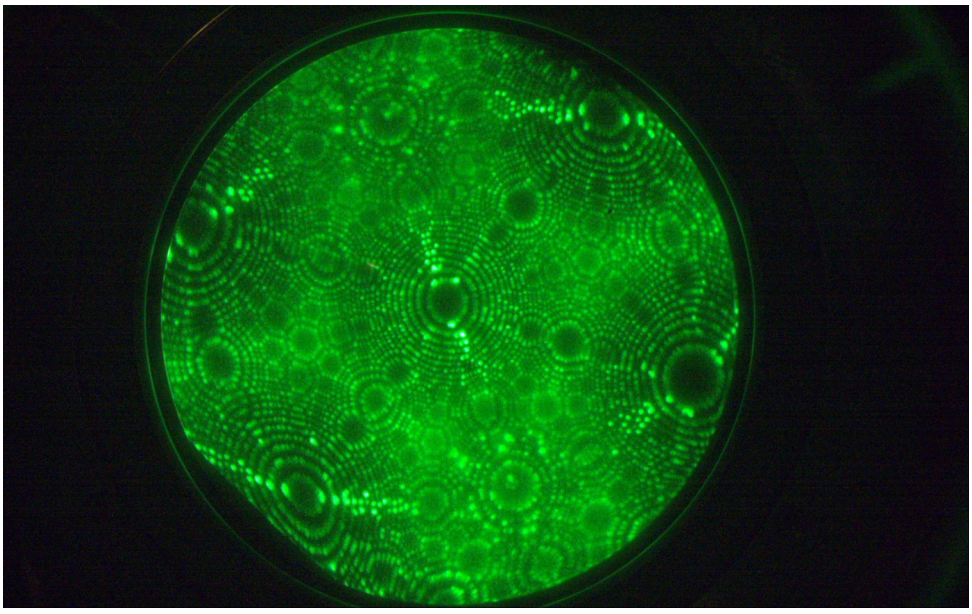

Figure 2.3.: The field ion image of a tungsten tip. In (a), the applied voltage amounts to 8.2 kV, while the voltage in (b) was set to 12 kV. (Courtesy of Helena Solodenko)

Before a metal atom is removed from the emitter surface, it already becomes partially ionic because electrons will drain out due to the presence of the electric field. This model is called the *revised* charge-draining model [17]. In the original charge-draining model [30] it was assumed that the atoms evaporating from the surface are initially bound in a

neutral state and that its charge would only drain out in very close vicinity to the energy barrier, which has to be overcome. Quantum-mechanical considerations made by Sanchez et al. [31] support the idea of the revised version of the charge-draining model, which states that even relatively far away from the energy barrier the atom are already partially ionized. Prior to these two models, Müller first introduced the *image hump* model [22], which is assuming that full ionization takes place before the ion passes the potential energy hump. This model is nowadays believed to be less accurate than the revised charge-draining model.

The exact value for the critical field strength, which leads to the emission of ionized atoms is called the *critical evaporation field* or simply *evaporation field* E_{crit}. Given this particular field strength, the activation energy $Q(E_{crit})$ for field emission vanishes. The value of E_{crit} is material dependent. With the help of the energy balance Q_0 of the FEV process of a single charged ion

$$Q_0 = \Delta + E_I - \Phi_0, \tag{2.3}$$

a final estimation for the evaporation field can be made. In the energy balance equation (2.3), Δ represents the bonding (sublimation) energy, E_I the ionization energy of the atom and Φ_0 the work function of the material. The idea behind equation (2.3) is that when an atom is removed from the surface, the bonding energy and the ionization energy has to be spent. At the same time, an electron is drained, which delivers the work function back to the electron system.

Further considerations made by Müller [32], and Gomer and Swanson [25] finally yield the evaporation field for a single charged ion:

$$E_{crit} \approx \frac{4\,\pi\,\epsilon_0}{e^3}\,Q_0^2. \tag{2.4}$$

The dependency of the activation energy $Q(E)$ from the applied electric field was first expected to be

$$Q(E) = Q_0 - \sqrt{\frac{e^3}{4\,\pi\,\epsilon_0}\,E} \tag{2.5}$$

according to Müller. However, experimental investigations indicated that the relationship is approximately linear [33]. This finding does not necessarily contradict to Müller's expression. In close vicinity to the critical evaporation field ($E \approx E_{crit}$), a Taylor expansion

of (2.5) yields

$$Q(E) \approx \frac{Q_0}{2}\left(1 - \frac{E}{E_{crit}}\right). \tag{2.6}$$

The possibility to trigger and steer the FEV process lead to the idea of detecting the field-evaporated ionized atoms rather than image gas ions, like it is done in FIM. This concept forms the principle of APT.

2.1.3. Volume analysis

Historically, the first atom probe setup comparable to modern instruments was the so-called *imaging atom probe* introduced by Panitz [34]. The important property of this instrument was its wide field-of-view (FOV) and a spherically curved phosphor screen (combined with micro channel plates) acting as a detector. Further improvement by Cerezo et al. [35], Deconihout et al. [36], and Blavette et al. [37] finally allowed to determine the impact position on the detector by using a planar detector which followed several micro channel plates. These improved instruments were able to record the x- and y-coordinates of the impact positions of detected ions. In addition, they enabled the user to record data sets in the range of a few million atoms.

In 2003 the so-called LEAP® (local electrode atom probe) was introduced [38, 39]. This instrument is nowadays widely used in the atom probe community (in different released versions). As the name is already indicating, the LEAP® uses a counter electrode in front of the atom probe tip. This counter electrode has a central circular aperture, which increases the field strength at the tip apex. In contrast to previous devices, these modern instruments are able to collect several millions of ion impacts in a single measurement. The field evaporation can be triggered in two contrasting ways, either by a short voltage pulse or by a laser pulse. Laser-pulsed devices give access to the analysis of poorly conducting materials apart from metals. Therefore, instruments using laser-pulses are becoming more and more popular. Nevertheless, not all groups working on the field of APT are using the commercial LEAP®, but rather designed their own individual devices [40–42].

As mentioned above, APT can be interpreted as a kind of update of a FIM. In principle, the experimental setup is very similar (see figure 2.4), except the fact that no image gas is needed. The very high values for the electric field, achieved by applying a moderate positive voltage of several kV and reducing the sample dimension to a needle with a curvature radius of a few nanometers, are created in very close vicinity to the emitter surface. The

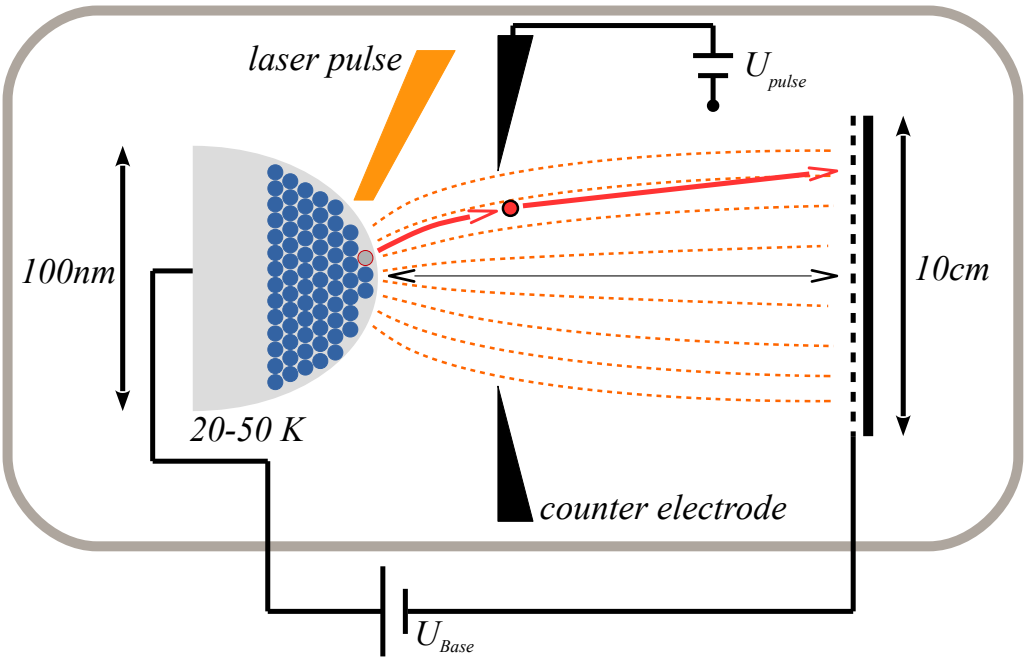

Figure 2.4.: Sketch of the experimental set-up in atom probe tomography. The tip (left) is mounted in front of the position-sensitive detector with a distance of a few cm. The whole set-up is located inside a vacuum chamber with a pressure of approximately 10^{-10} mbar. The base voltage is applied between tip and detector. It is complemented by either a voltage pulse at the counter electrode or a short laser pulse. The removed ions (red) are accelerated towards the detector due to the presence of the electric field (orange dashed lines).

electrical field at the emitter apex is approximately given by

$$E_{apex} = \frac{U}{\beta\, r}, \tag{2.7}$$

with the total voltage U applied to the tip, the curvature radius r and the *field factor* β. The field factor is treated as a constant parameter depending on the instrument and the sample. Typical values for β are between 3 and 12. If the tip could be described by a perfectly smooth sphere without a shank or cone underneath, β would have a value of 1. Due to the deviation of the tip shape from a sphere, the field factor is needed.

The origin of this surprisingly simple formula stems from the consideration of an example geometry, where the shape of the tip is described by a paraboloid (for a detailed derivation see [43]). Although the description of the tip by a paraboloid is not completely realistic, it turns out that the field factor at the apex and along the tip axis just depends logarithmically on the actual emitter shape. Consequently, equation (2.7) is considered to be useful in general. Usually it is used to determine the curvature radius of the tip during a measurement, as the voltage U is known.

Since atomic noise levels should be depressed, the field emitter is cooled down to a

temperature in the cryogenic range (20 − 50 K). The atom probe needle is mounted in front of the position-sensitive detector with a distance of a few centimeters (see figure 2.4). The measurement takes place in a vacuum chamber with ultra high vacuum conditions ($\sim 10^{-10}$ mbar), which are necessary in order to avoid any breakdown of the electrical field and to ensure a comparably "clean" environment, so that no impurities will affect the results of the experiment and the ion trajectories won't be disturbed by collisions. A constant base voltage U_{base} is applied between the field emitter and the detector. The limited field caused by the base voltage is still not sufficient to trigger FEV. Therefore, an additional voltage pulse U_{pulse} is applied, which brings the tip into a state, where significant field desorption occurs. Typically, the voltage pulse is supplied by short negative pulses to an extraction electrode (counter electrode in figure 2.4). The pulse frequency is usually in the range of 100 to 200 kHz.

For laser-assisted atom probe measurements, the base field is complemented by a short laser pulse. In this case, FEV is triggered by thermal activation in form of a short heat pulse. The choice of the laser power is critical to the quality of the measurement and is strongly material dependent [44]. In order to achieve reliable results, the amount of heat introduced to the system must be restricted, since high temperatures might cause migration of atoms on the emitter surface before field desorption. A careful optimization of the laser power and the pulse frequency ensures a sufficient cooling time of the tip surface after each individual pulse. The pulse frequency of the laser is typically in the range of a few hundred kHz with a pulse duration shorter than 20 ps (even as low as 120 fs in some cases). Nevertheless, it is worth to mention that these values might differ severely depending on the investigated material and the type of laser being used.

Following an atom probe experiment, the recorded data needs to be "reconstructed" (see section 2.2). To this end, a suitable model for the tip shape is required. A convenient approximation for the shape of the atom probe needle assumes that a general field emitter is composed of a truncated cone with a spherical cap on top. The cone has a taper angle α and the cap has a curvature radius r_{tip}. This model delivers a rather simple approach for the later reconstruction of the measurement data. The truncated cone/shaft of the tip acts as a focusing lens during the FEV. As it is indicated in figure 2.4, the ion trajectories are deflected towards the detector. This focusing effect needs to be taken into account in a reconstruction approach, as it is described below.

2.2. The point projection reconstruction approach

Once an atom probe experiment has successfully been carried out, the recorded data, containing the time-of-flight and the impact position of the detected ions, need to be post-processed. In general, this post-processing step is called *reconstruction*. As mentioned before in section 2.1, the final goal is to rebuild the emitter volume in the form of a three-dimensional map, where every detected ion has its well-defined position. Therefore, any kind of reconstruction technique has the task to assign a mass-to-charge ratio and a three-dimensional coordinate to all the recorded particles on the detector. The mass-to-charge ratio m/q is derived from the time-of-flight in a straight forward way:

$$\frac{m}{q} = 2\,U\,\frac{t^2}{d^2}, \tag{2.8}$$

with the accelerating voltage U, the distance d between tip surface and detector and the recorded time-of-flight t. For a better mass resolution, a long flight length is desired, but this gain of mass resolution is counteracted by a decrease in the field-of-view (e.g. the lateral width of experimentally accessible sample volume). To this end, solutions like the introduction of a reflectron with focusing properties into the atom probe have been made, which helps increasing the mass resolution without a reduction of the FOV [45].

The more complicated part of the reconstruction of a measured particle is the *spatial reconstruction*, e.g. the determination of the Cartesian coordinates inside the field emitter volume. In order to find the three-dimensional coordinates within the emitter volume, Bas et al. proposed a surprisingly simple and purely geometric method based on two main assumptions [46]. First, ion trajectories from the emitter surface to the detector are considered as straight linear projection lines between the hit position and a projection point P, located along the tip axis inside the emitter volume (see figure 2.5). For this reason, this technique is commonly known as the point projection approach.

As a second assumption, the shape of the emitter apex is assumed to be spherical with a constant radius of curvature r located on a truncated cone with a constant shank angle α throughout the whole reconstruction procedure. This simplification of a stable *endform* of the tip after a sufficiently long FEV process was confirmed by simulation approaches [47], even though it has to be mentioned that the initial spherical shape changed slightly towards a more polygonal equilibrium tip surface in the mentioned study. For pure silicon tips, the endform has experimentally been observed to be non-spherical. Furthermore, there also seems to be no tangential continuity between the cap and the shaft of the atom probe needle [48, 49].

The working principle of the method is the following: The reconstruction starts with a

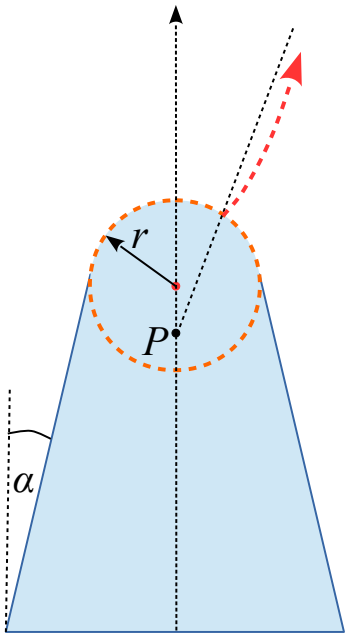

Figure 2.5.: The point projection approach by Bas et al. assumes a constant spherical tip apex with radius r set on a truncated cone with a shank angle α. The real ion trajectories (red dashed arrow) are simply described by a linear back projection (dashed black line) between the impact position on the detector and the projection point P on the tip axis.

semi spherical tip surface, defined by a user specified radius of curvature r. The initial apex position z_{apex} along the tip axis is also user specified. Each ion is reconstructed one after the other until all recorded atoms have been processed. The process starts with the first detected atom, which means, the reconstruction is performed from top to bottom. The three-dimensional coordinates of one particular atom are given by the point of intersection between the projection line, leading from the detector impact position to the projection center on the tip axis, and the emitter surface (see figure 2.6):

$$\begin{pmatrix} x \\ y \\ z \end{pmatrix} = \begin{pmatrix} 0 \\ 0 \\ z_{apex} \end{pmatrix} + \begin{pmatrix} r \sin(\vartheta'/\xi)\cos(\varphi) \\ r \sin(\vartheta'/\xi)\sin(\varphi) \\ 1 - \sin(\vartheta'/\xi) \end{pmatrix}. \tag{2.9}$$

Here φ is the azimuth angle of the hit position (x', y') on the detector plane and ϑ' denotes the detection angle of the ion on the detector with the distance l to the tip (see figure 2.7b)):

$$\vartheta' = \arctan\left(\frac{\sqrt{x'^2 + y'^2}}{l}\right). \tag{2.10}$$

The image compression factor ξ takes into account the focusing effect of the electric field

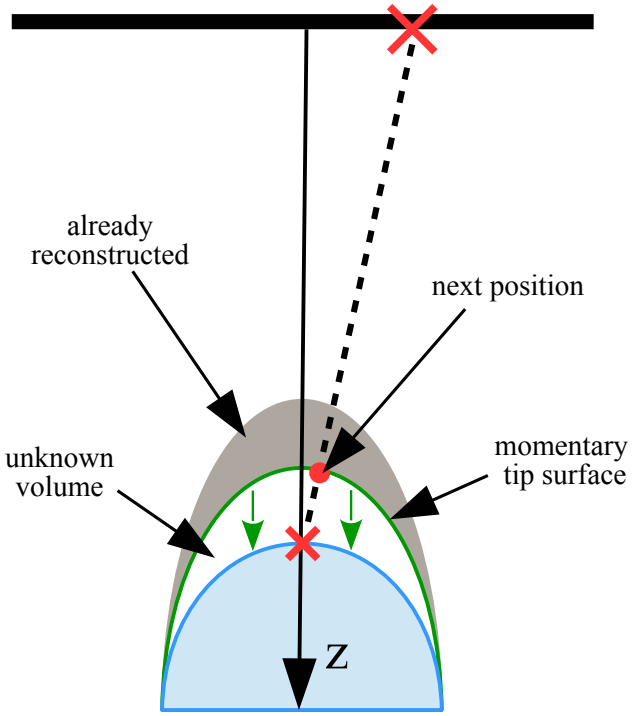

Figure 2.6.: Principle of the geometric reconstruction method [46]. For each detected ion the reconstructed coordinates are given by the point of intersection (red dot) between the linear back projection of the detector coordinate and the current tip surface (green). The volume is built up from top to bottom (grey), while the emitter surface is shifted downwards. The blue volume represents the remaining tip after the experiment.

on the ion trajectories. For small detection angles ($\vartheta' < 30°$), the linear relation $\vartheta = \vartheta'/\xi$ between the detection angle and the respective emission angle is a suitable approximation. For a larger FOV, a different approximation should be chosen, which will be discussed later in section 4.1.1. Since no azimuthal distortion is assumed in this model, the angle φ on the detector is the same for the reconstructed coordinate of the detected ion. As a consequence of equation (2.9), the z-coordinate of reconstructed events is larger for atoms that are being reconstructed closer to the center of the detector.

After each step, the current position of the emitter apex has to be shifted downwards in order to take into account the shrinkage of the tip during FEV. This increment Δz is depending on several parameters:

$$\Delta z = \frac{\Omega}{\rho_{Det}} \frac{M^2}{A_{Det}}. \tag{2.11}$$

Δz is proportional to the atomic volume Ω and the squared magnification factor

$$M = \frac{l\,\xi}{r}. \tag{2.12}$$

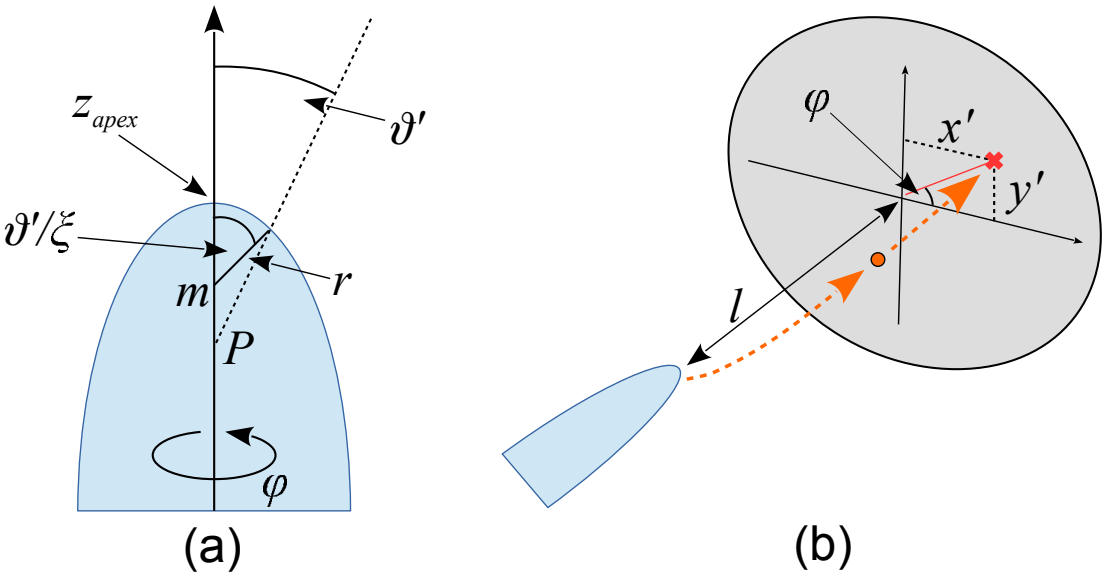

Figure 2.7.: Illustration of the point projection approach. In (a), the ion trajectory is approximated by a linear back projection from the detector to the projection point P (dashed line). Due to the focusing effect of the tip shank, the detection angle ϑ' differs from the emission angle $\vartheta = \vartheta'/\xi$. Note that P typically lies behind the center m of the spherical cap with radius r (for $m = P$ it would be a radial projection). In (b), the measurement of the impact position (x', y') on the detector and the corresponding azimuthal angle φ for the later evaluation of equations (2.9) and (2.10) are shown.

Furthermore, the increment also depends on the detector area A_{Det} and the detector efficiency ρ_{Det}, which is introduced in order to consider the volume of missing atoms that could not be detected.

The derivation of (2.11) starts with an estimation of the number of evaporated atoms N with constant volume Ω during the FEV of a thin layer on the tip apex. This layer has a thickness Δd and is limited by the emitter aperture ϑ_{max}:

$$N = \frac{A(\vartheta_{max})\,\Delta d}{\Omega}. \tag{2.13}$$

The captured surface area $A(\vartheta)$ of the layer can be expressed by the overall detector area and the magnification factor within a small angle approximation:

$$N \approx \frac{A_{Det}\,\rho_{Det}\,\Delta d}{\Omega\,M^2}. \tag{2.14}$$

The emitter shrinkage Δz can now be approximated by

$$\Delta z \approx \left(\frac{dN}{d\,(\Delta d)}\right)^{-1} \tag{2.15}$$

which yields equation (2.11).

For samples with a non-zero shank angle α the curvature radius r is increasing during shrinkage (see for example chapter 7 in [18]). This results in a blunting of the emitter, which has to be included into the previous considerations. If the emitter is shrinking by Δz, the change of curvature is given by

$$\Delta r = \frac{\sin(\alpha)}{1 - \sin(\alpha)} \Delta z. \tag{2.16}$$

After the calculation of the z-increment $(\Delta z)_i$ in reconstruction step i, the change of curvature $(\Delta r)_i$ is determined. The new curvature radius is taken into account in equation (2.11) by inserting it into equation (2.12) for the next z-increment $(\Delta z)_{i+1}$:

$$(\Delta z)_{i+1} = \frac{\Omega}{\rho_{Det}\, A_{Det}} \frac{l^2 \xi^2}{(r_i + \Delta r)^2}. \tag{2.17}$$

Regarding the general model of the tip in the case of a non-zero shank angle, typically tangential continuity between spherical cap and cone is assumed. In the reconstruction, this continuity is included by (2.16), even though modifications of this equation, neglecting tangential continuity have been proposed [50].

2.2.1. Extension of the point projection approach for large detection angles

The point projection approach presented in section 2.2 yields sufficient results for the three-dimensional atom positions in the case of atom probe experiments with a very limited field-of-view ($\vartheta' \leq 5°$). For larger detection angles ϑ', which means for locations further away from the tip axis, the resolution of the reconstructed tip volume decreases. This decrease is mainly caused by the assumption of a constant emitter curvature, even though tip blunting is already considered.

Furthermore, the z-increment in equation (2.17) has been derived within a small angle approximation (see equation (2.14)) regarding the emission angle ϑ. For larger angles, the analyzed volume can no longer sufficiently be described by a planar layer with a thickness Δd and an area A_{Det}/M^2. Since the FOV in modern instruments is comparably large ($\vartheta' \leq 40°$), an improvement of the point projection approach, especially for the expression of the emitter shrinkage Δz, was required. Such improvements have been presented by Geiser et al. [51], Gault et al [52], and earlier by Walck [53]. These extensions of the Bas approach take into account the dependency of the emitter shrinkage Δz from the enhanced FOV. Furthermore, the influence of the shank angle and the tip blunting are included. The

emitter shrinkage is generally given by

$$\Delta z = \frac{\Omega}{\rho_{Det}\,(dv/dz)}. \tag{2.18}$$

Here the function dv/dz describes the change of the analyzed emitter volume v during reconstruction. In order to derive the change of the volume, v is described by a tip composed of a spherical cap sitting on a cone with a shank angle α. On the bottom, the truncated cone is cut by a second spherical cap with a different curvature radius (see figure 2.8a)). The overall volume v is then given by two cap volumes V_{k1} and V_{k2} and the difference between two cone volumes V_1 and V_2 (light blue volume in figure 2.8a)). Consequently, the total volume reads

$$v = V_{k1} - V_{k2} + V_2 - V_1. \tag{2.19}$$

Another useful expression for v is given by

$$v = v(z + \Delta z) - v(z) = \Delta z\,\frac{dv}{dz}. \tag{2.20}$$

In the following, an expression for the volume v is derived. Straight-forward geometric considerations yield the following expression for a cone volume as it is described in figure 2.8b):

$$V_{cone}(z) = \frac{\pi}{3}\,R^2\sin^2(\vartheta)\cdot(z + \Delta z'). \tag{2.21}$$

Here, R denotes the initial tip radius. Since the tip blunts according to figure 2.8c)

$$R = z\,\frac{\sin(\alpha)}{1-\sin(\alpha)} =: z\cdot w, \tag{2.22}$$

the volume of cone 1 in figure 2.8a) equates to

$$V_1 = \frac{\pi}{3}\,R^2\sin^2(\vartheta)\;[1 + w\,(1-\cos(\vartheta))]\;z. \tag{2.23}$$

Since the second cone is shifted downwards by Δz, its volume is given by

$$V_2 = \frac{\pi}{3}\,R^2\sin^2(\vartheta)\;[1 + w\,(1-\cos(\vartheta))]\;(z + \Delta z). \tag{2.24}$$

For the spherical cap on the top, the volume can be expressed by

$$\begin{aligned} V_{k1} &= \frac{\pi}{3}\,\Delta z'^2\,(3\,R - \Delta z') \\ &= \frac{\pi}{3}\,R^2\,z\,w\,(2 - 3\cos(\vartheta) + \cos^3(\vartheta)), \end{aligned} \tag{2.25}$$

and for the second cap accordingly

$$V_{k2} = \frac{\pi}{3}\,R^2\,(z + \Delta z)\,w\,(2 - 3\cos(\vartheta) + \cos^3(\vartheta)). \tag{2.26}$$

Finally, the combination of equations (2.19) and (2.20) together with (2.23)-(2.26) yields

$$\frac{dv}{dz} = \pi\,R^2\,\left[\sin^2(\vartheta)\,(1 + w\,(1 - \cos(\vartheta))) - w\,(2 - 3\cos(\vartheta) + \cos^3(\vartheta))\right]. \tag{2.27}$$

With the relation in equation (2.27), the z-increment (2.18) becomes more suitable for the reconstruction of volumes measured with an atom probe with a large FOV. Again, in contrast to this linear dependency of the analyzed volume from the z-increment, the Bas et al. approach assumes that the volume is distributed homogeneously across the analyzed area A. Within a small angle approximation, S can be expressed by the detector area A_{Det} and the magnification M, so that $dv/dz = A_{Det}/M^2$.

In conclusion, the main difference between the Bas et al. approach and the extension by Geiser et al. is the missing necessity of a small angle approximation and the more accurate description of the analyzed volume from the z-increment (the analyzed area respectively). Nevertheless, the extension is still a geometric approach that assumes a hemispherical cap.

2.2.2. Limitations of the geometrical approach

The reconstruction approach presented in section 2.2 has proven to deliver reasonable results for emitter structures containing materials with similar threshold fields of evaporation. The absence of strong deviations in the evaporation field ensures a tip shape during FEV, which can sufficiently be described as spherical. In many cases it was even possible to reconstruct atomic lattice planes in direction of the tip axis.

A challenge for the geometric back projection technique is given by emitter structures with a high degree of inhomogeneity in their evaporation behavior. A difference in the evaporation fields is very likely to lead to artifacts in the geometric reconstruction. The main reason for this is the influence of different evaporation thresholds/probabilities on the emitter shape during an atom probe experiment. In these cases, the tip apex does not have a spherical shape. Instead, the radius of curvature changes locally in dependence

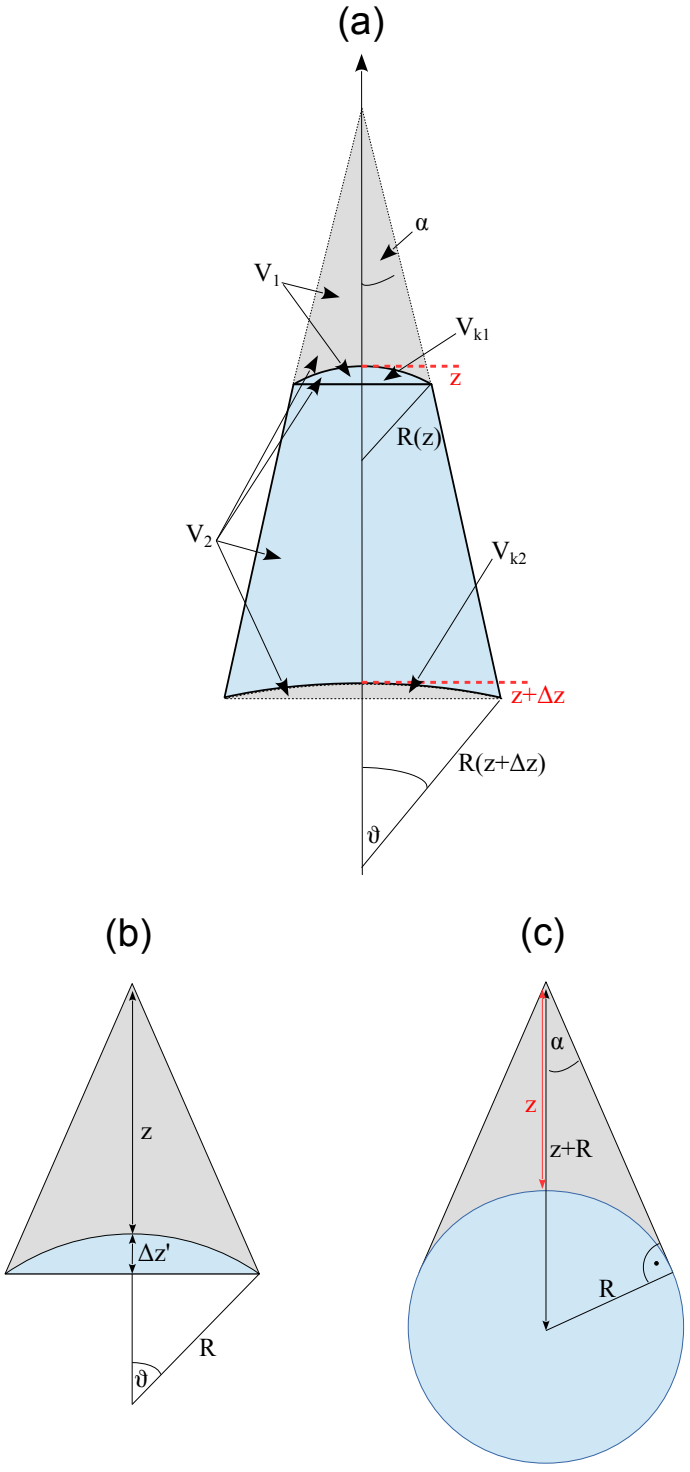

Figure 2.8.: Geometric considerations. The total analyzed emitter volume v (light blue) is shown in (a). The volume is given by a spherical cap on the top (V_{k1}), combined with the difference of two cone volumes ($V_2 - V_1$), which is again cut at the bottom by another spherical cap (V_{k2}). In (b), the geometric relation for equation (2.21) can be observed. The plot in (c) illustrates the dependency of the curvature radius R from the shaft angle α in (2.22).

on the current local composition on the tip surface, which leads to local magnification effects and even trajectory overlaps [11, 54, 55]. An example for the influence of such local magnification effects is presented in figure 2.9b), where the reconstruction of a tip containing a spherical particle with a higher evaporation field (see figure 2.9a)) is shown. This example is a simulated field evaporation. Due to the higher evaporation threshold, the precipitate forms a protrusion during FEV, as soon as it appears at the emitter surface 2.9c).

In order to point out this effect on the surface shape, figure 2.10 illustrates the change regarding the curvature radius of the emitter surface shown in figure 2.9c) along the radial direction perpendicular to the tip axis. The structure of the given example volume is amorphous, since the formation of crystallographic facets is avoided in this way, which is beneficial for the calculation of the curvature radius. For comparison, in figure 2.10 the curvature radius is also shown for the initial tip surface, where the radius in the center has a value of approximately 29 nm. Despite some numerical fluctuations, it can be seen that the curvature radius drops significantly in the center in the later stage, where the precipitate protrudes at the surface. Here, the curvature radius amounts to approximately 19.5 nm. The ratio of these curvature radii is equal to 19.5 nm/29 nm=0.67.

The simulation of the field evaporation has been carried out by taking into account the force acting on a surface atom. In every simulation step, one particular atom is evaporated. In this case, always the atom experiencing the highest force has been emitted. The force is proportional to the squared evaporation field. This means that the difference of the involved evaporation field has also been squared. The ratio of the squared evaporation fields in the simulation amounts to $(1.0/1.25)^2 = 0.64$. This value is astonishingly close to the ratio of the curvature radii in the center. The relationship between the radius of curvature and the evaporation fields of different phases will be further discussed in section 4.1.3.

The varying shape of the tip leads to a strong outward deflection of the ions around the protrusion. This deflections can not be correctly taken into account in the later reconstruction as long as the emitter shape is assumed constant, which leads to a distorted reconstruction of the precipitate (see figure 2.9b)) accompanied with a significant fluctuation regarding the atomic density, which will be discussed in chapter 4. Further examples for the difficulties in connection with the reconstruction performed with the point projection approach can be found in [56] or [57].

In order to overcome these drawbacks, an improved reconstruction technique is needed. In the past, several approaches have been suggested. For example, the calibration and estimation of the constant reconstruction parameters included in the point projection approach (e.g. the image compression factor and the field factor) has been improved [58–61]. In another rather complex attempt, TEM images of the emitter surface were

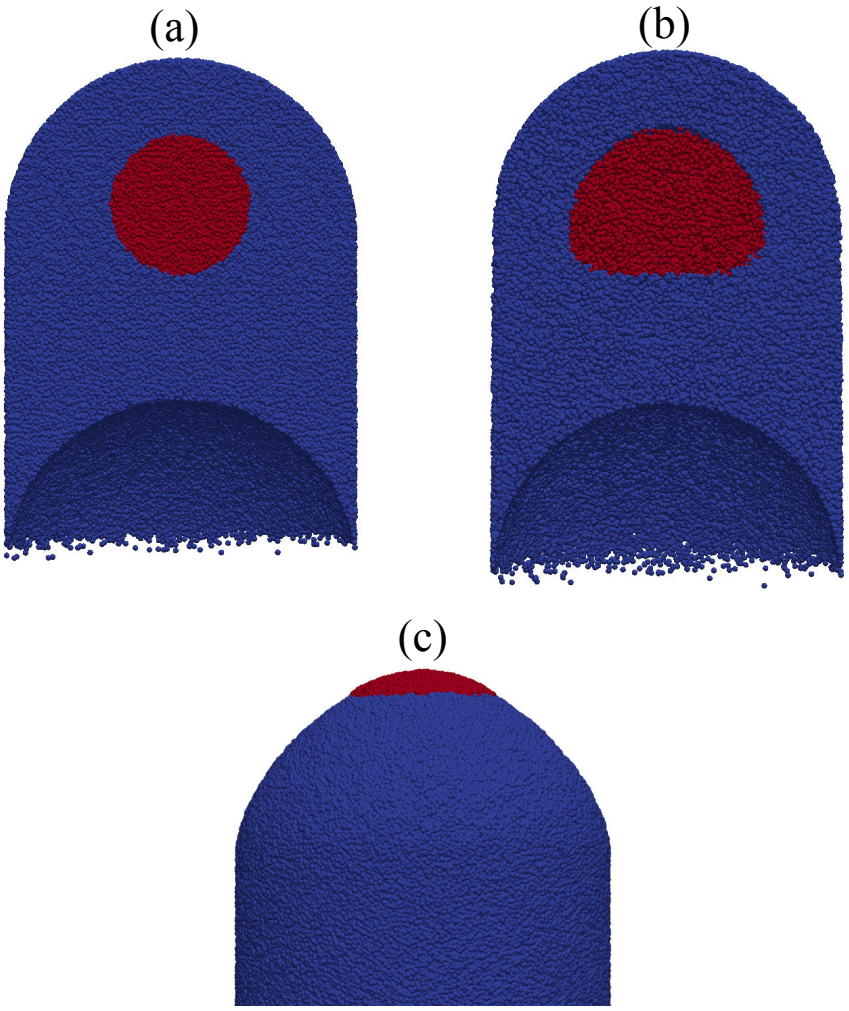

Figure 2.9.: Well-known artifacts of the geometric reconstruction approach demonstrated by the example of an amorphous tip structure containing a spherical precipitate (a). The atoms belonging to the precipitate (red) have a 25% higher evaporation field compared to the surrounding matrix (blue). Due to local magnification effects, the precipitate in (b) appears deformed and broader in lateral direction in the reconstruction. The tip shape during the simulated FEV is shown in (c).

used in order to obtain the surface shape during FEV and use this additional information in the reconstruction [62]. In addition, a correlative electron tomography approach has been performed for the case of porous materials [63]. Furthermore, for the improvement of the reconstruction on a larger scale (above 10 nm), an iterative technique based on computational geometry has been presented [64].

Despite these contributions aiming for the improvement of the spatial reconstruction, the need for an easy to use, fast and reliable approach is still urgent. If a new approach did not rely on the simple geometric assumptions of the established technique, a higher quality of the results, especially in the case of inhomogeneous tip structures, could be expected. Therefore, an amended algorithm should allow the tip structure to deviate from a spherical

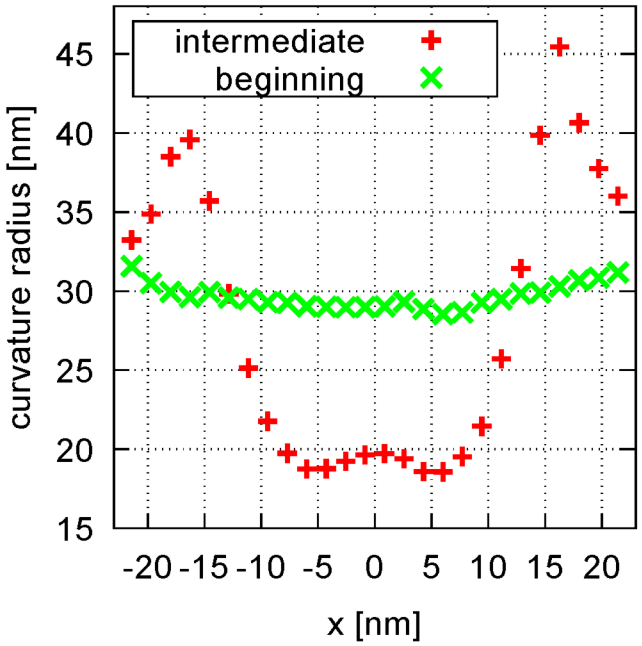

Figure 2.10.: The radius of curvature at the tip surface along the projected radial direction containing a precipitate with a higher evaporation field (figure 2.9a)). The curvature radius is shown for the emitter surface at the beginning (green) and at an intermediate state of the FEV (red) according to figure 2.9c).

shape locally at any time during the reconstruction. In addition, the simple description of the ion trajectories as projection lines should better be replaced by realistic flight paths. To this end, based on the electrical field defined by the current emitter shape, ion trajectories need to be calculated during the reconstruction.

As a first step towards this goal, the proof of principle for such an approach is demonstrated in section 3.1, where the simulated FEV of an atom probe tip is basically reversed. Later in section 3.2, this approach is being further extended, in order to make the approach more applicable to a realistic situation. Since the basic concept of the numerical simulation of an atom probe experiment including full trajectory calculation is not trivial, the following section will briefly provide an overview on the most flexible simulation technique.

2.3. Delaunay triangulation and Voronoi tessellation

In this work, the newly developed reconstruction algorithms are tested on simulated data sets. These simulations are routinely performed with the help of the state-of-the-art simulation package *TAPSim*[1]. A simulation is carried out on a lattice of randomly distributed nodes

[1] https://www.imw.uni-stuttgart.de/mp/forschung/atom_probe_RD_center/software/

covering the three-dimensional simulation space. The tip structure is located at the bottom of the simulation space. This tip is further surrounded by a large number of support nodes. The support nodes cover the vacuum inside the simulation space (measurement chamber) and are essential to solve Poisson's equation. The solution of Poisson's equation delivers the electrical potential at each node in the grid, which further allows the calculation of the electric field acting on the tip surface and on field-evaporated ions. Once the equilibrium potential is known, the given emitter structure is field-evaporated atom by atom and a realistic trajectory for each ion is calculated on the full length between the tip surface and the detector. This procedure is repeated until either the whole tip has been evaporated, or a user-specified number of events is recorded.

For the simulation of realistic ion trajectories from the emitter apex to the detector, it is useful to split the simulation space into different domains. In the case of the simulation package *TAPSim*, this is done by covering the simulation space with a mesh of support points as mentioned above. These points are further connected by a three-dimensional tessellation composed of tetrahedra, the so-called *Delaunay tessellation*. The nature of such tessellation of the simulation space is now discussed in two-dimensional space for the sake of simplicity.

In two dimensions, the tessellation is called Delaunay triangulation because the tetrahedra in three dimensions are replaced by triangles in 2D. The triangulation is performed by connecting a grid of arbitrarily distributed points with so-called *Delaunay triangles* (see the triangles in figures 2.11b) and 2.11c)). The defining characteristic of a Delaunay triangle is its empty circumcircle. This means that for a given triangle in the triangulation no point of the point distribution (e.g. no vertex of any other triangle) is located inside its circumcircle (see figure 2.11c)). For the three-dimensional case, the empty circle criterion translates to an empty circumsphere defined by the four vertices of each tetrahedron belonging to the tetrahedral mesh. In addition to the empty circle/sphere property, the boundary of a Delaunay tessellation/triangulation is always convex.

In order to set up the triangulation of a given arbitrary point distribution, several algorithms exist. In this work, the Boyer-Watson algorithm has been applied [65]. Following this scheme, the tessellation is built up by inserting the individual points one by one into the already existing triangulation (defined by the previously inserted points) in each step until all points have been inserted. Starting with an initial triangle given by the first three points in the point list (as long as those points are not aligned), every point is inserted one after the other leading to a constantly changing appearance of the current triangulation. The procedure is shown in figures 2.12a)-2.12d) for the two-dimensional example of figures 2.11a)-2.11c). In figure 2.12a), a new point is inserted into the existing Delaunay triangulation. Due to the fact that the point is located inside the triangulation, it

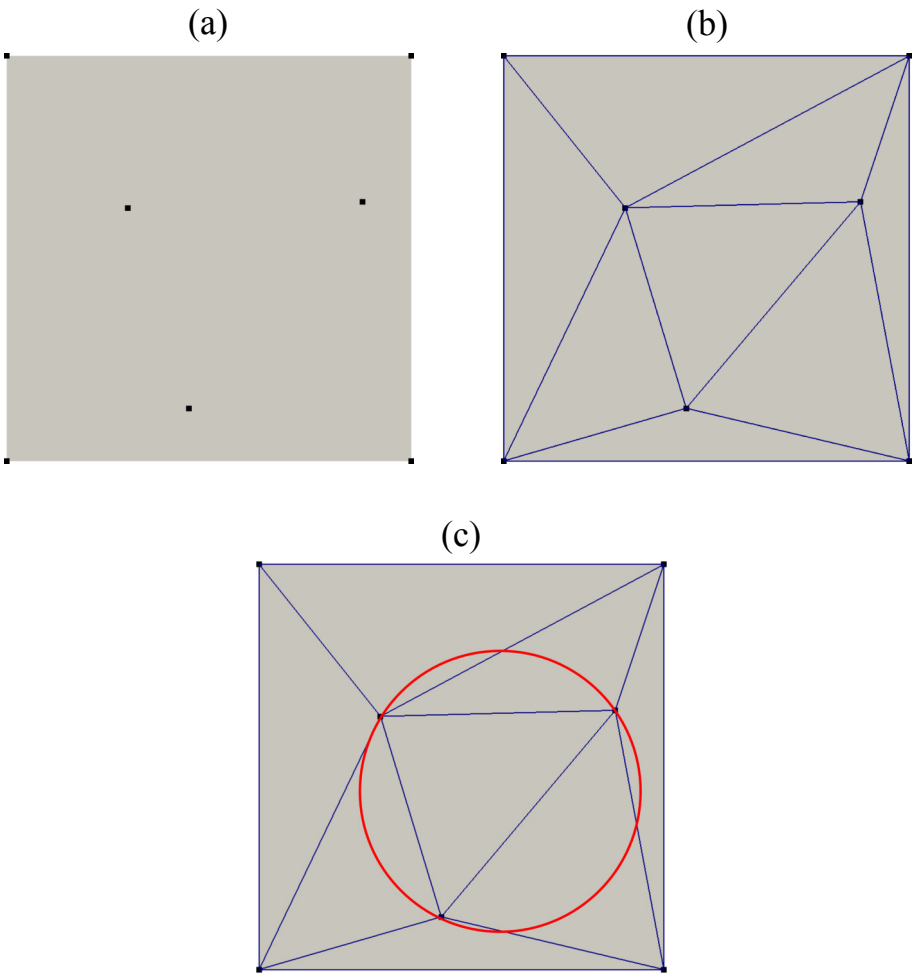

Figure 2.11.: Example for a two-dimensional Delaunay triangulation. The point distribution in (a) is connected by a mesh of Delaunay triangles (b). The red circle in (c) indicates the characteristic property of each triangle, namely the empty circumcircle.

can be expected that at least one triangle becomes invalid. In figure 2.12b) it can be seen that two triangles need to be deleted because their respective circumcircles are no longer empty. Once all invalid triangles have been deleted, the new point is located inside a cavity formed by the remaining edges of the invalid triangles. In order to fill this cavity, all points belonging to the surface of the cavity are connected to the new point of the triangulation. In the end, the cavity is filled by new Delaunay triangles and the complete triangular mesh is a Delaunay triangulation again (figure 2.12d)). This scheme can directly be applied to the three-dimensional case. In three dimensions, the cavity shown in figure 2.12c) is composed of the left over triangular facets of the deleted invalid tetrahedra.

The Bowyer-Watson algorithm can also be reversed in cases, where the deletion of a vertex of the point distribution is required. All triangles (tetrahedra) connected to the deleted vertex also have to be removed from the triangulation. Again a cavity is left in the

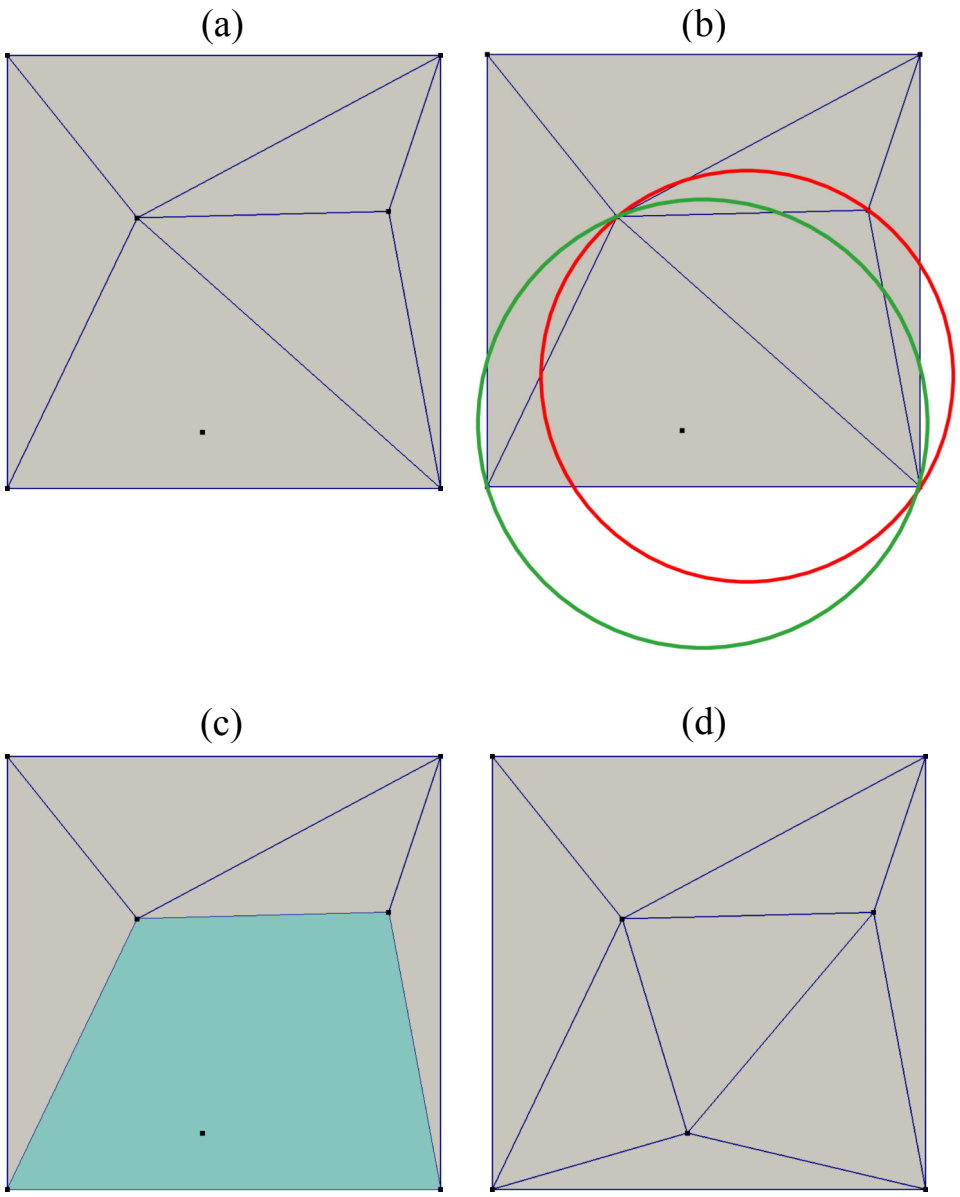

Figure 2.12.: Insertion of a point to an already existing Delaunay triangulation. In (a) the new point is inserted to the list of vertices belonging to the triangulation. This makes the two triangles denoted by their respective circumcircles become invalid (b). The invalid triangles are deleted from the triangulation leaving a cavity surrounding the new point (c). Consequently, all points of this cavity are connected to the new point, which leads to the formation of new Delaunay triangles filling the cavity (d).

mesh, which has to be refilled with Delaunay triangles (tetrahedra). This task can easily be addressed by treating all points belonging to the cavity as a separated grid. This grid has to be triangulated according to the above introduced algorithm and can subsequently be inserted into the cavity of the initial triangulation.

It can be shown that for a given distribution of points only one particular Delaunay

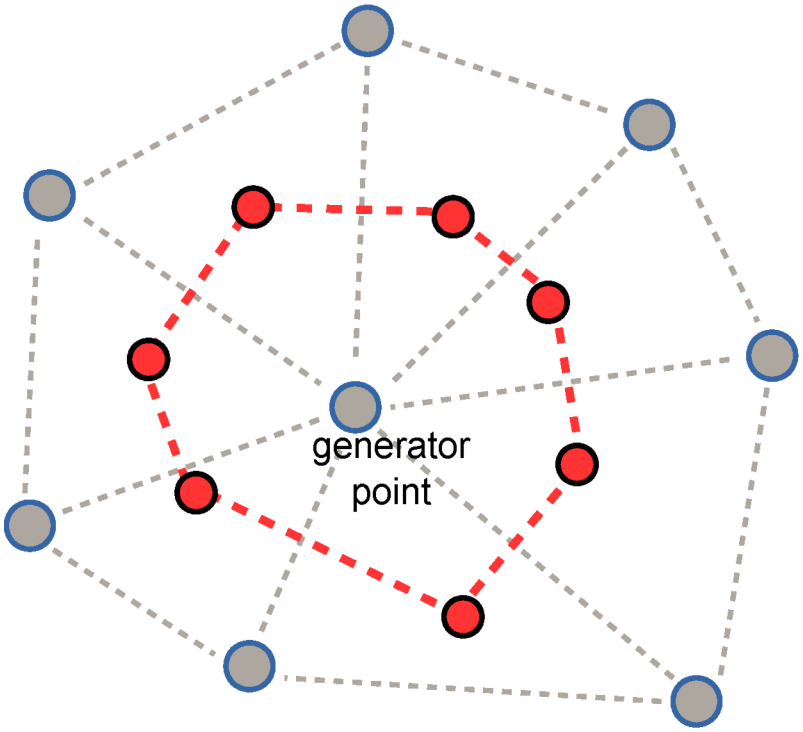

Figure 2.13.: Illustration of the link between a Delaunay and a Voronoi tessellation in the two-dimensional case. The convex Voronoi cell (dashed red lines) confines its generator point, which can also be identified as a vertex of a Delaunay mesh (dashed grey lines). The edges of the Voronoi cell are given by the perpendicular bisectors of the edges of the associated Delaunay triangles.

triangulation exists, except for the special case, where at least one point is lying on the circumcircle of another triangle (for example a rectangular grid in two dimensions).

2.3.1. Voronoi tessellation

Another very useful tessellation of the two-dimensional or three-dimensional space is the so-called *Voronoi* tessellation. The Voronoi tessellation is composed of convex shaped domains, called Voronoi cells. In solid-state physics the concept of a Voronoi cell is well-known as the so-called *Wigner-Seitz cell*. These cells can easily be constructed, if a Delaunay mesh covering the space is already given because the Voronoi mesh can be seen as the geometric dual graph of the Delaunay tessellation.

Each Voronoi cell confines a vertex of the Delaunay mesh and is defined by the intersection of the perpendicular bisectors of the edges (facets) associated to the respective vertex (see figure 2.13). Due to this fact, a Voronoi cell $V(\vec{p}_i)$ is a domain containing all points $\vec{x}$ of the space S, for which the confined Delaunay vertex (the generator point) $\vec{p}_i$ is

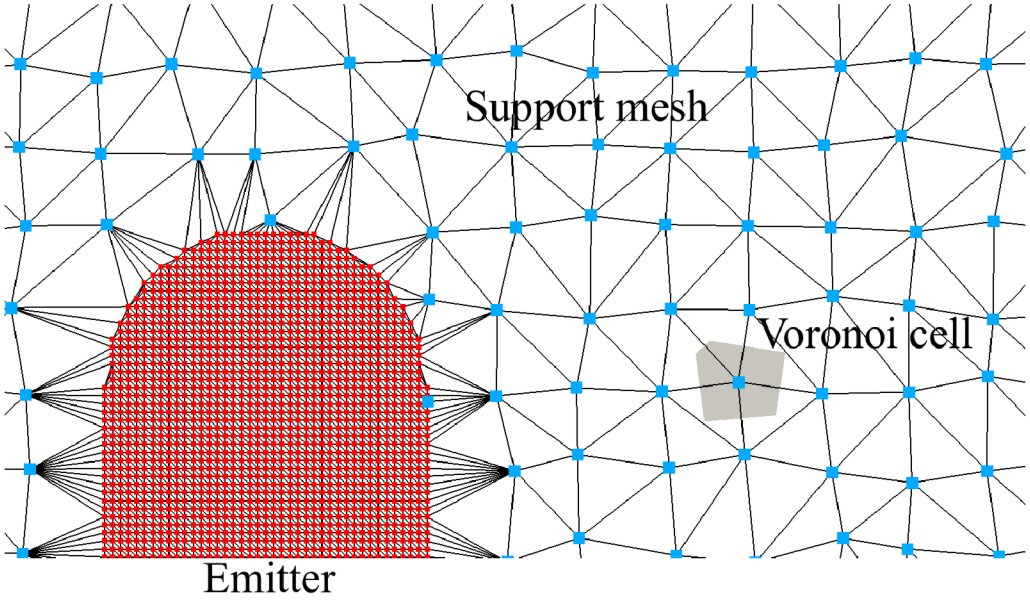

Figure 2.14.: Voronoi tessellation of the simulation space close to the emitter in 2D. The emitter (red) and the support mesh (blue) are connected by a Delaunay triangulation (black lines). Each node acts as a generator point for a Voronoi cell (gray). Poisson's equation for the electrical potential is solved on the irregular grid given by the generator points of the Voronoi tessellation.

closer than any other generator point in the mesh:

$$V(\vec{p}_i) = \left\{ \vec{x} \in \mathbb{R}^n : |\vec{x} - \vec{p}_i| \leq |\vec{x} - \vec{p}_j|, \forall j \neq i \right\}. \tag{2.28}$$

In general, the shape of a Voronoi cell is arbitrary, but for well-known lattice structures like a simple cubic (sc) or body-centered-cubic (bcc) mesh, the corresponding Voronoi cells have a very typical shape. In contrast to any Delaunay tetrahedron or triangle, a Voronoi cell is not necessarily limited. Moreover, the surface area or volume might be infinitely large, if the generator point is located at the boundary of the Delaunay mesh.

The simulation of an atom probe experiment, which has been done in the frame of this work, is based on the Voronoi tessellation of the entire simulation space, as it is illustrated in figure 2.14. The tessellation allows to perform the simulation on a realistic length scale of several centimeters between emitter and detector. The Voronoi partition also provides a very elegant way to solve Poisson's equation for the electrical potential iteratively at the position of each generator point.

Once this equilibrium state of the electrical potential is found for the given current emitter structure, the force at each lattice site on the emitter surface as well as the force acting on an ion located at an arbitrary position inside the simulation space can be determined.

Starting with an initial value for the electrical potential at each node (each generator

point), equation (2.29) is applied in order to approach the final state [66] that fulfills Poisson's equation:

$$P_i = \left(\sum_{j=1}^{N} \gamma_{i,j} \cdot P_{i,j} + \frac{q_i}{\epsilon_0} \right) \cdot \left(\sum_{j=1}^{N} \gamma_{i,j} \right)^{-1}, \tag{2.29}$$

with the potential value $P_{i,j}$ at neighbor j, q_i the charge confined inside the Voronoi cell of point i and $\gamma_{i,j}$ the coupling factor between the points i and j. The index j runs over all adjacent neighbor cells. The coupling factor is depending on the dielectricity values assigned to the Voronoi cells of points i and j, as well as on the distance $d_{i,j}$ between both points and the surface area $A_{i,j}$ of the Voronoi face between the two cells:

$$\gamma_{i,j} = \left(\frac{1}{\epsilon_{r,i}} + \frac{1}{\epsilon_{r,j}} \right) \cdot \frac{A_{i,j}}{d_{i,j}}. \tag{2.30}$$

For every point P_i, a new potential value is calculated. These new values are assigned to the points and the application of equation (2.29) is repeated for every point. With every iteration of equation (2.29), the electrical potential converges towards the solution of Poisson's equation. Once the solution is obtained to a sufficient accuracy, the potential can also easily be determined everywhere in the mesh by interpolation. To this end, the algorithm first identifies the Delaunay tetrahedron, in which the probed position is located in. With the help of this information, the potential value is given by the weighted sum of the respective values at the vertices of the Delaunay tetrahedron, which can be conveniently obtained by expressing the probed position by barycentric coordinates:

$$P(\vec{r}) = \sum_{i=0}^{4} \omega_i \, P_i. \tag{2.31}$$

The described potential is a weighted average, for which the potential values P_i at the vertices are weighted with the barycentric coordinates ω_i of the probed position $\vec{r}$ in the tetrahedron.

In order to integrate Newton's equation of motion for charged particles inside the simulation space, the force acting on these ions needs to be known. In general, the Coulomb force acting on a charged particle (charge q) at position $\vec{r}$ is given by the product of its charge and the electrical field. The electrical field at position $\vec{r}$ is equal to the negative gradient of the potential:

$$\vec{E}(\vec{r}) = -\mathrm{grad}\, P(\vec{r}). \tag{2.32}$$

In the case of a regular mesh, the potential gradient at each point could easily be calculated by applying a finite difference method (e.g. central differences). However, in the general case of an irregular mesh, this simple scheme cannot be used. Therefore, the local "potential landscape" has to be approximated by a differentiable function in the vicinity of each node in the mesh. In *TAPSim*, this is done by fitting a parabolic three-dimensional function to the potential values of every respective generator point and its Delaunay neighbors. The Coulomb force, which is present at the given generator point, simply equates to the derivative of the previously fitted function. In order to obtain the Coulomb force at an intermediate position between the nodes, the weighted sum of the field values at the surrounding Delaunay vertices is calculated in the same way, like it is done for the potential values.

Apart from the partition of the simulation space, another approach to describe the electrical field between the tip and the detector has been introduced recently. This approach works without any partition of the simulation space, which turned out to be useful for some purposes of this work. The approach is explained in section 2.4, below.

2.4. Calculation of the charge distribution on the tip surface

In this work, the reconstruction partly relies on the calculation of realistic trajectories. The trajectory calculation in the reconstruction procedure is based on a scheme, which was first proposed by Rolland and coworkers [67]. In contrast to the well-established simulation approach of Oberdorfer [8], this technique does not rely on a Voronoi tessellation of the simulation space. The absence of such a tessellation is very beneficial because in this way, there is also no grid of support points, which would have to be changed continuously during the reconstruction.

The meshless approach is based on the solution of Robin's equation [68] which describes the charge density on the surface of a conductor:

$$\sigma(\vec{P}) = \frac{1}{2\pi} \int \int_S \frac{\vec{n}_P \cdot \vec{u}}{|\vec{u}|^3} \sigma(\vec{P}')\, dS'. \tag{2.33}$$

Here σ is the charge density, $\vec{P}$ and $\vec{P}'$ are positions on the conductor surface, $\vec{n}_P$ is the normal vector at position $\vec{P}$, $\vec{u}$ is connecting $\vec{P}$ and $\vec{P}'$ and dS' is the surface element at $\vec{P}'$.

The solution of equation (2.33) can be found by applying an iterative method considering

a sequence of charge density distributions $\sigma_n(\vec{P})$ starting with an arbitrary σ_0:

$$\sigma_{n+1}(\vec{P}) = \frac{1}{2\pi} \int \int_S \frac{\vec{n}_P \cdot \vec{u}}{|\vec{u}|^3} \sigma_n(\vec{P})\, dS'. \tag{2.34}$$

This general solution is then applied to the case of a field emitter. As it has been shown in several previous works [31, 69, 70] and as it was mentioned in section 2.1.2, the surface atoms of an atom probe tip are acting as partial ions due to the influence of a very high electric field. This is taken into account by assigning a charge q_i to each surface atom of the emitter. It is assumed that every charge is spread over a certain small area A_i, surrounding the atom i. The area is further assumed to be the same for each atom, which means $A_i = A \,\forall\, i$. Together with (2.34) this yields:

$$\frac{q_i}{A} = \frac{1}{2\pi} \sum_{k=1,k\neq i}^{N} q_k \frac{\vec{n}_i \cdot \vec{r}_{ik}}{|\vec{r}_{ik}|^3}. \tag{2.35}$$

Here the vector $\vec{n}_i$ is the normal vector of the emitter surface at the position $\vec{r}_i$ of the atom i and the vector $\vec{r}_{ik} = \vec{r}_i - \vec{r}_k$ connects the atoms i and k. In order to make equation (2.35) physically meaningful, it has to be divided by $2\,\varepsilon_0$. The combination of (2.34) and (2.35) provides the algorithm, which can be applied to the case of a field emitter. Starting with an arbitrary charge q_0 at each surface atom, the following iterative formula can be used to find the equilibrium charge distribution:

$$\frac{q_{i,n+1}}{A} = \frac{1}{2\pi} \sum_{k=1,k\neq i}^{N} q_{k,n} \frac{\vec{n}_i \cdot \vec{r}_{ik}}{|\vec{r}_{ik}|^3}. \tag{2.36}$$

In each iteration step, the total amount of charge has to be conserved. This is done by adjusting the small surface element A after each step, so that $\sum q_{i,n+1} = \sum q_{i,n}$. The calculation of the surface charge values is repeated, until all individual changes $\Delta = q_{i,n+1} - q_{i,n}$ from one step to another becomes smaller than a user-specified threshold.

The development of the charge distribution during iteration starting with a homogeneous configuration can be seen in figures 2.15a) and 2.15b):

As it can be seen in figure 2.15b), the atoms located at the edges of a crystallographic plane are carrying the largest amount of charge in the equilibrium state. This observation corresponds to the fact that surface atoms at the edges of crystallographic planes are most likely to be field evaporated during an atom probe experiment. The high evaporation probability stems from the proportionality between the squared partial charge and the force

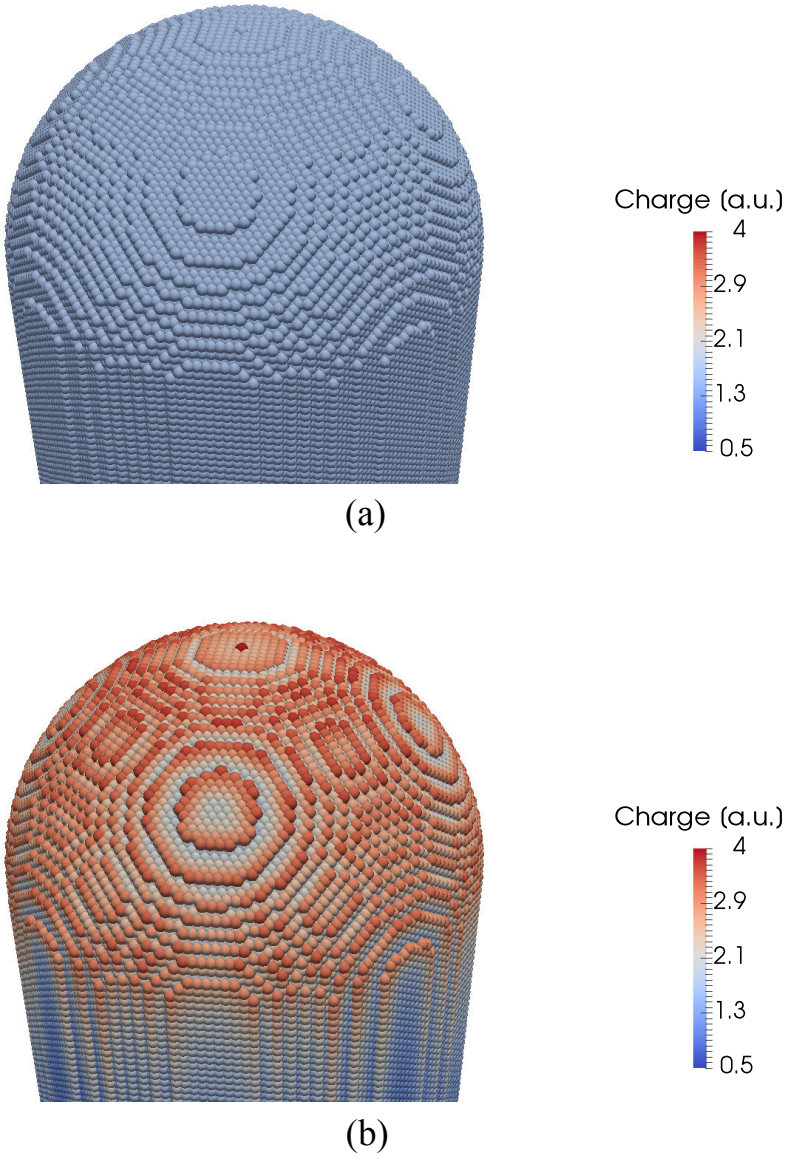

Figure 2.15.: Development of the charge distribution at the surface of a field emitter. Starting with a homogeneous distribution (a) the iterative method of equation (2.36) has been applied. Already after the first step, the charge distribution has changed drastically (shown in (b)) and is already very close to the equilibrium configuration under the given geometry. The changes after further iteration steps are hardly visible and therefore, they are not shown.

acting on a surface atom, which can be derived with the help of Coulomb's law:

$$\vec{F}_i = \frac{1}{4\pi\epsilon_0} \sum_{k=1,k\neq i}^{N} q_i\, q_k\, \frac{\vec{r}_{ik}}{|\vec{r}_i k|^3}. \tag{2.37}$$

The individual probability for evaporation is considered to be proportional to the stress $\gamma_i = F_i/A$ at each surface site covering the area A [71]. Combining equation (2.37) with (2.35), the evaporation probability equates to:

$$p_i = \frac{q_i^2}{2\epsilon_0 A^2}. \tag{2.38}$$

The outlined scheme for the determination of an equilibrium charge density is essential for the subsequent trajectory calculation.

2.4.1. Trajectory calculation

The calculation of ion trajectories in the presence of a charged emitter surface is performed by an integration of Newton's law with the help of a Runge-Kutta method as it is described in [72]. The determination of the force, acting on the particle is done via the application of equation (2.37). The only difference is that the charge q_i now refers to the charge state of the emitted ion and the vector $\vec{r}_{ik}$ is a function of the ion's current position.

In order to reduce the computational cost of the calculation of the sum in equation (2.37), the atoms at the tip surface can be organized in an octree-structure (see [67]). In this octree, every node refers to a cubic cell in the simulation space, which contains a certain amount of charged surface atoms that are located inside the cube. The octree is composed of a large cube (the *root*) covering the whole simulation space, which is further divided into eight smaller cubes, the so-called *child* nodes. Each child node might be further subdivided, which leaves them to become an *internal* node. The subdivision is carried out, until each child node does not contain more than a user-specified amount of surface atoms. The smallest cubes in the octree that are not subdivided any more a called *leafs*.

The determination of the force acting on the field-evaporated ion could be carried out by considering all surface atoms in the leafs of the octree (all atoms at the tip surface respectively). However, many surface atoms are located in a considerably large distance to the ion. Therefore, the contribution of those surface atoms to the sum in equation (2.37) is small. In order to save time, those atoms with a large distance to the ion are being "summarized" with the help of the octree. For each internal node, the center-of-charge is calculated considering all surface atoms contained inside the internal node's cube. The center-of-charge $\vec{r}_c$ is given by the sum over all N_j coordinates $\vec{r}_j$ of the atoms confined in the internal node, weighted by their individual charge q_j:

$$\vec{r}_c = \sum_{j=0}^{N_j} q_j \cdot \vec{r}_j. \tag{2.39}$$

Obviously, the charge of this summarized internal node is given by the sum of all charges q_j. If the distance of the center-of-charge to the ion is larger than a user-specified value, the contribution of all atoms confined in the internal node to the sum in equation (2.37) is given by the charge and the coordinates of the center-of-charge.

Due to this simplification, the summation in equation (2.37) might be drastically reduced, yielding a faster flight path integration. The same scheme is also applied to the calculation of the equilibrium charge distribution prior to the emission of an ion, described in section 2.4. Regarding the performance of the entire process, this turns out to be even more critical.

In the case of a reconstruction performed with the technique described in section 3.2 the charge distribution on an arbitrary atom probe tip is computed and the resulting ion trajectories starting from several different positions at the respective emitter surface are taken into account. The basic idea for a reconstruction technique, based on the trajectory calculation is presented in the following chapter.

Chapter 3.

Reconstruction on a discrete tip surface

In this chapter a first important step towards an improved reconstruction technique is made. To this end, the capability of the general concept is demonstrated by inverting the simulated field evaporation. In section 3.1, the principle of the reconstruction method is briefly described. Subsequently, the exact tip structure after the simulated atom probe experiment is taken and the field evaporated volume is reconstructed with the help of calculated realistic ion trajectories.

In section 3.2 the approach is further elaborated in order to make it more versatile. Here, the algorithm is no longer working on a predefined lattice, which allows a higher degree of freedom for finding the position of each detected ion in the reconstruction. The advantages and limitations of this technique are discussed based on example calculations for characteristic simple emitter structures.

3.1. Proof of principle on a rigid lattice

As a first demonstration of the beneficial effect of the consideration of ion trajectories in the reconstruction process, the simulated FEV is inverted. The results of this study have been published in [11]. This means that the field evaporated emitter volume is built up opposite to the order of the evaporation. Atoms that have been detected last are the first to be reconstructed. In each step, the current surface structure of the atom probe needle is considered for the calculation of ion trajectories.

The situation in each reconstruction step within this simple approach is illustrated in figure 3.1. The number of candidates for the reconstruction coordinates are limited to the lattice positions, which are located at the momentary tip surface. The algorithm chooses one of these candidates as the respective reconstruction coordinate belonging to the current measured detector event. To this end, for every candidate position a trajectory is calculated. Afterwards, the trajectory corresponding to the impact position closest to the measured ion

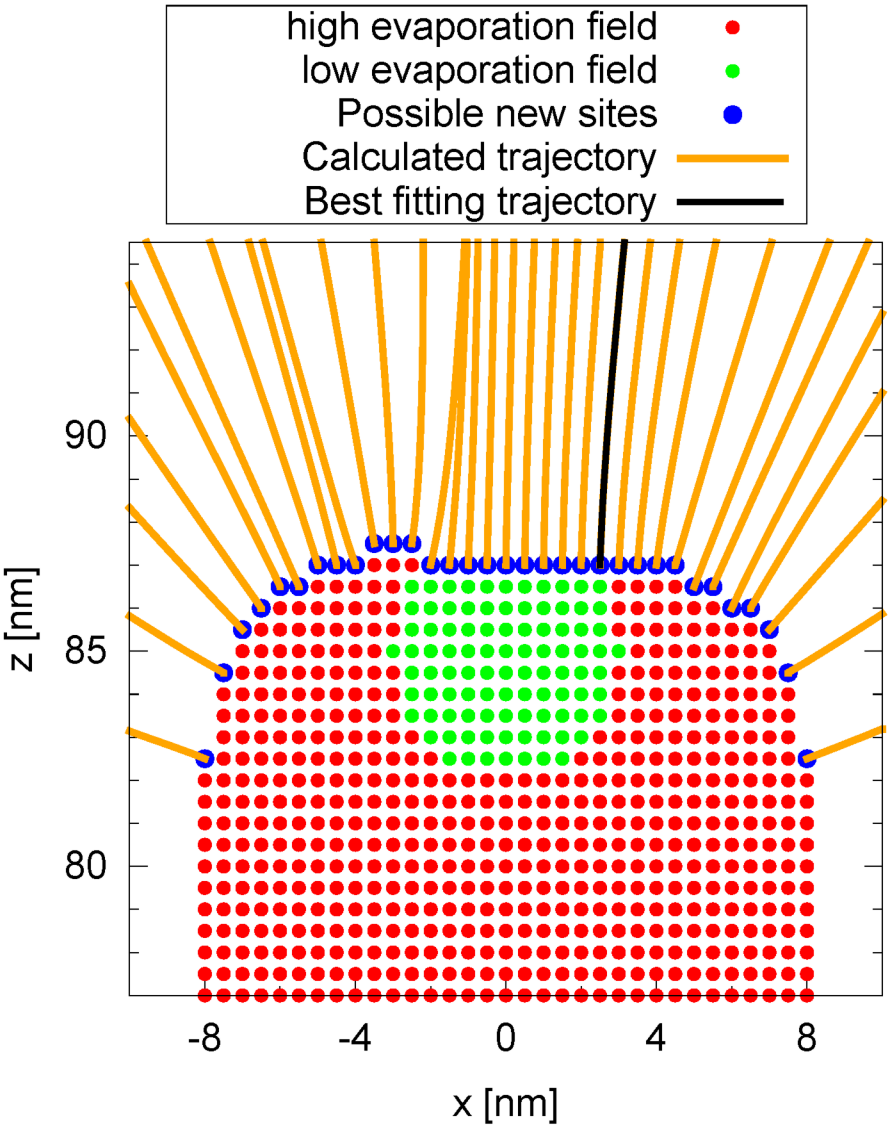

Figure 3.1.: Reconstruction approach on a rigid lattice. In every step of the reconstruction, a discrete set of candidate positions for the next atom is defined (blue dots). These positions belong to the lattice of the former emitter structure (containing two different atomic species), which has been field evaporated. They are located in direct vicinity of the current tip surface. Subsequently, trajectories are calculated and their respective hit positions are compared to the measured impact coordinates of the current event. The starting point of the best matching trajectory (black line) defines the reconstruction coordinates of the detected ion.

impact is identified. The starting point of this particular trajectory is finally chosen as the reconstructed coordinate.

Before the algorithm can continue with the next measured event, the emitter surface needs to be updated, since one atom has been added and other atoms below might no longer be considered as surface atoms. In addition, the surrounding electrical potential needs to

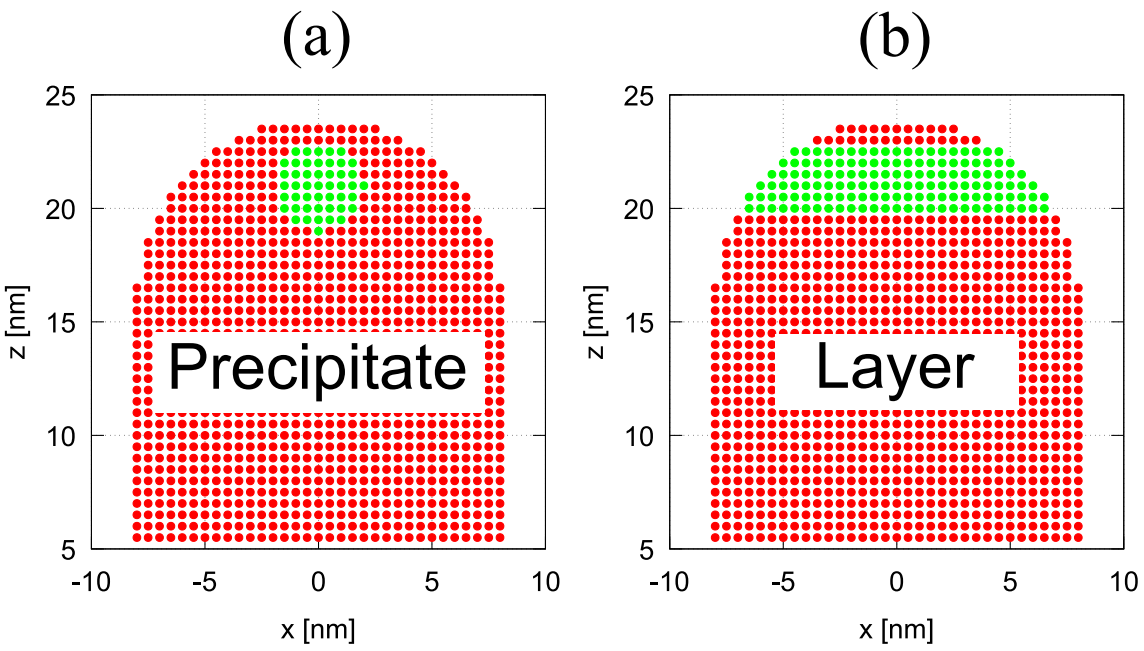

Figure 3.2.: Slice through the reconstructed emitter structures for the reconstruction on a rigid lattice [11]. In (a) the precipitate with a 50% lower or higher evaporation field in comparison to the surrounding matrix (red) is illustrated. The respective tip volume containing a layer structure is shown in (b).

be recalculated according to the new situation. The potential value of the new surface atom is set to the same constant value as the other atoms belonging to the tip. In close vicinity, this is causing changes of the electrical potential. Once the potential has been recalculated locally to sufficient accuracy, the algorithm is ready to deal with the reconstruction of the next detected event and the same procedure is repeated.

This method has been applied to different test samples, each of them containing two atomic species. The simulated data sets contained approximately 5000 atoms and 8000 atoms respectively. One of those emitter samples contained a spherical precipitate inside a surrounding matrix. The other structure contained a layer, orientated perpendicular to the tip axis. For both emitter structures, two different cases have been investigated. In the first, the spherical particle or the layer had a 50% higher critical evaporation field than the matrix atoms. In the other case, the evaporation field was 50% lower (see figure 3.2). Such a large difference regarding the evaporation field would cause severe artifacts when using the conventional geometric reconstruction approach. The results derived by the conventional point projection approach are given in the appendix in figure A.1 for the precipitate structure and figure A.2 for the layer structure.

By contrast, the trajectory-based technique could rebuild the tip structure exactly in all studied cases as illustrated in figure 3.2. At this point it has to be mentioned that the comparison between the fundamental concepts is biased to some extent. The exclusive

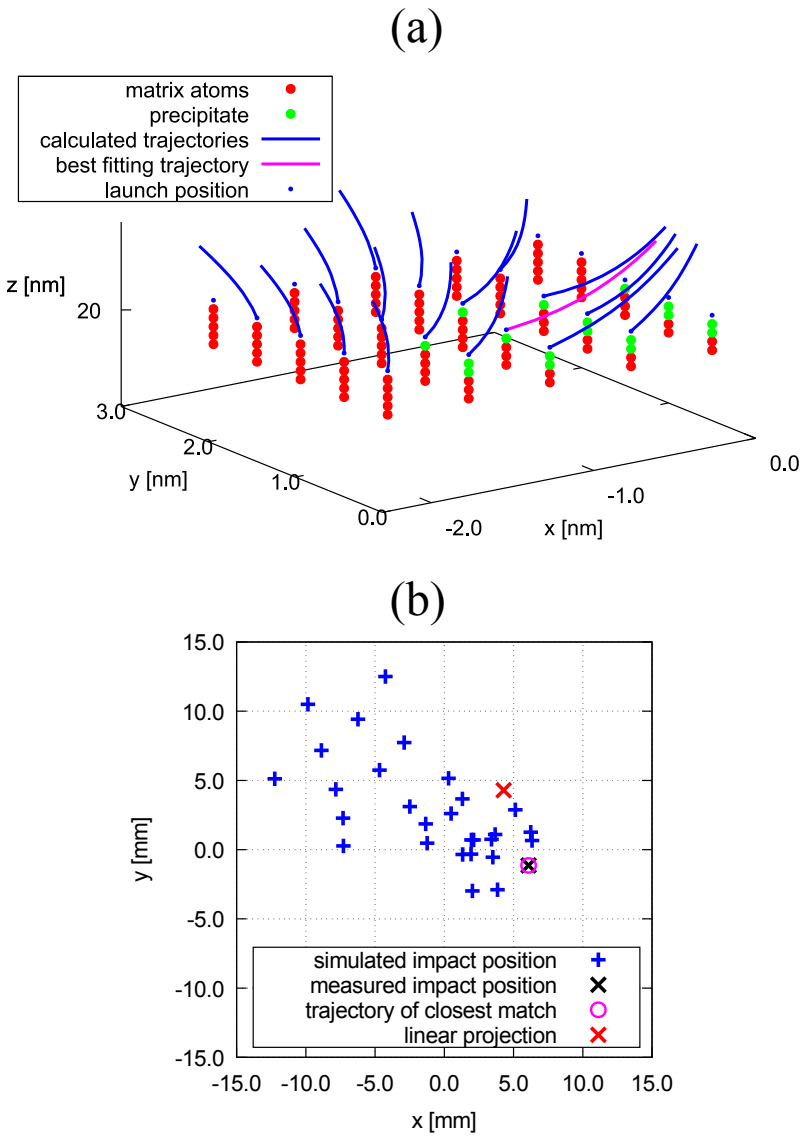

Figure 3.3.: The deflection of ion trajectories on the tip surface in the case of a precipitate with a lower evaporation threshold is shown in (a). In (b), the respective impact positions on the detector together with the hypothetical impact position (called "linear projection") needed for the correct reconstruction by the standard technique is plotted. (data taken from [11])

selection of candidate coordinates belonging to the predefined lattice structure guides the developing reconstruction into the correct direction and excludes several sources of potential errors. The strong deflections of ion trajectories in vicinity to the precipitate shown in figure 3.3a), causing strong artifacts when applying the conventional approach, can already be avoided in this simple scheme.

In order to point out the severe influence caused by ion deflections, figure 3.3b) demonstrates how beneficial the use of realistic ion trajectories can be. The blue daggers in the plot represent the impact positions of the considered sample trajectories that started at

various surface sites in a specific stage of the reconstruction of the low field precipitate example, when the precipitate is covering a certain amount of the tip surface. They correspond to the blue trajectories in figure 3.3a). Accordingly, the best matching trajectory, which is plotted in purple in figure 3.3a) corresponds to the impact given by the purple circle in b). This trajectory ends extremely close to the measured position (black cross in the plot). For comparison, in figure 3.3b) the hypothetical impact position, which would be needed for the conventional point projection approach to yield the correct reconstruction coordinate for the considered ion is indicated by a red cross. This position is located approximately 5 mm away from the measured impact. In this example it can impressively be observed that strong ion deflections cannot be sufficiently taken into account by the standard technique and the consideration of trajectories has the potential to improve the reconstruction.

In order to make the new technique applicable to realistic situations, where the exact lattice structure of the field evaporated volume is not known, the method is further extended in section 3.2. Nevertheless it should be mentioned that the idea of positioning atoms on a predefined lattice is not uncommon. In the past, the so-called *lattice rectification* technique has been proposed [73, 74]. Here the atoms are repositioned onto the positions of a certain lattice structure after performing the standard reconstruction approach. The lattice structure is extracted from the initial reconstructed volume by applying crystallography characterization techniques (e.g. spatial distribution maps [75]).

3.2. Reconstruction without a rigid lattice

In section 3.1, a first step towards a trajectory-informed reconstruction of atom probe tomography data has been introduced. This method needs to be further improved, so that it no longer relies on the knowledge of the lattice structure of the measured tip. The algorithm should be able to find a reasonable position for each atom without any kind of a predefinition of possible positions.

An improved realization of the trajectory-based method works as follows: Starting with a reasonable guess for the reconstruction coordinates, the algorithm approaches the final surface position of the next atom step by step. This approach towards a surface coordinate, which delivers a sufficiently close trajectory impact position, is performed by a well-known optimization algorithm, e.g. the simplex algorithm of Nelder and Mead [76]. This algorithm repetitively calculates trajectories starting at several different positions. The vertices of the simplex represent these starting positions. During the process, the simplex is shrinking more and more, until its size is sufficiently small. Then the vertex of the simplex,

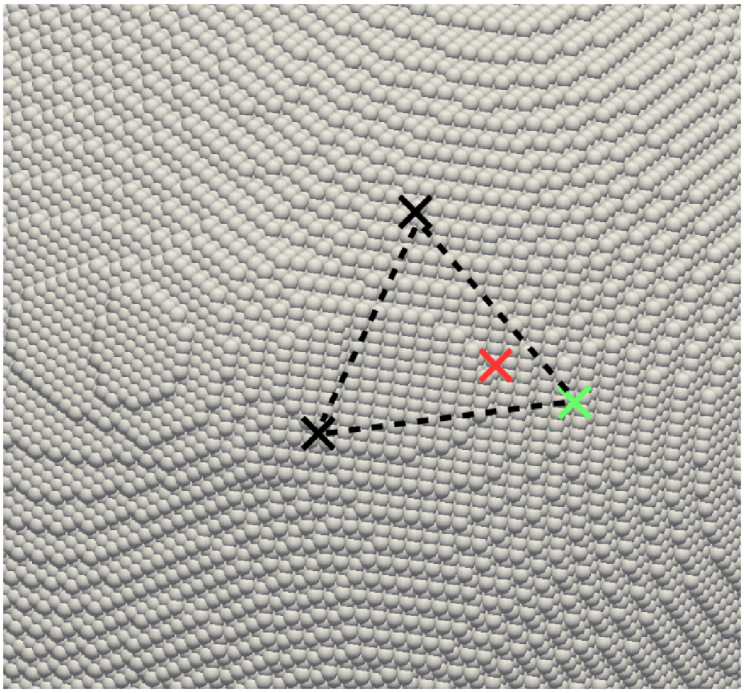

Figure 3.4.: Illustration of the simplex algorithm in the case of the free reconstruction approach (top view of the tip surface). The surface atoms are represented by hard spheres. The correct reconstruction coordinates (represented by the red cross) are iteratively found. The simplex algorithm chooses 3 different start positions for the trajectory calculation (black and green crosses). At any time, one of the sample positions delivers the currently best result (green). The triangle defined by the three start coordinates is shrinking during the search for the best solution. Once the size of the triangle is sufficiently small, the reconstructed position is given by the start position of the best matching trajectory.

corresponding to the best matching ion trajectory, is chosen as the final reconstruction coordinate. In this case, the simplex is two-dimensional, which means, it has a triangular shape (see figure 3.4).

The x- and y-coordinates for the starting positions on the surface are given by the simplex algorithm. The respective z-coordinate is then defined by a simple projection of these two-dimensional coordinates onto the emitter surface, given by the surface atoms represented by hard spheres. The application of this scheme to a simple fcc structure is shown in figure 3.5. As it can be seen from the reconstructed emitter volume, this "improved" reconstruction method results in the formation of artificial structures on the tip surface. These chains are composed of reconstructed atoms that are stacked upon each other. This chain formation is clearly wrong and must be an artifact of the applied technique.

Indeed, a physical explanation for the observed phenomenon could be the lack of accuracy. The reconstruction coordinate found in each step might be close to the correct position, but

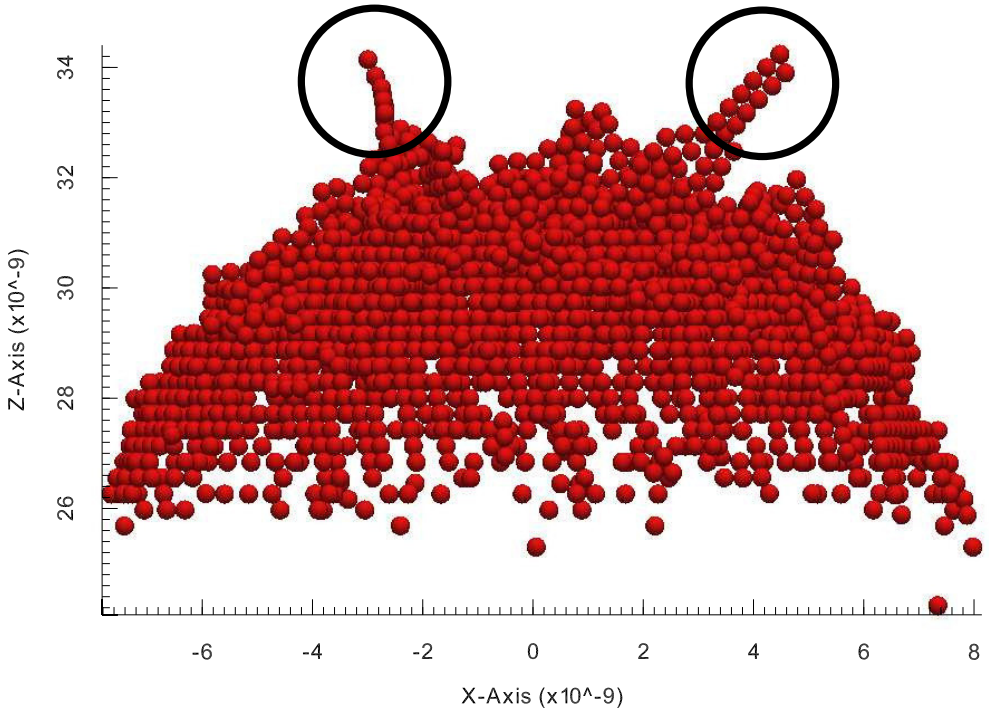

Figure 3.5.: Reconstruction of a small emitter volume with an fcc structure derived by applying the trajectory-based scheme without the help of a rigid lattice. Due to small inaccuracies regarding the positioning of the atoms on the emitter surface, chain-like structures (encircled) can be observed.

nevertheless, due to a limited precision of the calculation of the electrical potential and the force, the perfectly correct position is not found in the majority of cases. In addition, the correlation between the starting positions of the trajectories on the surface and the impact positions on the detector cannot be expected to be unique. Caused by trajectory overlaps, different locations on the tip might yield to the same impact detector position within the given degree of accuracy.

The formation and growth of the demonstrated chain structures can then be understood by considering the strong effect of small protrusions on the flight path of the ions. Once a small number of atoms, or in some cases even one individual atom, is occupying a position, which slightly sticks out of the emitter structure, ion trajectories starting in the direct neighborhood experience a strong deflection. The consequence of this deflection effect is significant.

The trajectories starting on top of the protrusion compete with the trajectories starting from other, more reasonable surface sites (see figure 3.6). Due to the large area on the detector, which can be reached from the top of the protrusion, the algorithm might have to make a choice between several almost equally sufficient matching surface positions. In those cases, depending on the actual distance to the measured impact, atoms might by

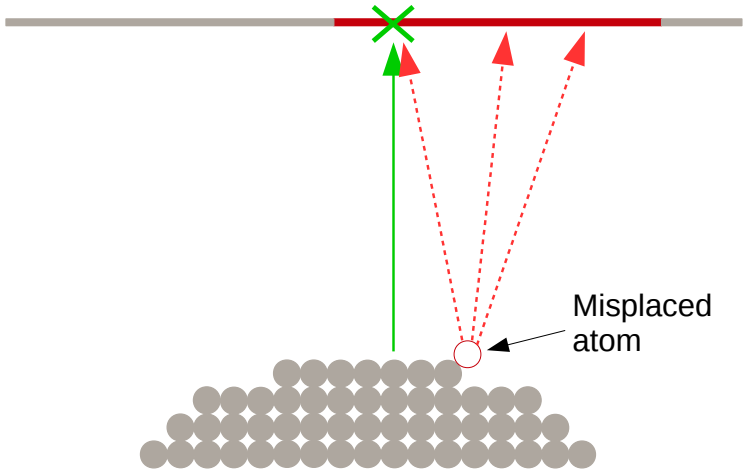

Figure 3.6.: Mechanism leading to chain-like protrusions on the emitter surface. The trajectories starting on top of the protrusion (red dashed arrows) compete with the trajectory originating from a more reasonable surface location (green arrow). Because of the relatively large accessible area for ions starting from the protrusion (red bar on the detector), the chain structure is very likely to grow, since atoms might be reconstructed on the top of the chain by mistake.

mistake be reconstructed to a completely wrong location. In this case the artificial chain structures will grow and their influence on the reconstruction will even be amplified.

As a consequence of this self-focusing to protrusion, a reconstruction algorithm without any kind of constraint is highly unstable. Since small errors in the positioning of atoms on the emitter surface cannot be excluded entirely, these deviations from the perfect reconstruction position would lead to a self-amplifying formation of artifacts. A reasonable result for the reconstructed emitter volume could no longer be expected, as soon as the mechanism described above and illustrated in figure 3.6 dominate the whole process.

In order to address this challenge, the reconstruction method needs to be refined further, so that the formation of such self-amplified protrusions is avoided. In section 3.2.1 such an amended procedure is presented.

3.2.1. Introduction of an inter-atomic potential

In section 3.2, the challenges regarding the self-amplified growth of protrusions arising during the reconstruction have been discussed. Since the growth of such structures can hardly be stopped once they have reached a certain height relative to the surrounding surface, they need to be excluded completely from the very beginning.

To this end, the reconstruction should still be performed without the constraint of a predefined rigid lattice, but with guiding help of a weak interaction. This extension is given by the application of a simple inter-atomic potential at each probed surface position.

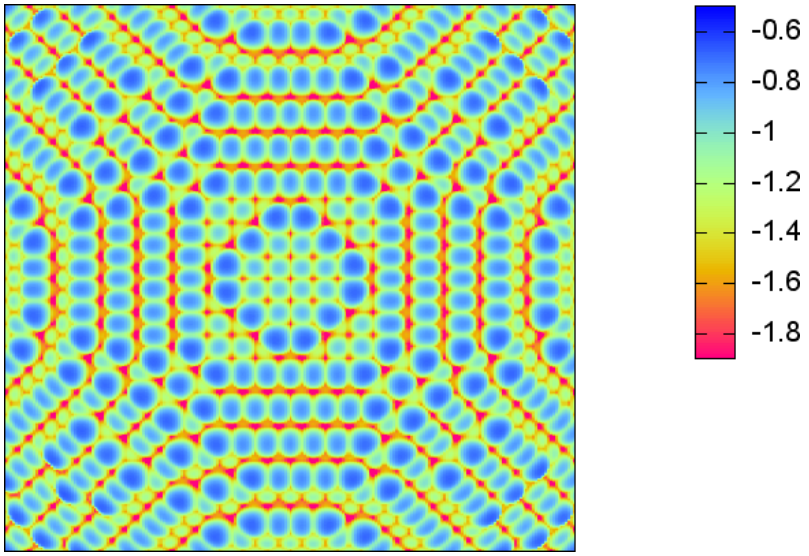

Figure 3.7.: Top view of the sampling of a bcc emitter structure ([001] orientation) with a Lennard-Jones pair potential according to equation (3.1). The lowest values are obtained at the edges of the crystallographic planes.

The strength of this potential acts as a second criterion for the selection of a reconstruction position for each detected ion. Alongside the search for a position, which delivers a minimum distance between measured and calculated impact positions on the detector, the intention behind the use of an inter-atomic potential is to guide the algorithm towards surface sites with a large number of neighboring atoms. This property should be well suited for the task of rebuilding the field evaporated volume with a high density. The possibility of stacking atoms upon each other becomes more unfavorable because the number of direct neighbors, or the number of atomic bonds to other surface atoms respectively, would be very low, compared to other locations on the current emitter surface.

The idea of "measuring" the amount of atomic bonds at every probe position can be realized by applying a simple pair potential, for example the Lennard-Jones potential:

$$V_{LJ}(r) = \varepsilon \left[\left(\frac{r_0}{r} \right)^{12} - 2 \left(\frac{r_0}{r} \right)^{6} \right], \tag{3.1}$$

where r is the distance between the two interacting atoms and r_0 represents the atomic distance, for which the potential shows a minimum. The absolute depth of the potential ε is irrelevant in the following application of equation (3.1).

When the emitter surface is sampled and the value of the pair potential is calculated at each position, the resulting potential landscape might look as it is shown in figure 3.7 for the example of a bcc structure. As a consequence of the different pair potential values at the surface as shown in figure 3.7, a dense packing of the reconstructed tip volume could

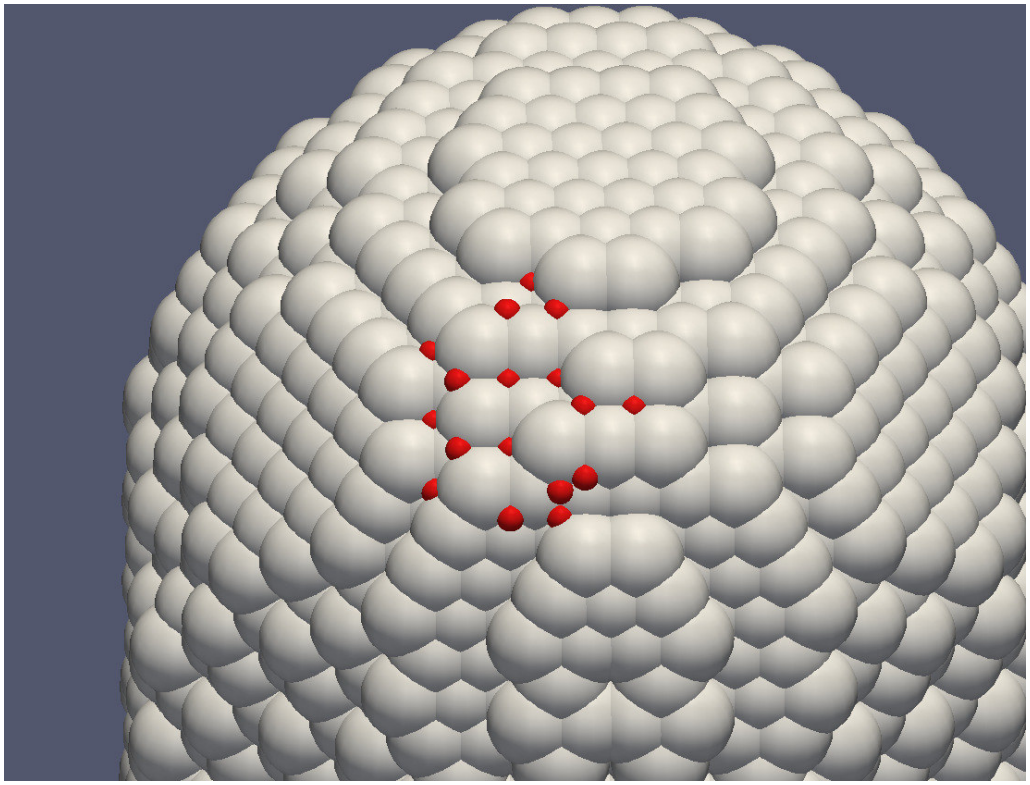

Figure 3.8.: Local minimum values of the Lennard-Jones potential applied on the surface of an atom probe tip. The red spheres represent the resulting coordinates of the search for minimum potential values. These positions define the final set of candidates for the reconstruction.

be achieved, if only local minimum positions of the applied Lennard-Jones potential were considered as possible trajectory starting points. Consequently, the selection of possible reconstruction coordinates needs to be restricted again.

In every step, prior to the calculation of any ion trajectory, the emitter surface has to be searched for local minimum values regarding the Lennard-Jones potential in the vicinity of a reasonably guessed position. This can conveniently be done with the help of a conjugate gradient method [77] or the already mentioned simplex algorithm. A sufficiently large number of sample points around the guessed position provides the gradient method with start coordinates. Then for each of those initial locations on the surface, the search for a close minimum of the pair potential is performed, until the gradient method converges. The result of such a search is shown in figure 3.8.

Once the final set of possible candidates for the reconstruction is known, the algorithm starts to simulate ion trajectories originating from each local minimum of the pair potential. The remaining task in every reconstruction step is to make the final choice for the resulting reconstruction coordinate. Since in this case, a second measure for the quality of any candidate position besides the trajectory impact position is available, a combined criterion

can be applied. In this work, the combined measure $\rho(\vec{r})$ is given by the ratio of the distance between simulated and recorded detector position d, and the value of the pair potential $P_{LJ}(\vec{r})$:

$$\rho(\vec{r}) = \frac{P_{LJ}(\vec{r})}{d}. \tag{3.2}$$

In this way, the candidate with the lowest value for ρ defines the final position for the reconstruction of the next atom.

In the following, the results of the application of the above described procedure to several different small emitter structures are presented. In all cases, the reconstruction started with the remaining tip surface after the simulated evaporation.

The first test specimen is a rather small needle with a tip radius of 4 nm and an fcc lattice structure. The lattice orientation was chosen so that the [111]-direction shows in the direction of tip axis. The characteristic feature of the emitter volume is a 1.0 nm thick layer with a 50% lower evaporation field in comparison to the surrounding matrix atoms. The detected data set contains 5000 atoms. In figure 3.9a), a slice through the tip is shown before evaporation. The information about the lattice structure can be seen in figure 3.9b). Here, a lattice identification tool contained in the software package *Ovito*[1] has been used, in order to verify the presence of an fcc lattice and to provide the plot in figure 3.9b) as a reference for the later reconstruction [78]. The tool performs a common neighbor analysis according to [79], which is a typical choice for the task of lattice identification [80].

It can be observed that all atoms except for the surface atoms are colored in green. This means that the bulk atoms belong to the same fcc lattice. For the surface atoms, a matching lattice structure could not be found, since a sufficient number of neighboring atoms is needed for the identification algorithm.

The corresponding images for the result of the reconstruction performed with the above presented algorithm are shown in figure 3.9c) and d). In c), the former thin layer can easily be identified in the reconstruction, even though the difference in the evaporation field was severe. Nevertheless, the reconstruction is not perfect. In the bottom and especially at the outer part of the volume some slightly misplaced atoms appear. This circumstance also results in a loss of the information about the lattice structure at the bottom. Interestingly, the fcc lattice is reestablished in the following layers, which indicates at least a certain robustness of the technique against local disturbances, since the structure is build up from the bottom to the top. The reason for the misplaced atoms most probably stems from numerical inaccuracies in the calculation of the charge density on the surface. Even very small misplacements of atoms in the vicinity of a trajectory starting point might already

[1] http://ovito.org/

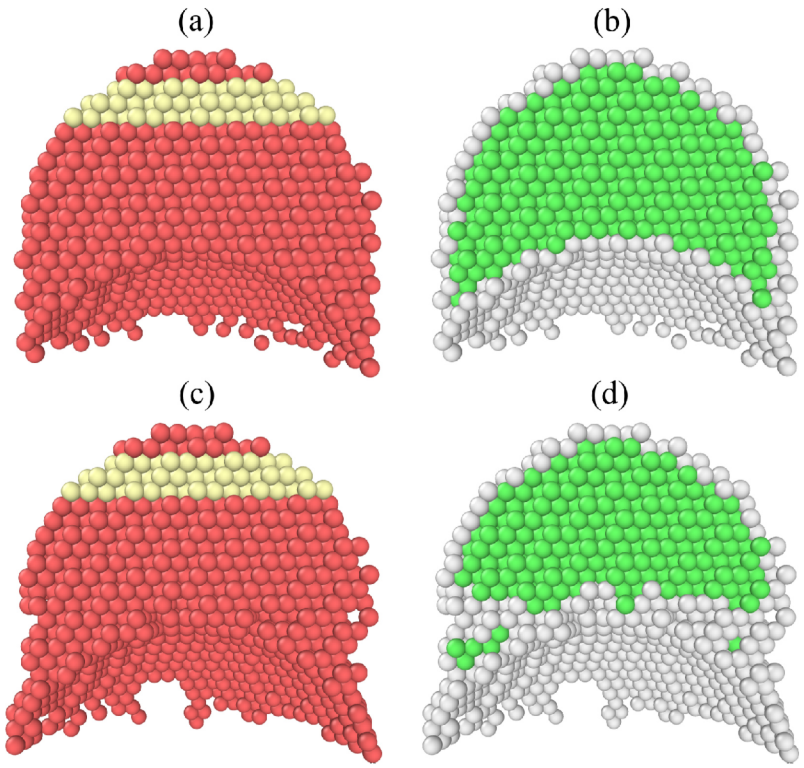

Figure 3.9.: Reconstruction of a layer structure. The plot in (a) shows the original emitter volume for a small fcc structure with [111] orientation along the tip axis prior to the FEV. The corresponding identification of the lattice structure is shown in (b). Green atoms could be identified to belong to the former fcc lattice. In (c), the reconstructed volume is shown. The corresponding plot for the identification of the lattice structure at each atomic site is provided in (d).

lead to a sufficiently large deflection of ions and consequently to more errors.

The second tested sample also had an fcc lattice structure containing a spherical particle with a 50% higher evaporation field than the surrounding matrix. The tip radius was also chosen to 4 nm. Due to the computational cost of the algorithm at the moment of this investigation, the reconstructed emitter volume had to be limited to just 5000 atoms, which is much smaller than a typical data set of a real experiment.

In figure 3.10c), a slice through the resulting reconstruction is shown. In this case, the reconstructed volume matches exactly to the evaporated volume (shown in a)), which means that this particular test was completely successful. In order to support this statement, figure 3.10d) shows an analysis of the lattice structure in the reconstructed volume. Green atoms belong to an fcc lattice, while no particular lattice structure could be assigned to the white atoms at the surface. Since only atoms at the surface appear white, this presentation underlines the successful performance of the algorithm because the identification of the lattice structure only works for bulk atoms (as already mentioned above).

Overall, the observation of the capability of the technique to deliver the correct lattice

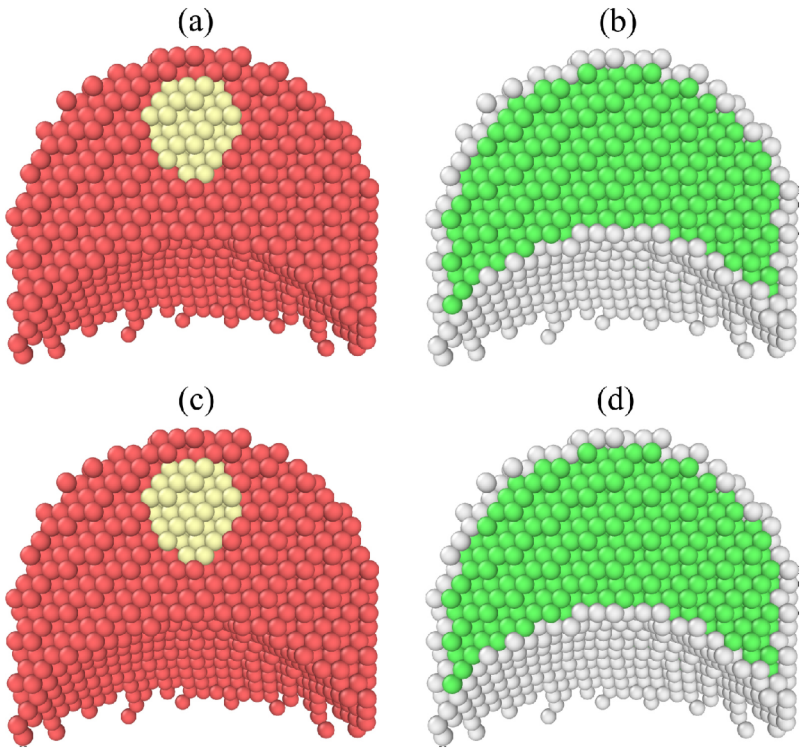

Figure 3.10.: Reconstruction of an emitter structure with a spherical precipitate. In (a), the original volume for a small fcc structure with [111] orientation along the tip axis and a spherical particle with a higher evaporation field compared to the matrix is illustrated. The corresponding identification of the lattice structure is shown in (b). Green atoms could be identified to belong to the former fcc lattice. In (c), the reconstructed volume for the same data set is shown. Again in (d), the identification of the lattice structure at every atom position is visualized.

structure is quite remarkable, since the cohesive energy of an fcc crystal is almost equal to the cohesive energy of an hcp lattice structure when applying a Lennard-Jones potential (see [81] on page 59). In fact, the hcp structure even has a slightly lower cohesive energy. For the fcc structure the cohesive energy amounts to -2.32204, while for the hcp structure its value is given by -2.3226. Due to small inevitable misplacements of individual atoms, one could imagine that the former fcc structure might switch into an hcp structure because the hcp lattice sites could become more favorable. On the other hand, the transition to another lattice structure incorporates the formation of an interface. The energy needed to build such an interface can be expected to overcompensate any gain of cohesive energy by lattice transformation.

Obviously, the application of an inter-atomic potential as a guidance for the algorithm leads to a significant improvement and helps to avoid artificial surface roughness and the formation of the chain structures shown in figure 3.5.

Nevertheless, a useful reconstruction tool must also be able to deal with the consequences of a limited detector efficiency, which is affecting every real measurement. The typical

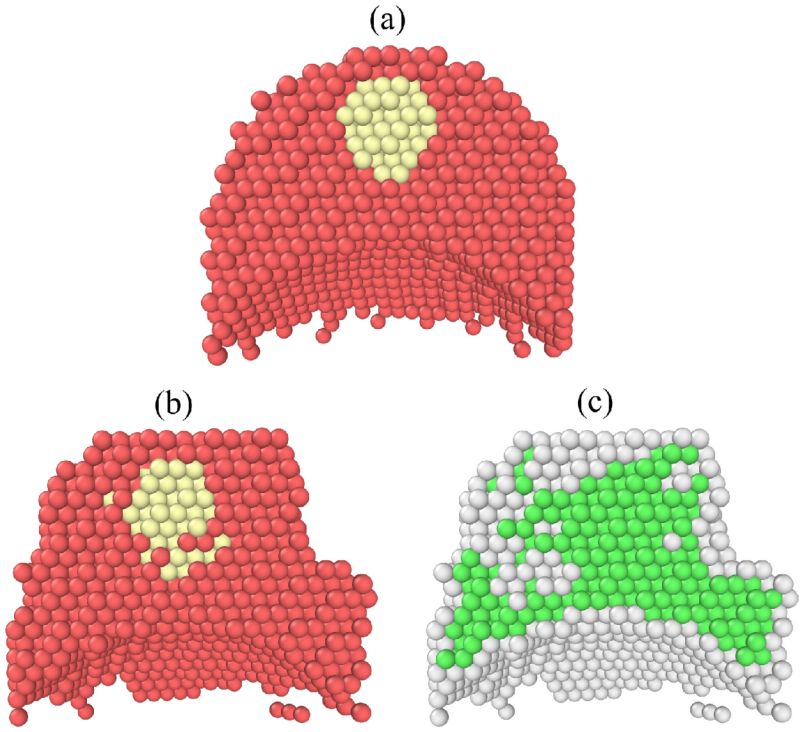

Figure 3.11.: Influence of a limited detector efficiency. In (a), the same original volume as already shown in figure 3.10(a) is illustrated. In (b), the result for the reconstruction with a detector efficiency of 99% is shown. The corresponding information about the lattice structure in the reconstructed volume can be seen in (c).

efficiency of a position-sensitive detector used in an atom probe device amounts to only 50%, in modern devices an efficiency of 80% is achievable. In order to investigate the performance of the algorithm in cases, where a significant portion of the evaporated volume is missing in the measured data set, the data set containing the spherical precipitate in figure 3.10 has again been reconstructed. In contrast to the test before, 1% of the detected atoms has been removed randomly from the list of measured events. The resulting tip volume in figure 3.11b) already shows a clear deformation in general, even though the detector efficiency is still much better than in a real atom probe experiment. Fortunately, the precipitate itself can still be identified as a dense coherent particle but it already becomes slightly distorted. The lattice structure of this reconstructed volume shown in figure 3.11c) is no longer as constant as before. Especially in the left part of the illustrated slice through the emitter volume, the fcc lattice structure could not be identified anymore. This effect is not limited to the very surface of the tip but reaches far into the bulk.

The deformation of the tip is of course to some extend explainable by the missing volume. The most interesting observation of this little numerical experiment is the fact that the former fcc structure is already lost in a fairly large part of the volume. This loss of information

about the lattice structure could obviously not be repaired by either the influence of the inter-atomic potential or the trajectory calculation. Since the effect of missing information in the data set is already significant after the deletion of only 1% of the data, dealing with the limited detector efficiency of a realistic atom probe experiment can be expected to be a very challenging task. It can also be assumed that the main issue in this regard is the effect of the occurring surface deformation/roughness on the charge distribution and consequently the electric field, which defines the ion trajectories. In section 3.2 it was already shown that the effect of even small protrusions or locally increased roughness on the charge distribution has the potential to distort the whole reconstruction. In a situation, where a large amount of data is missing, even the application of an inter-atomic potential might not be enough to prevent areas with an increased roughness, since misplacements of atoms are still likely to occur.

At this point, it is still unclear, how to deal with the discussed consequences of a limited detector efficiency in the context of the approach described above. One might consider to introduce a random insertion of atoms into the reconstructed volume during the reconstruction process. On the one hand, it would be rather easy to overcome the volume deficit in this way. On the other hand it would still be not guaranteed that the occurrence of severe roughness on the tip surface is sufficiently avoided. In addition, the random insertion of atoms to unoccupied surface sites might also lead to trajectory deflections. In an unfortunate situation, such deflections might guide the algorithm into the wrong direction, which would yield misplaced atoms again. In a situation like that, it could be possible that these misplacements occur because of the random atom insertion and would not happen, if no further atoms would have been inserted into the volume randomly.

For the moment, a more robust approach for the reconstruction is needed, which is not affected by missing information. In addition, the computational cost of the technique needs to be reduced drastically for the application to realistic data sets of a few hundred million atoms. To this end, a fundamentally different concept of an improved algorithm is made in chapter 4. In this following case, the trajectory calculation is skipped, since this part of the above presented approach turns out to be very critical and also sensitive to slight misplacements of atoms. Instead of a very precise description of the ion trajectories, the following technique will focus on the dynamic mesoscopic modeling of the surface shape of the emitter. Since the information about the development of the tip shape during FEV must somehow be reflected in the measured data set, this following approach is designed to extract the momentary tip shape from the data set. Instead of focusing on individual events, it rather considers larger parts of the entire measurement data and calculates the corresponding tip shape. This more realistic description of the emitter is expected to deliver substantial improvements for the reconstruction. Regarding the lack of information due to

a limited detector efficiency, it can also be assumed that such an approach is more robust, as long as the detector efficiency is sufficiently homogeneous.

Chapter 4.

Atom probe reconstruction with a varying tip shape

As already discussed in section 2.2.2, the limitation of the conventional point projection method mainly originates from the assumption of a constant emitter shape during the field-evaporation experiment. In the reconstruction shown in figure 2.9b) the influence of a dynamic tip curvature can be observed. Due to the high evaporation field of the precipitate, the tip curvature undergoes a significant change during field-evaporation (see figure 2.9c) and figure 2.10), which yields a significantly broadened precipitate in the reconstructed volume.

The goal of the work described in the following, is to develop a robust reconstruction approach, which is able to detect and consider these changes in the emitter curvature. In this way, the flexibility of the reconstruction technique would be increased and the assumption of a hemispherical tip surface would become obsolete.

Therefore, the main feature of the technique should be the capability to extract the emitter shape at an arbitrary stage of the field evaporation from the local density of measured events on the detector. As a first simplification for our considerations, we still assume rotational symmetry. However, once the tip shape can be described sufficiently precise under this constraint, a reconstruction based on this realistic surface can be expected to show substantially reduced local magnification effects compared to the conventional geometric projection. In addition, the new approach should avoid trajectory calculations, since these calculations are much more time consuming and potentially reduce the stability of the procedure.

In the following, the principle of this alternative approach is outlined. Within the scope of this work, the concept has been published in [12].

In order to test the method, simulated data derived from emitter structures with rotational symmetry will be reconstructed as application examples. Furthermore, a real experimental

data set containing a layer structure of copper and aluminum nitride is reconstructed and discussed in section 4.1.7.

4.1. A new reconstruction approach for emitters with rotational symmetry

The goal of the following technique is the reduction of local magnification effects, which have a strong influence especially when structures contain different materials/phases with strongly varying evaporation fields. In contrast to previous reconstruction approaches, this new method shall not rely on the assumption of constant curvature. Instead, it allows the radius of curvature of the tip profile to change in radial direction perpendicular to the tip axis.

The profile describing the tip surface is being calculated in a straight forward way, only considering the local density of detected events on the detector. In order to take into account the dynamic change of the surface of the measured tip, the profile calculation described in the following, is performed for several larger portions of detected ion impacts. Consequently, a change of the impact pattern on the detector will automatically yield a change in the field emitter profile. The fragmentation of the entire set of measurement data will be further explained in section 4.1.2. In the following section 4.1.1, the derivation of an emitter profile from the density distribution on the detector is presented. The reconstruction will be performed in the same order as in sections 3.1 and 3.2, meaning from the bottom of the detected volume towards the top (last events are reconstructed first). Thus, the observed emitter profile needs to be lifted in order to account for the emitter shrinkage during evaporation. This issue of lifting the profile turned out to be very important for the quality of the reconstruction and is further discussed in section 4.1.4.

4.1.1. Identification of the tip profile

Let us base the following consideration on a few assumptions. First, a linear relationship between the distance D of the impact position of an ion on the detector and the detector center and the emission angle θ of an ion at the tip surface is supposed. This relationship has been well validated experimentally in the past [82], as it can be seen in figure 4.1:

$$D = \kappa L \theta. \tag{4.1}$$

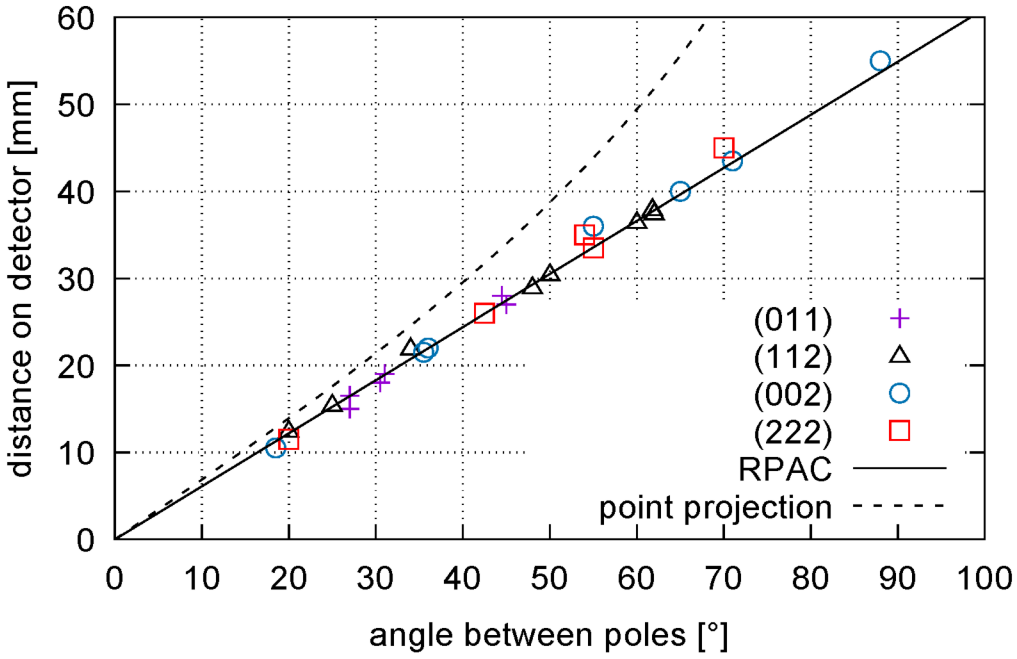

Figure 4.1.: Distances of different poles in the field ion image of a tungsten tip. The observed data is compared with the projection model according to the simple point projection and the radial projection with angular compression ("RPAC") model described in equation (4.1) with $\kappa = 0.61\,\mathrm{mm}/^\circ$. (data taken from [82] and [83])

This relation is an alternative to the linear relation between the detection angle θ' and the emission angle, which is typically considered in the point projection approach by Bas et al. As it can be seen in figure 4.1, both models are suitable to describe the ion projection for a relatively small field-of-view. However, for detection angles larger than 30°, the projection relation of equation (4.1) should be preferred. In the literature, this projection law is called *radial projection with angular compression* [18] or *azimuthal equidistant projection* [84]. Since the versatility of this law regarding the FOV is higher, it has been taken into account for the here presented reconstruction technique. The flight length L and the *image compression factor* κ in equation (4.1) are instrument constants, which need to be known in order to ensure a reliable result for the reconstruction. As a consequence of this relationship, trajectory overlaps, which have been presented in section 3.1 and especially in figure 3.3, need to be neglected.

The second important assumption for the new method is that each tip surface profile, which is later identified, belongs to a steady-state situation of the previous field evaporation. The term steady-state situation imposes that the shape of the field emitter can be considered to be constant for a certain time during the evaporation process. In order to calculate these temporarily constant tip profiles, the detector needs to be divided into several concentric

rings. This ring tessellation is also done with the tip profile, which is still to be identified in detail. The number of rings belonging to the detector tessellation and to the profile is the same, which means, each of the detector rings corresponds to one of the profile rings, describing the tip surface. Every ring on the detector represents a defined interval of detection distances from the detector center. According to equation (4.1), this directly translates to a well-defined range of polar emission angles on the emitter surface. Every profile ring is characterized by a fixed inclination/emission angle θ_i, matching the average detection distance D_i of the associated detector ring (see fig. 4.2). The remaining task for the reconstruction algorithm is the calculation of the nodes defining the surface profile. Each node is given by the pair of two values of radius r_i and the respective height h_i. Every ring contained in the final emitter profile is bordered by two nodes.

As a consequence of the steady-state assumption, the amount of detected ions on one detector ring is proportional to the evaporated volume V_i in the corresponding surface segment (see figure 4.2c)). The volume can be identified as the projected surface area A_i of an individual profile segment onto the base cross-section of the emitter multiplied by the shrinkage Δz. Due to the fixed inclination angle of the profile segments, the projected surface area A_i of segment i is given by its surface area A_i^* multiplied by an angle-dependent projection factor:

$$A_i = A_i^* \cdot \cos(\theta_i). \tag{4.2}$$

For every portion of the measured data set, the corresponding emitter profile is identified. This is done ring by ring, from the center towards the outer part of the surface profile. Starting with the first point of the profile at the center $r_0 = 0$ and $h_0 = 0$ the following points of the tip profile are determined by the recursive evaluation of

$$r_i = \sqrt{\frac{N_i}{\pi\, N_{tot}}\, A_{Tip} + r_{i-1}^2} \tag{4.3}$$

and

$$h_i = h_{i-1} - \tan(\theta_i) \cdot (r_i - r_{i-1}). \tag{4.4}$$

In equation (4.3), the fraction of measured atoms in the i$^{\text{th}}$ detector ring N_i, and the total amount of measured ions N_{tot}, as well as the overall cross-sectional area A_{Tip} of the measured tip section are needed. An iterative application of equations (4.3) and (4.4) finally delivers the resulting emitter profile associated with the current portion of data.

Once the surface profile has been identified, a certain amount of the atoms considered

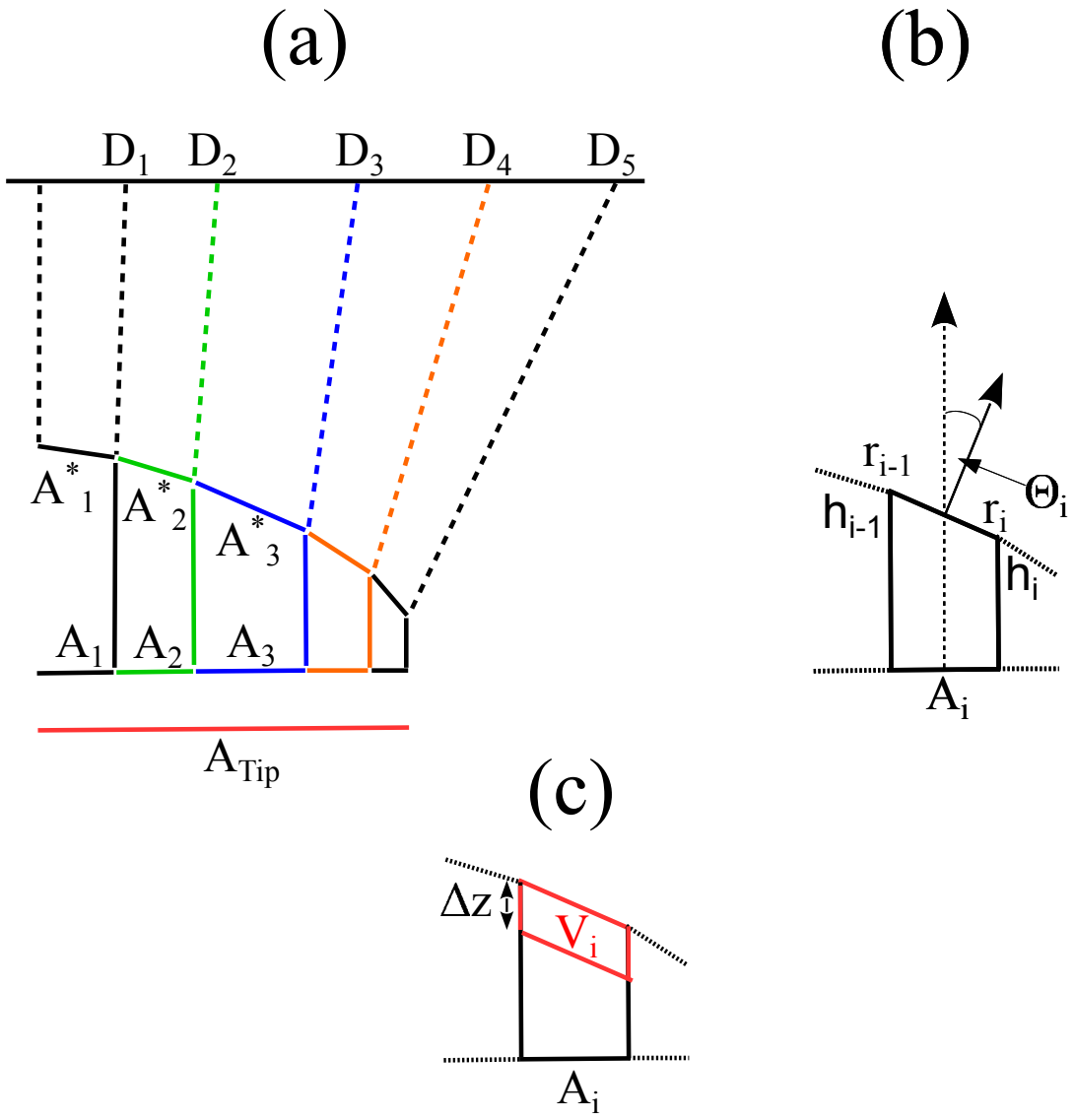

Figure 4.2.: Segmentation of emitter and detector. The detector (on the top in (a)) is divided into rings of radii D_i. The same is done with the profile intended to describe the tip surface in a particular steady-state situation (see bottom of (a)). Every detector ring is associated with an interval of detection distances ΔD and a projected surface area A_i. The inclination angles θ_i of the corresponding profile rings are fixed, as it is illustrated in (b). The rings have a well-defined radius r_i and a height h_i. Every ring represents an emission angle interval $\Delta\theta$, which is defined by the neighbor segments. In (c), the size of the evaporated volume V_i of one particular segment, given by $V_i = \Delta z \cdot A_i$, is sketched.

before, is reconstructed. The final reconstruction coordinates can be determined by linear interpolation between the coordinates of the previously determined profile nodes. Since the distance D on the detector is known for each recorded event, the associated angle θ on the surface is defined by equation (4.1) and therefore it is clear, on which ring of the emitter profile (with the inclination angle θ_i) the next atom has to positioned. Due to the

assumed rotational symmetry of the investigated structure, the azimuth ϕ on the detector is equal to the azimuth φ on the surface. Consequently, the Cartesian coordinates $\vec{r}$ of an atom are calculated by

$$r_x = \left(r_i + \frac{\theta - \theta_i}{\Delta\theta} \cdot (r_{i+1} - r_i) \right) \cdot \cos(\varphi), \tag{4.5}$$

$$r_y = \left(r_i + \frac{\theta - \theta_i}{\Delta\theta} \cdot (r_{i+1} - r_i) \right) \cdot \sin(\varphi), \tag{4.6}$$

$$r_z = \left(h_i + \frac{\theta - \theta_i}{\Delta\theta} \cdot (h_{i+1} - h_i) \right). \tag{4.7}$$

After the reconstruction of an atom, the tip profile has to be lifted upwards to take into account the emitter shrinkage, which has taken place during the evaporation process. In a first approach, one could lift the entire tip surface according to the volume increase Ω given by the new atom:

$$\Delta z = \frac{\Omega}{A_{Tip}}. \tag{4.8}$$

This practice follows the conventional reconstruction techniques (except that the emitter surface is not a hemisphere any more and it is shifted downwards due to the inverted reconstruction order).

4.1.2. Fragmentation of the data set

The profile calculation described in section 4.1.1 is performed several times for different portions of data during the reconstruction of the whole data set. To this end, the list of recorded ion impacts is subdivided into smaller portions. The idea of this subdivision is to model the changes of the shape of the emitter during the measurement as accurately as possible, but keep the portion of data large enough to avoid statistical fluctuations in the shape calculation.

In contrast to the geometric point projection method, the reconstruction starts with the last detected ions, which ensures that the tip structure is rebuilt from the bottom to the top and the surface shape is known at any moment of the reconstruction. The evaluation expects two sampling parameters. The first parameter N_P is important for the profile calculation, which has been described above. It represents the number of detected events in the data

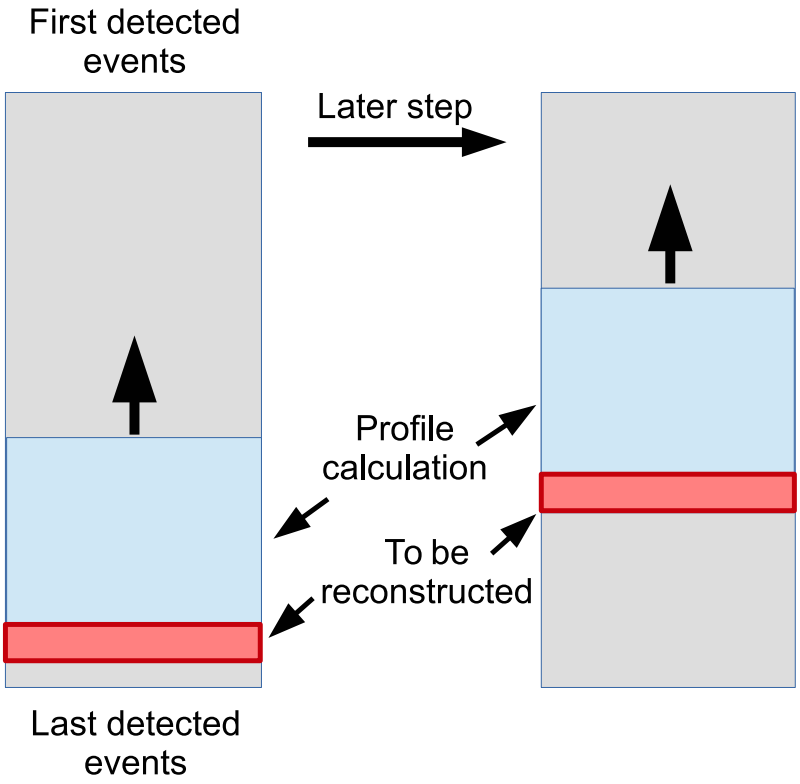

Figure 4.3.: Principle of the sampling process of the recorded measurement data (gray box) [12]. The reconstruction algorithm starts the profile calculation with the last detected ion at the bottom of the data set. All the ions in the blue box are taken into account for the derivation of the next tip profile. Atoms confined in the red box at the bottom of the data fraction are finally reconstructed on the basis of the resulting profile. Subsequently, the red and the blue box are shifted towards the earlier detected ions and the profile calculation is repeated.

portion that are considered for the identification of the next surface profile (indicated by the blue box in figure 4.3).

The second parameter N_R defines the number of atoms that will be finally reconstructed with the help of the currently calculated profile (red box in figure 4.3). This parameter is allowed to be equal to N_P, but in some cases it might be even beneficial for the reconstruction to choose a smaller value. Especially for smoothing the transition between different surface profiles, a choice of $N_R < N_P$ might lead to a more realistic result. In the case of very abrupt changes of the tip shape, a parameter choice with $N_P = N_R$ could lead to strong overlaps of the successive profiles. Obviously, a choice where $N_R > N_P$ doesn't make sense, because in this situation, a certain fraction of measured atoms is reconstructed based on a profile derived without considering them.

After the reconstruction of N_R atoms on the basis of the current profile, a new profile for the reconstruction of the next N_R atoms is calculated. To this end, the first N_R atoms in the data portion for the profile calculation are replaced by the next N_R atoms from an earlier

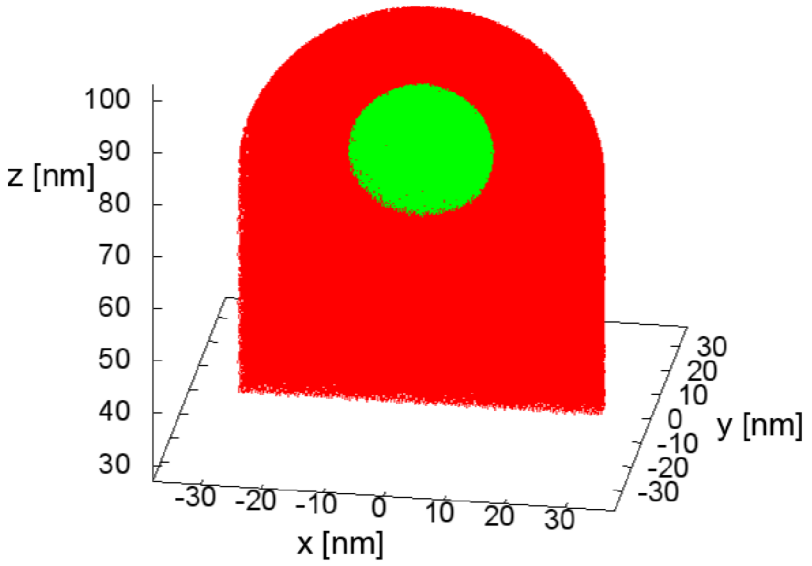

Figure 4.4.: Sample structure for testing the new reconstruction method [12]. The tip has an amorphous structure and contains a spherical particle (green) centered on the tip axis with a diameter of 24 nm.

stage of the field evaporation. Practically speaking, this means that the dashed red box and the blue box in figure 4.3 are shifted upwards towards earlier recorded events by the amount of data confined in the red box, as it is indicated on the right hand side of figure 4.3.

4.1.3. Proof of concept for symmetric emitter structures

In this section, the new reconstruction method presented in section 4.1.1 and 4.1.2 is tested [12]. To this end, the FEV of an amorphous tip structure containing a spherical particle (shown in figure 4.4) located on the tip axis has been carried out. The emitter has a radius of 30 nm and a height of 100 nm. The precipitate has a diameter of 24 nm and the atomic density is homogeneous and amounts to 6 atoms per cubic nanometer.

In order to demonstrate the capability of the new method clearly, the simulated FEV has been done with a severe difference in the evaporation field of the two species. The simulation package *TAPSim* is recording every field evaporated atom by default, which means it provides a detector with an efficiency of 100% and an angular range up to 90°. In order to make the situation more realistic, the reconstruction has been performed exclusively with those detected ions reaching the detector within a finite aperture below 45°. In the first attempt, the efficiency was kept at 100%. The original data set contained one million detected atoms. After the exclusion of all atoms outside the FOV, approximately 600.000 events were left for the test of the reconstruction method with the data set, containing a spherical particle with a higher or lower evaporation field. The data sampling parameters

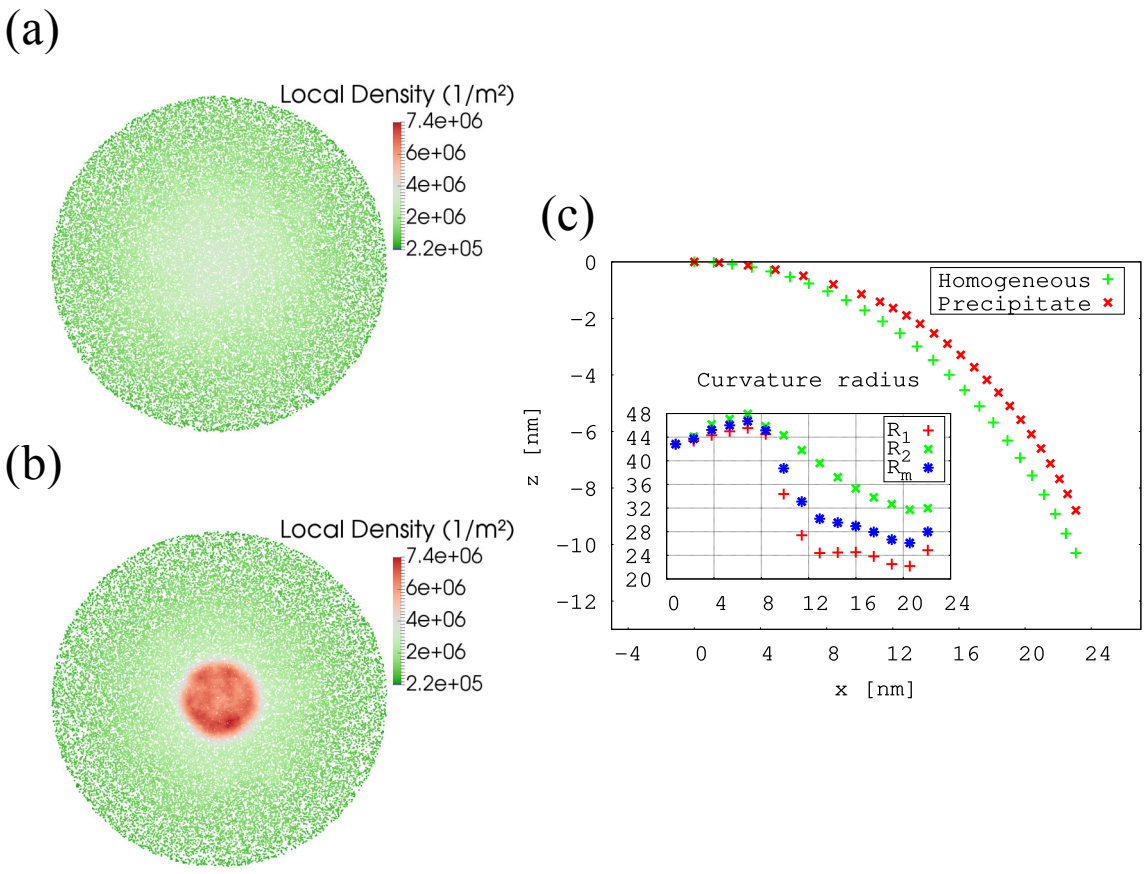

Figure 4.5.: Demonstration of the varying curvature radius shown for two calculated tip profiles [12]. In (c) the green profile is representing an emitter shape belonging to a homogeneous amorphous structure, while the red profile is resulting from a density distribution belonging to an inhomogeneous emitter structure, containing a species with a significantly lower evaporation field (28%). The density distribution on the detector corresponding to the green profile is shown in (a) and the distribution yielding the red profile is shown in (b). The inset in (c) illustrates the mean radius of curvature (blue) and the principle curvature radii R_1 and R_2 of the red surface profile at different lateral positions. A clear difference between the precipitate phase in the center and the outer matrix phase can be seen.

were set to $N_P = 50000$ for the profile calculation and $N_R = 10000$ for the portion of atoms that are reconstructed in each step. This choice is intended to smooth the transitions of the emitter profile shape, which occur during the reconstruction.

For the demonstration of the advantages of the new technique in comparison to any conventional method that assumes a constant emitter curvature, the capability of identifying the tip shape is shown for two different portions of data in figure 4.5. The two data portions belong to the simulated field evaporation of the emitter containing a particle with a 28% lower evaporation field. The picture in a) shows the density distribution for the first portion of data that has been detected, which means it contains the first 50000 atoms from the top of the emitter shown in 4.4. At this stage, no precipitate atoms were located at the surface,

and consequently, the surface shape has not changed yet from the ideal sphere. The density of events shows a small increase in the center, but overall, it looks rather homogeneous. By contrast, in figure 4.5 b), the density distribution on the detector clearly shows an increased amount of events in the center. The corresponding portion of data has been taken from a stage of the field evaporation, where the surface reached the precipitate. The increased density of events in the center is the consequence of the 28% lower evaporation field of the precipitate atoms compared to the matrix atoms. Since the precipitate is located in the center of the tip, the ions are predominantly detected in the middle of the detector.

According to equation (4.3), the enhanced amount of recorded material in the detector center in figure 4.5b) yields a larger radius of the associated ring segments in the calculated tip profile, as it can be seen in c). The red profile, stemming from the detection density in b), clearly has a very different shape, compared to the green profile resulting from the density distribution in a). A closer look on the mean radius of curvature along both tip profiles underlines the effect of the varying event density on the calculated tip shape. In the inset of figure 4.5c), the values of the principle curvature radii R_1 and R_2 belonging to the precipitate profile (red) is plotted over the lateral radius of every point in the profile. These principle curvature radii R_1 and R_2 finally yield the mean radius of curvature

$$R_m = \frac{2\,R_1\,R_2}{R_1 + R_2}. \tag{4.9}$$

The plot shows that the mean radius of curvature has two "plateau" values. The first plateau value for the inner part of the profile amounts to (44 ± 2) nm, while the second plateau at the outer part is (29 ± 2) nm. This means, the curvature radius for the inner part is significantly higher than the curvature radius of 30 nm of the initial tip, while it is slightly lower going further away from the tip axis. It also becomes clear that the two principle curvature radii strongly differ at the interface between the particle and the matrix but converge towards the initial mean radius of curvature (30 nm) again at the outer part of the profile, which may be interpreted as a confirmation of the presented new method.

In [85], the authors expect a relationship between the mean radii of curvature R_A and R_B and the evaporation field F_A and F_B of two phases, which reads $R_A/R_B = F_B/F_A$. In this presented example, the ratio of the plateau values of the curvature radius is (1.5 ± 0.1), while the ratio of the evaporation fields amounts to 1.4. Given the limited accuracy of the profile calculation, the stated relation in [85] can be considered as confirmed.

The remaining task of the reconstruction algorithm is the final calculation of the three-dimensional coordinates inside the tip volume for every detected ion. The coordinates are defined by equations (4.5), (4.6), and (4.7), always using the current profile associated with the data portion being reconstructed.

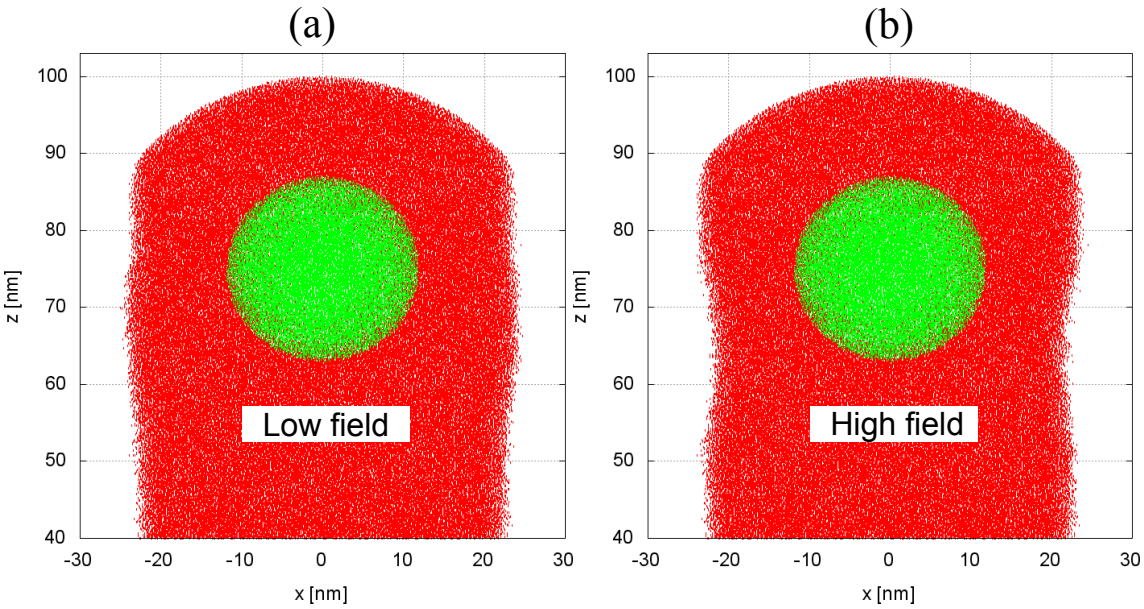

Figure 4.6.: The detected tip volumes for the case of a 44% lower evaporation field (a) and a 56% higher evaporation field [12].

In order to further test the algorithm, two simulated data sets with even more severe contrast in the evaporation fields were reconstructed. One simulation was carried out with a 56% higher and the other one with a 44% lower evaporation field of the precipitate atoms in comparison to the surrounding matrix. In figure 4.6 the original structures of the detected data sets for both example cases are shown. Here, another important effect of the local magnification occurring during FEV combined with the limited FOV can be seen. This effect is a variation of the outer diameter of the detected volume. In the low field case in figure 4.6a) an increasing diameter near to the precipitate can be observed. To the contrary, in the high field case in figure 4.6b), the volume tapers when the spherical particle is evaporated. Since the lift of the emitter profile after the reconstruction of an atom depends on the projected cross-sectional area A_i (see equation (4.8)), this variation regarding the cross-sectional area will affect the reconstruction. To this end, the diameter change also needs to be considered during reconstruction.

In this study, a rather simple approach has been implemented in order deal with this issue. Since the atom type of every detected ion and its respective evaporation field is known prior to the reconstruction, the average evaporation field $E_{evap,av}$ for the entire data set can be calculated:

$$E_{evap,av} = \frac{1}{N} \sum_{i=0}^{N} E_{evap,i}. \tag{4.10}$$

Furthermore, for each portion of data considered for the calculation of the next surface profile with the help of equations (4.3) and (4.4), the average evaporation field of the respective portion $E_{evap,i}$ is determined according to equation (4.10). Once this average evaporation field for the current data portion is known, a scaling factor ε_i for the diameter of the newly determined surface profile is derived:

$$\varepsilon_i = \frac{E_{evap,av}}{E_{evap,i}}. \tag{4.11}$$

This scaling factor leads to an increased diameter of the reconstructed tip volume in the case of a precipitate with a lower evaporation threshold, since the average evaporation field of the data portion is significantly lower than $E_{evap,av}$, if the portion of data contains a lot of precipitate atoms. In the opposite case, the volume diameter is shrinking as soon as a relatively large amount of precipitate atoms with a high evaporation field is reconstructed. This simple approach to deal with a varying diameter has been applied in all the following test scenarios.

The full reconstruction process has been tested for tip structures with the low evaporation field and the high evaporation field precipitate shown in figure 4.6. The results are shown in figures 4.7 and 4.8. The reconstruction has been performed with the same values regarding the sampling parameters. In the low field case, as well as in the high field case, the values $N_P = 5000$ and $N_R = 5000$ turned out to yield the most reasonable result. The aspect ratio of the reconstructed particle with the lower evaporation field in figure 4.7a) is equal to 1.0 and the whole emitter volume is obviously more similar to the original tip than the tip volume shown in b). This is already a tremendous improvement, which becomes clear by comparing it with the aspect ratio of the reconstructed particle in figure 4.7b). Here the conventional reconstruction delivers a particle with an aspect ratio of 1.92. Despite this impressive benchmark, the overall shape of the particle in the middle of the tip is still slightly too flat at the upper end.

For the tip structure containing a particle with a 56% higher evaporation field, again the new technique yields a significantly improved result (figure 4.8a)) compared to the Bas et al. approach in figure 4.8b). The aspect ratio of the particle resulting from the new technique amounts to 0.98, while it is equal to 0.63 for the back projection technique. It becomes very clear that the new approach is able to significantly reduce the local magnification effect, which causes the drastic deformation of the precipitate in the classical reconstruction.

However, also with the new concept, the shape of the reconstructed particle is still not perfectly spherical. Opposite to the low field case, here the reconstructed precipitate appears too flat at the bottom and slightly too pointed at the top. The reason for the observed remaining deviations from a spherical shape in both cases is mainly given by the strong and

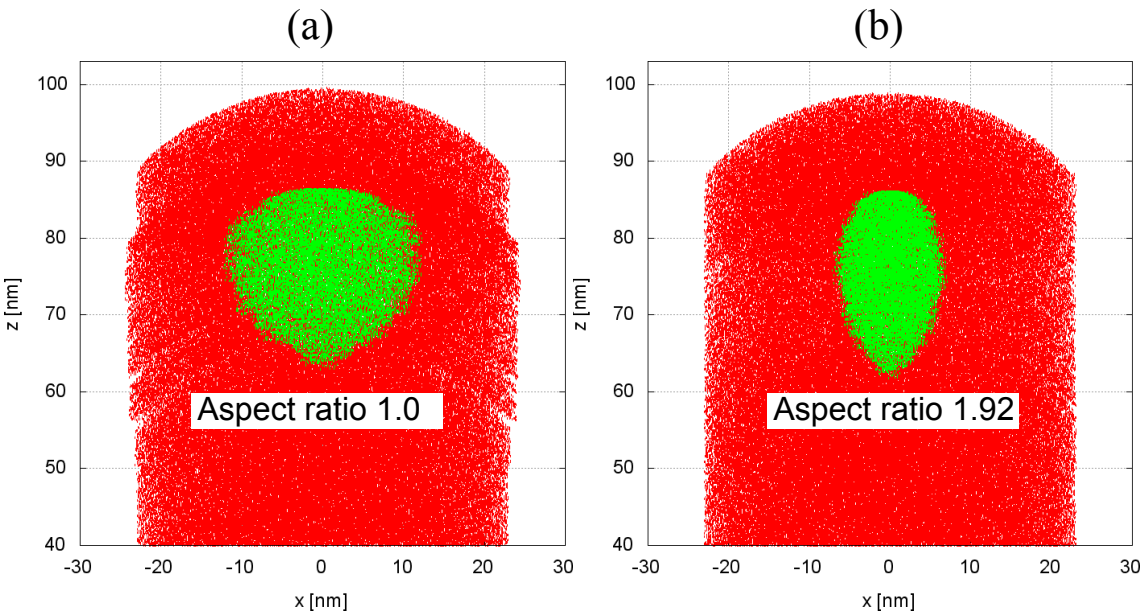

Figure 4.7.: Slice through the reconstructed emitter volume with a precipitate of lower evaporation field. New concept (a) and the reconstruction resulting from the conventional back projection approach by Bas et al. (b). (reproduced from [12])

abrupt changes between two subsequent emitter profiles. Further improvement might be achieved by varying the sampling parameters N_R and N_P during the reconstruction, rather than keeping them at the same constant values throughout the whole process. Potentially, a reasonable reduction of the value for N_P at a transition stage of the emitter profile might turn out to be beneficial. On the other hand, this would require at least another parameter, the user would have to specify, and therefore the concept would also become more complicated.

In order to point out the advantages of the presented new method further, in figures 4.9 and 4.10, the atomic density in the vicinity of each atom inside the reconstructed emitter volume is shown for both reconstruction methods. For the particle with a low evaporation field, it can be seen in figures 4.9b) and c) that the conventional reconstruction delivers a volume with an enormously increased density of the atoms, which is a direct consequence of the local demagnification effect in this case. However, the atomic density observed for the new approach is overall far more homogeneous, especially inside the precipitate. Nevertheless, one can still see local fluctuations of the atomic density, mainly at the interface between the precipitate and the matrix. In some areas of the reconstruction in figure 4.9b), also the abrupt transition between one calculated profile and the next one is clearly visible.

For the particle with the higher evaporation field, the influence of the large contrast in the evaporation fields is very prominent in figure 4.10c). The density of the reconstructed particle is dramatically reduced compared to the surrounding matrix. Again, in figure 4.9b)

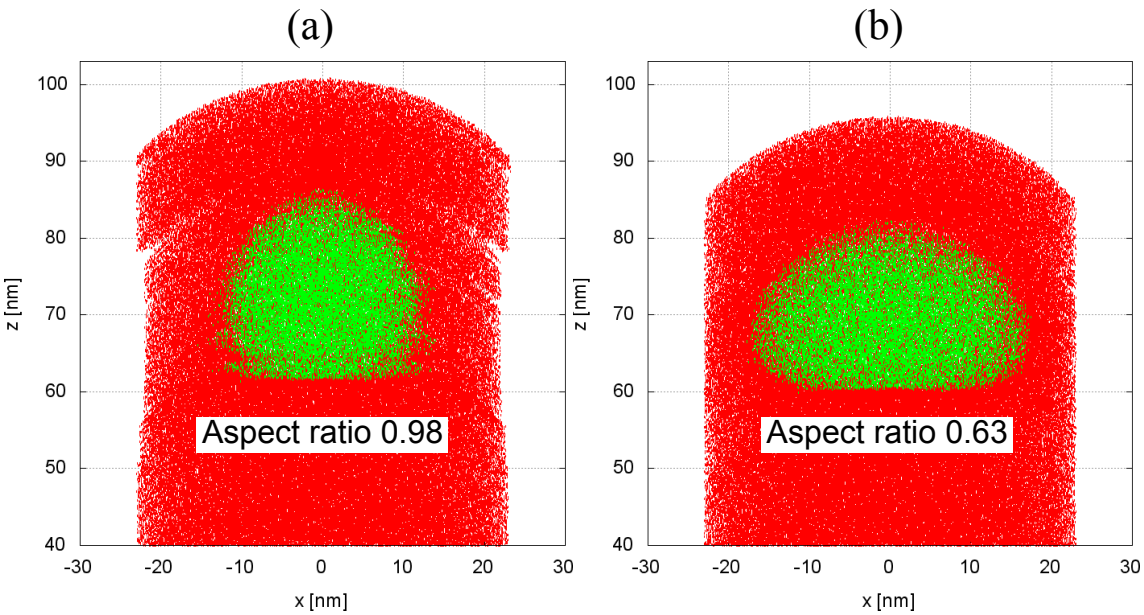

Figure 4.8.: Slice through the resulting reconstruction derived by the new approach for a precipitate with a higher evaporation field (a). In (b), the reconstruction performed by the Bas et al. method is shown. (reproduced from [12])

derived with the new reconstruction concept, the influence of the local magnification is significantly weaker. The atomic density appears to be almost homogeneous even in the precipitate region.

Despite this very satisfying situation, also for a precipitate with a high evaporation field, the density still varies significantly at the particle/matrix interface and also in this case, the transitions between the individual profiles, describing the emitter at different stages is not always smooth. Especially at the top of the reconstructed precipitate in b), the outer part of the volume seems to be depleted, which can be explained by a very abrupt change of the detector density distribution and their respective profiles at this stage of the reconstruction.

At this point it is worth to mention that these findings are not completely surprising, since the here presented tip shape calculation assumes a steady-state situation when calculating an emitter profile, as it has already been pointed out in section 4.1.1. Unfortunately, this steady state is not fulfilled when the precipitate appears or disappears at the tip surface during FEV. In these situations, the field emitter changes its shape relatively quick and therefore, the resulting tip profile extracted from the event distribution on the detector cannot describe the whole transition sufficiently accurate.

In the next subsection 4.1.4, the reason for the observed density variations is explained and in addition, an amended procedure regarding the lift of the current emitter profile after the reconstruction of an individual atom is discussed. The main idea of this further improved procedure, is to lift the rings describing the surface individually, rather than

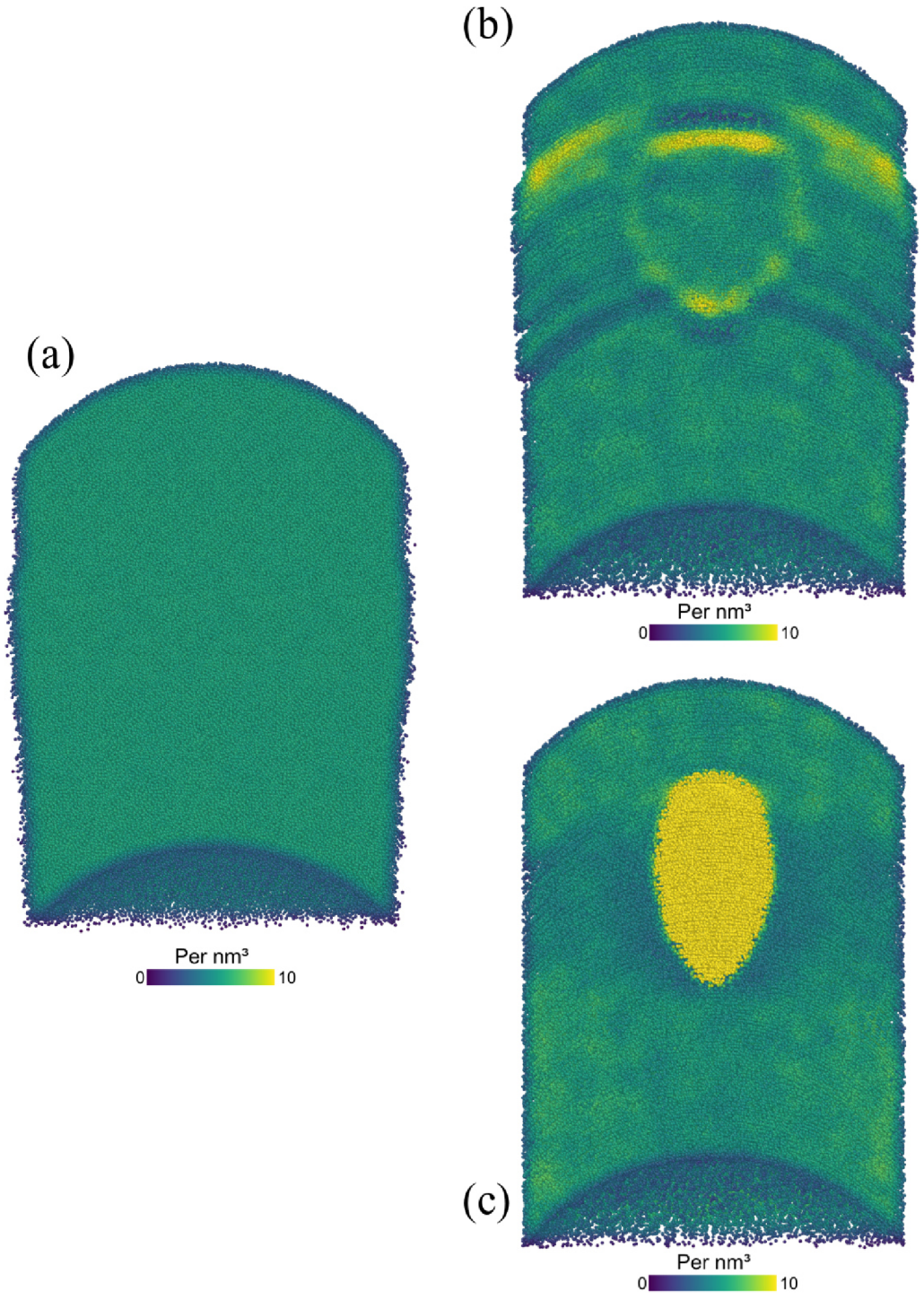

Figure 4.9.: Atomic densities for the case of a particle with a low evaporation field (reproduced from [12]). In (a), a slice through the original tip structure with a homogeneous density of 6 atoms per cubic nanometer is shown. In (b), the density of the reconstruction by the new method is plotted, while (c) shows the atomic density achieved with the conventional point projection method.

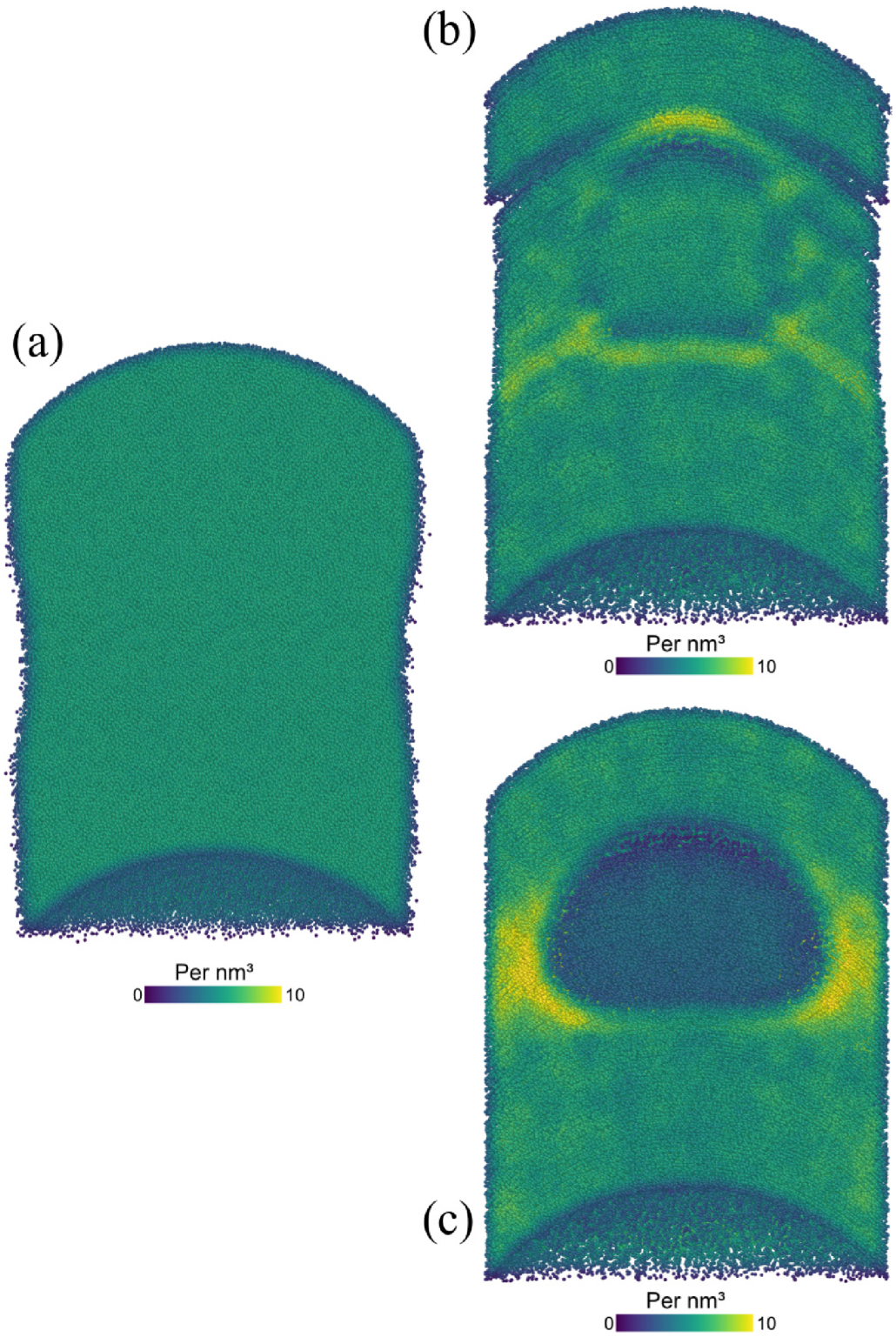

Figure 4.10.: Atomic densities for the case of a particle with a high evaporation field (reproduced from [12]). In (a), a slice through the original tip structure with a homogeneous density of 6 atoms per cubic nanometer is shown. In (b), the density of the reconstruction by the new method is plotted, while (c) shows the atomic density achieved with the conventional point projection method.

lifting the entire emitter surface rigidly after each reconstructed atom.

4.1.4. Lifting the emitter profile

As it can be seen in figures 4.9 and 4.10, the atomic density of the reconstructed volume still shows local density variations even in the shape corrected reconstruction scheme. These variations mainly originate from the fact that the tip profile has been lifted rigidly according to equation (4.8) after positioning each individual atom. The large difference in the evaporation field of the involved species causes a very inhomogeneous evaporation rate per surface area during a transition period of the FEV. The term transition period denotes a situation of the field evaporation, in which the emitter shape is not in a steady state, which is assumed in the above presented approach.

A "rigid lift" of the emitter profile during the reconstruction of those portions in the data set, automatically yields either depleted or compacted areas. Instead of lifting up the full profile according to (4.8), one may expect that a local lift of the surface would avoid or at least reduce these density variations.

Therefore, it was tried to further improve the reconstruction by lifting every single ring segment of the emitter profile individually. Since all segments are connected to their neighbors in the profile, the lift of one of these segments would indirectly influence the neighboring segments as well. In particular, the orientation angle θ_i with respect to the detector axis, which is supposed to be fixed, would inevitably change during the shift of a neighboring piece of the surface profile.

In order to deal with this problem, it is assumed that the profile pieces are no longer connected to each other, so that their fixed orientation angle can be maintained during the reconstruction. By lifting the segments individually, the calculated tip surface is granted a necessary amount of "freedom", which allows the continuous adaption of the profile to a significant change of the measured event density on the detector.

The principle of the "local lift" of the emitter profile is rather simple. If a detected ion needs to be positioned somewhere within the surface segment i, the shift in direction of the tip axis is given by

$$\Delta z_i = \frac{\Omega}{A_i}, \tag{4.12}$$

where A_i represents the projected cross-sectional area of the involved segment.

As it has been described in section 4.1.2, the surface profile is calculated several times during the reconstruction for different detector patterns. In order to avoid depleted or compacted regions in the reconstructed volume, the transition between two different

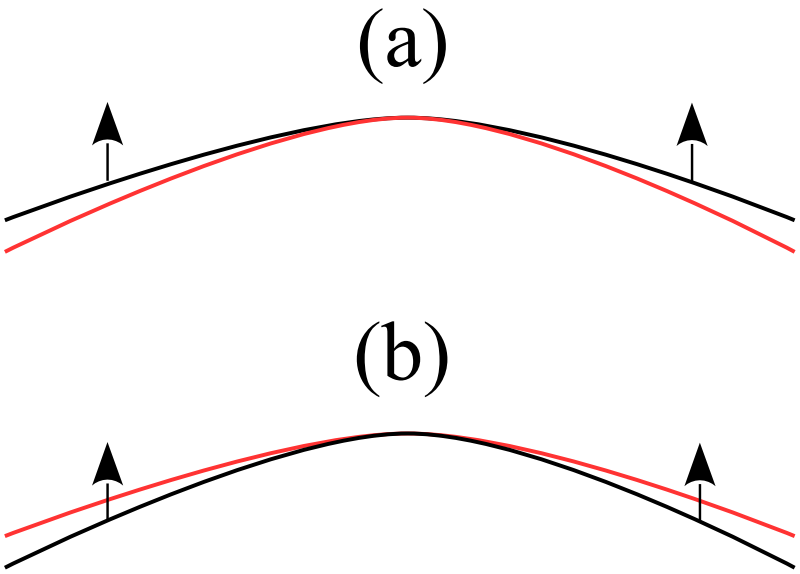

Figure 4.11.: Issue of strongly varying surface profiles. In (a), the case of consecutive surface profiles with a depleted zone between them is shown. The old profile (red) is followed by the black profile, which is not as strongly bent as the previous profile. Consequently, the space between the profiles is left empty, as the new profile is further shifted upwards. In (b), the opposite case, where the old profile (red) has a smaller curvature than the new profile, is illustrated. Since the new profile (black) is shifted upwards, the space between the profiles will be filled with reconstructed atoms twice, yielding a larger density of atoms in this area.

calculated emitter profiles is most important. If the density distribution on the detector changes significantly from one considered portion of data to another, the shape of the identified profile will also undergo a severe change.

Therefore, applying the rigid lift principle and stacking these emitter profiles upon each other, is very likely to yield either depleted areas which are simply not filled (see figure 4.11a)), or to the contrary, some areas might be considered twice, causing an increased density of atoms in those particular regions (see figure 4.11b)). Consequently, in the local lift procedure, a newly derived profile is stacked directly onto the previous profile, avoiding voids or overlaps.

The corresponding procedure is illustrated in figure 4.12. Since the involved surface profiles have already been split into pieces/segments, for each segment belonging to the new profile, a reasonable height needs to be found. The original profile below the next one (see figure 4.12a)) is no longer perfectly smooth, due to the fact that each segment has been lifted upwards individually during the reconstruction of the previous portion of detected ions (as illustrated in figure 4.12b)). The next surface profile, calculated by considering the next portion of data and using equations (4.3) and (4.4), differs from the previous profile regarding the lateral positions of the nodes, as it is shown in figure 4.12c). Consequently, the segments, belonging to this new profile cannot simply be positioned directly on top of

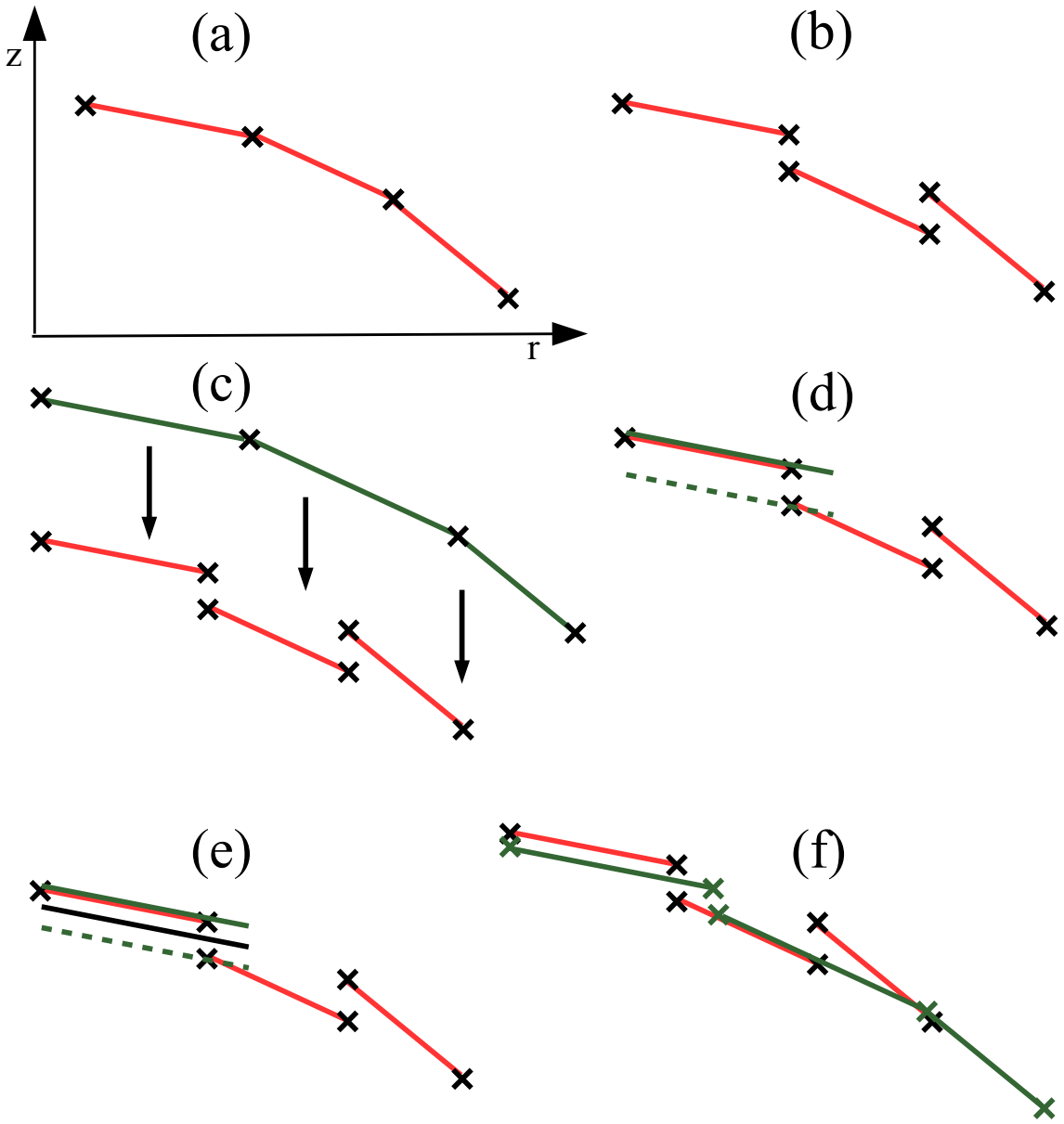

Figure 4.12.: Illustration of the procedure to put one calculated emitter profile onto the previous profile. In (a), an initial surface profile is shown. All segments, belonging to this profile are still connected. Due to the local lift of each segment, the segments are disconnected after some reconstructed events (b). On top of this profile the next one (green color) calculated with a new portion of data, which might slightly differ regarding its lateral size has to be put (c). Therefore, the next profile is again split into its individual segments. Every new segment is then brought into close contact to the profile below (d). This means that two possible heights are considered for every new segment. The first height is found by putting the left node of the new profile segment directly onto the previous profile (green solid line). Alternatively, the second height is defined by the height, which ensures the right node to be placed directly onto the underlying profile (dashed green line). The resulting position is given by the average of both possible heights(black solid line in (e)). The application of this procedure to every new segment finally yields the new profile described by the solid green lines in (f).

the profile segments underneath, belonging to the old profile. Therefore, for every new profile segment a reasonable height is derived in a two step process.

First, the new segment (solid green line in figure 4.12d)) is shifted vertically so that the inner node (the left node in figure 4.12d) respectively) is lying directly on the surface below, described by the previous profile (red). The resulting position is indicated by the solid green line in figure 4.12d). In a second step, the same procedure is applied, so that the outer node of the current segment (the right node respectively), is also positioned directly on the profile below, yielding a position, described by the dashed green line in figure 4.12d). The final height for the profile segment is then simply given by the average of both heights, which have been found in the two steps before. The resulting position of the profile piece is given by the black line in figure 4.12e). Once this scheme has been applied to all the segments of the new profile, the positioning of the individual atoms can continue.

It is worth to mention that the resulting new profile is also not perfectly smooth, as it can be seen by the solid green line in figure 4.12f). Furthermore, the issue described in figure 4.11 is still not avoided completely, but it can be reduced sufficiently, if the number of segments in the profiles is chosen reasonably. In addition, the calculation of new profiles during the entire reconstruction process using equations (4.3) and (4.4) remains very important for the local lift concept. Since the lateral size of the new profile segments needs to be adjusted to the amount of detected material in the corresponding detector segments, the recalculation of the profile has a direct and important influence on the local lift concept because the lateral size of the segments defines the z-shift of each segment according to equation (4.12).

In the following, the beneficial influence of the local lift procedure, including the concept of stacking profiles upon each other (as described above), on the atomic density of the reconstructed emitter volume is discussed. To this end, the result of the reconstruction approach using the rigid lift concept is compared to the result of the local lift principle. In figure 4.13a), the atomic density of the resulting reconstructed volume for the emitter structure containing a particle with a low evaporation field is shown for the rigid lift concept. It can be seen that the density is rather inhomogeneous at certain transition positions. Especially in the area highlighted by the orange dashed ellipse, the density is increased. The reason for this increase can be understood with the help of the different emitter profiles, which have been calculated during the reconstruction (black solid lines). In the considered region of the volume, the successive profiles differ strongly. As a consequence, the mechanism of overlapping profiles, described in figure 4.11b), yields an increased atomic density.

In figure 4.13b), the determined profiles for the rigid lift concept are plotted (black solid lines) together with the profiles of the local lift concept (red solid lines). The local lift

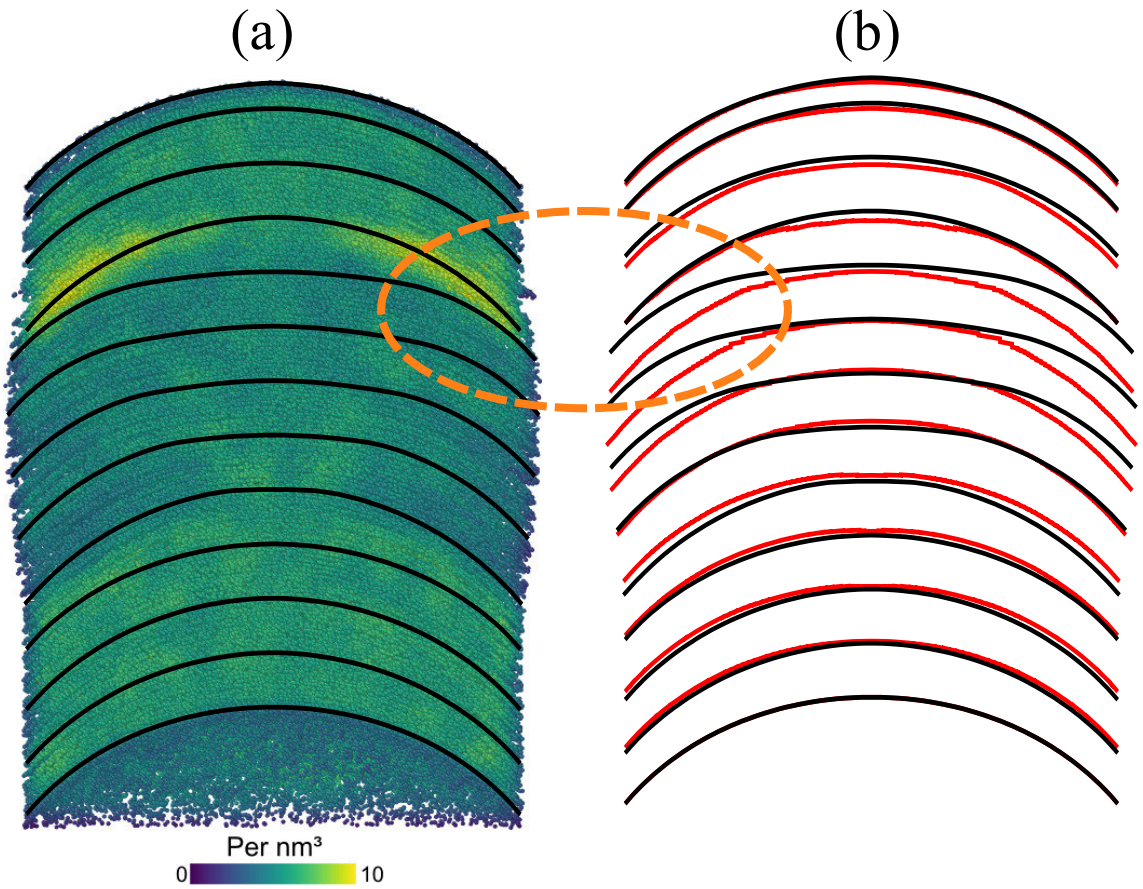

Figure 4.13.: Effect of lifting profile pieces individually. In (a), the development of the field emitter surface during reconstruction is shown for the rigid lift concept. The black lines represent the individual surface profiles, which have been calculated during the reconstruction process. In the background, the atomic density of the resulting emitter volume is shown. In (b), the profiles belonging to the rigid lift concept are compared to the profiles related to the local lift concept (red lines).

profiles have been derived by the process described in figure 4.12. It can be seen, that in the beginning (the bottom) the profiles are practically the same, since here the evaporation process has been in a steady state. As soon as the precipitate atoms are contained in the data portions considered for the profile calculation, the black and red profiles start to differ. Especially in the region, highlighted by the orange dashed ellipse, the red profiles stay behind the black profiles in the outer part of the volume. In this part of the reconstruction, a lot of material is positioned in the center, which means that the segments in the center of the profile are lifted more often. At the transition, where no more precipitate atoms are contained in the data portions (highlighted region) the difference between the rigid lift and the local lift is reduced again, until it almost vanishes at the very top. Due to the fact that the outer part of the profiles stays behind in the local lift concept, the increased atomic density in this region, as it can be seen in figure 4.13a), can be avoided (see figure 4.14).

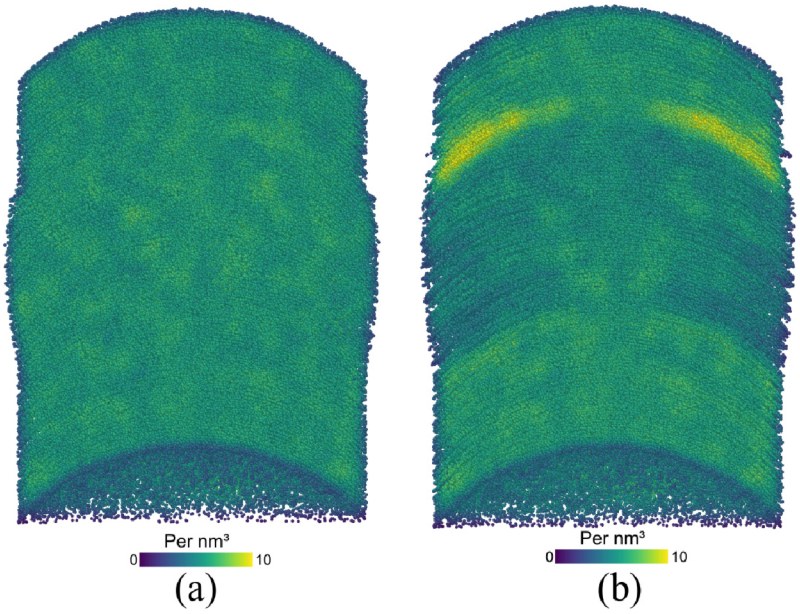

Figure 4.14.: Slice through the improved reconstructed emitter volume for the structure containing a particle with a lower evaporation field (a). Obviously, the density of atoms is clearly more homogeneous compared to the reconstruction shown in (b), which resulted from a rigid lift of the surface profiles after every reconstructed atom.

The influence of the reconstruction protocol by the local lift concept on the evaporated tip volume from figure 4.4 is shown in figures 4.14 and 4.15 for the case of a low evaporation field and a high evaporation field precipitate. The reconstructed volumes in figures 4.14a) and 4.15a) clearly show a significant improvement regarding the atomic density. The reconstructed tip structures show an impressively homogeneous atomic density for the lower as well as the higher evaporation field cases. The presence of a particle with a significantly different evaporation field is practically not reflected in the density anymore. By contrast, the reconstructed volumes based on the shift of "rigid" tip surfaces in figures 4.14b) and 4.15b) treat the transition periods of the field evaporation insufficiently and thus yield significant density variations, especially in the vicinity of the particle. The aspect ratios of the particles in the volumes belonging to the local lift concept did not change significantly in comparison to the rigid lift results.

As a result, the individual lift of the profile pieces together with the concept from figure 4.12 is a fairly uncomplicated approach to account for transition periods in the measured data, which could not be considered otherwise. At the same time, it has to be considered as a compromise between an approach with a sequence of fixed surface profiles as described in section 4.1.1 and a completely free approach, where the individual pieces of each profile would be allowed to change its height and orientation angle.

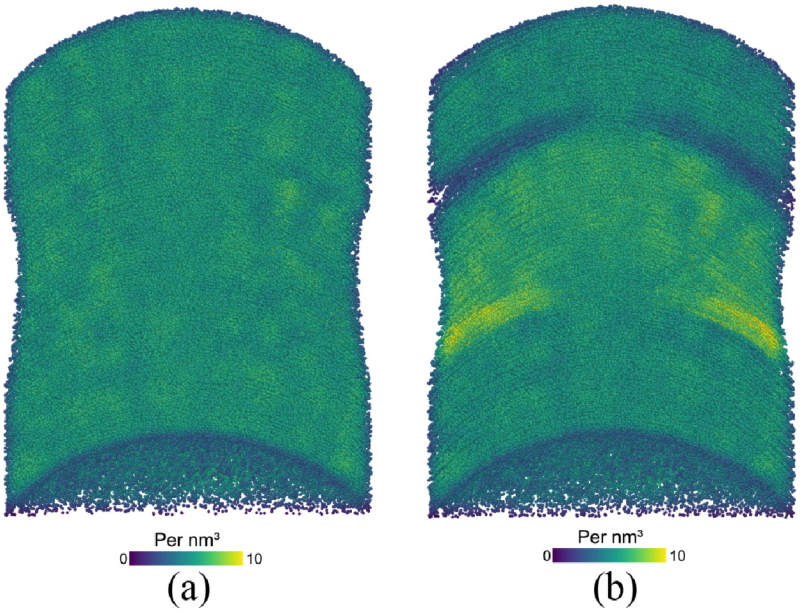

Figure 4.15.: Slice through the improved reconstructed emitter volume for the structure containing a particle with a higher evaporation field (a). Obviously, the density of atoms is clearly more homogeneous compared to the reconstruction shown in (b), which resulted from a rigid lift of the surface profiles after every reconstructed atom.

4.1.5. Reconstruction of layer structures

The presented final reconstruction scheme shall be further investigated for typical example structures with rotational symmetry. Beside emitter volumes containing spherical precipitates, layer structures are highly interesting. It is known from simulation studies [86–89] and APT experiments [90–93] that the reconstruction of layers is rather complex. Especially in cases, where the materials in the different layers have strongly deviant evaporation fields, the point projection algorithm yields very inhomogeneous layer thicknesses and also depleted areas at the interfaces. Rolland et al. recently proposed an approach dealing with this issue, which is exclusively restricted for the reconstruction of layer structures [94]. This technique also works without the assumption of a spherical tip shape and is based on an analytical model for the emitter endform. Another suggested way to deal with the reconstruction of layers is the application of an image compression function instead of a constant image compression factor [95]. In this case, the image compression factor varies for different detection angles and stages of the measurement. Similarly, several other authors suggest to use dynamic reconstruction parameters instead of constant values [96]. Nevertheless, these latter approaches all still rely on a spherical emitter shape.

Since the here presented approach is not exclusively dedicated to deal with layer structures, a successful test for a few example cases would underline the increased versatility of the

here proposed technique. If the layers are not very thick, the FEV of an individual layer can be characterized by a permanent change of the emitter shape. In other words, a steady-state situation of the evaporation process, as it is assumed for the here presented technique, is not present as long as the layer is located at the tip surface. The only way to deal with a situation of this kind, is the compromise, which is described in section 4.1.4, where the originally fixed surface profiles are split up into pieces, allowing to lift those pieces individually.

Like in section 4.1.3, the emitter volumes that were tested here, had an amorphous structure (tip radius 30 nm) and contained an embedded 10 nm thick layer perpendicular to the tip axis. The FEV has been simulated with the *TAPSim* package for two different cases. As with the precipitates, in the first case the layer atoms had a 44% lower evaporation field (low field case) and in the second case a 56% higher evaporation field (high field case). The detected volumes for a fixed FOV are shown in figures 4.16a) and 4.17a). A well-known issue of the reconstruction of layers with different evaporation fields using the point projection approach is the strongly varying layer thickness in the final reconstruction. As already discussed before, the reason for this common observation is mainly given by local magnification effects caused by the severely changing tip shape during the evaporation process. These artifacts are also clearly visible in the low field, as well as the high field case shown in figures 4.16b) and 4.17b).

In the low field case, the outer part of the layer (green species) is significantly thinner than the central part. The opposite observation can be made for the high field case. In the low field case, the tip surface flattens as soon as the upper matrix layer is completely removed. As a consequence, the majority of the layer material is detected in the center of the detector. Consequently, due to the fixed spherical surface shape assumed in the reconstruction, the center of the layer has a higher thickness because most layer atoms are considered to originate from the center of the emitter. The outer part appears to be thinner and even shows depleted regions because the rigid emitter surface is moved downwards after each reconstructed atom.

In comparison to the point projection technique by Bas et al., the here presented approach delivers a more constant layer thickness in both cases, illustrated in figures 4.16c) and 4.17c). The sampling parameter N_P and N_R were chosen differently for the two numerical experiments. In the low field case, the values $N_P = 80000$ and $N_R = 7000$ proved to be useful. In the high field case, the most successful reconstruction was found for $N_P = 35000$ and $N_R = 1000$.

In the example with the 44% lower evaporation field, the layer thickness amounts to approximately 10 nm and only a slight fluctuation of the thickness from the center towards the outer part of the volume is visible. The overall position of the layer along the tip

axis is a little too high ($\approx 2\,\mathrm{nm}$), which stems from the fact that due to the limited FOV, the information about the lateral size of the detected tip volume is lost and needs to be estimated. Comparing figure 4.16c) with the original volume in a), one can see a very slight difference in the lateral size. It appears that the volume in c) is $1-2\,\mathrm{nm}$ more narrow in the lower part underneath the layer (between 32 and 70 nm). Therefore, the position of the layer along the tip axis is slightly too high. The total height of the entire reconstructed volume is matching very well to the height of the initial volume in a). The reason for the accurate height is obviously the strong broadening, which occurs just underneath the layer (at approximately 75 nm). This broadening balances the effect of the narrow volume below and finally yields the correct height of the reconstructed tip. It is worth to mention that in the outer region of the reconstruction, there are still some density fluctuations visible, which will be discussed later (see figure 4.18).

In addition to the z-shift of the layer, the changing lateral width of the measured volume in the layer zone itself could not be reconstructed entirely correct. As it can be seen in figure 4.16a), the width at the bottom of the layer is longer than elsewhere in the detected volume, and it is decreasing fast towards the top. This necking effect, caused by the curvature change during evaporation, is in principle also modeled, but, since according to equation (4.11), the reconstruction algorithm assumes an increased width, as long as atoms with a significantly lower evaporation field are involved in the calculation, the necking effect is not sufficient. For a more accurate consideration of the width variation, a more complex model would still be needed. In the future, the problem might be solved by a larger field-of-view of the detector systems.

The application of the new reconstruction technique to the high field case also yields a layer structure with a very constant thickness from the center to the outer edge of the volume. Nevertheless, the thickness of the reconstructed layer appears slightly expanded to approximately 12.5 nm and like in the low field case, the height position of the layer is slightly shifted. In this case, the shift is directed downwards. Here it has to be mentioned that the final height of the complete reconstructed volume is somewhat too small, which is again explained by the inaccurate knowledge of the lateral size of the detected volume. The lateral width of the layer volume in the reconstruction correctly decreases from the bottom to the top of the layer. However, in the bottom the reconstructed necking is not large enough, while on the top of the layer is not broad enough compared to the original detected volume. The comparison of the atomic density between the point projection approach and the here presented full algorithm is illustrated in figure 4.18 and 4.19. In general, the density achieved by the newly developed approach is convincingly more homogeneous and is sufficiently close to the preset value of 6 atoms per cubic nanometer.

In the low field case, the conventional point projection technique clearly leads to an

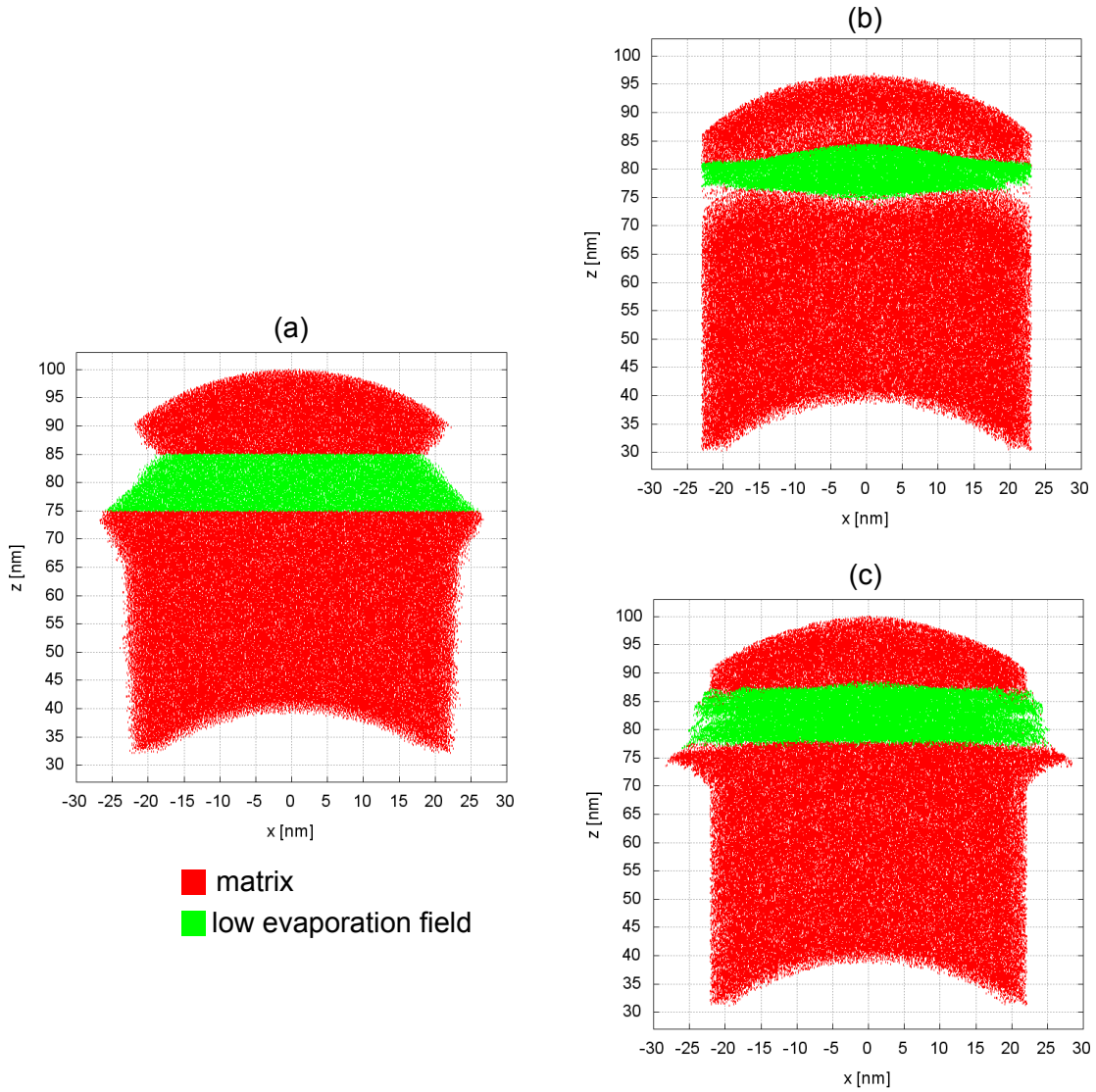

Figure 4.16.: Reconstruction of a layer structure with a lower evaporation field. The detected emitter volume in (a) has been reconstructed with the point projection approach by Bas et al. (b) and the new algorithm (c). The new algorithm has been performed by applying the local lift technique described in section 4.1.4 to achieve a seamless transition between different reconstruction stages.

increased density in the layer accompanied with a severely decreased density especially at the interface below the layer. In comparison, the reconstructed volume in figure 4.18a) is almost constant, even inside as well as around the layer. Only at the outer edge of the layer structure, small regions with a slightly decreased and increased atomic density can be observed. In contrast to the point projection technique, where the position and shape of the layer inside the tip volume can easily be seen from the density fluctuations, the reconstruction in a) does not allow to distinguish between layer and matrix in the density

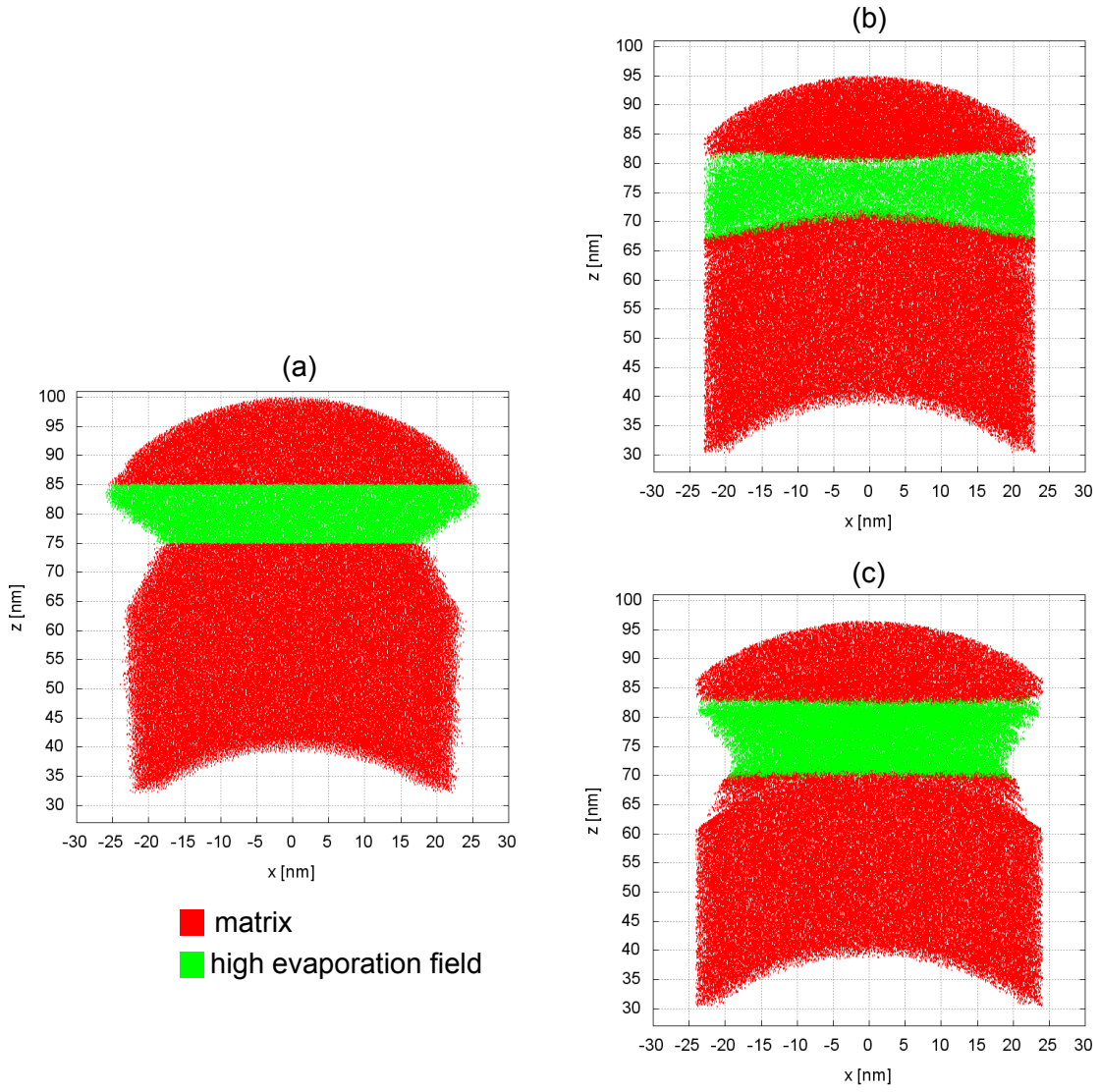

Figure 4.17.: Reconstruction of a layer structure with a higher evaporation field. Like in figure 4.16, the detected emitter volume is shown in (a). The point projection approach illustrated in (b) again shows a significantly varying layer thickness, which is clearly improved by the here presented algorithm, as demonstrated in (c).

map.

For the high field case in figure 4.19, again by using the Bas approach (figure 4.19b)), strong density variations cannot be avoided. The most prominent deviation from the correct target value can be seen above the layer and at the outer edge, where the density is increased. At the upper interface, the atomic density drops, which makes it possible to recognize the shape of the reconstructed layer even with the help of the density plot. In a), it can be seen that the new algorithm delivers an improved result. Nevertheless, it has to be admitted that even for the new technique, regions with an increased density at the outer edges of the layer

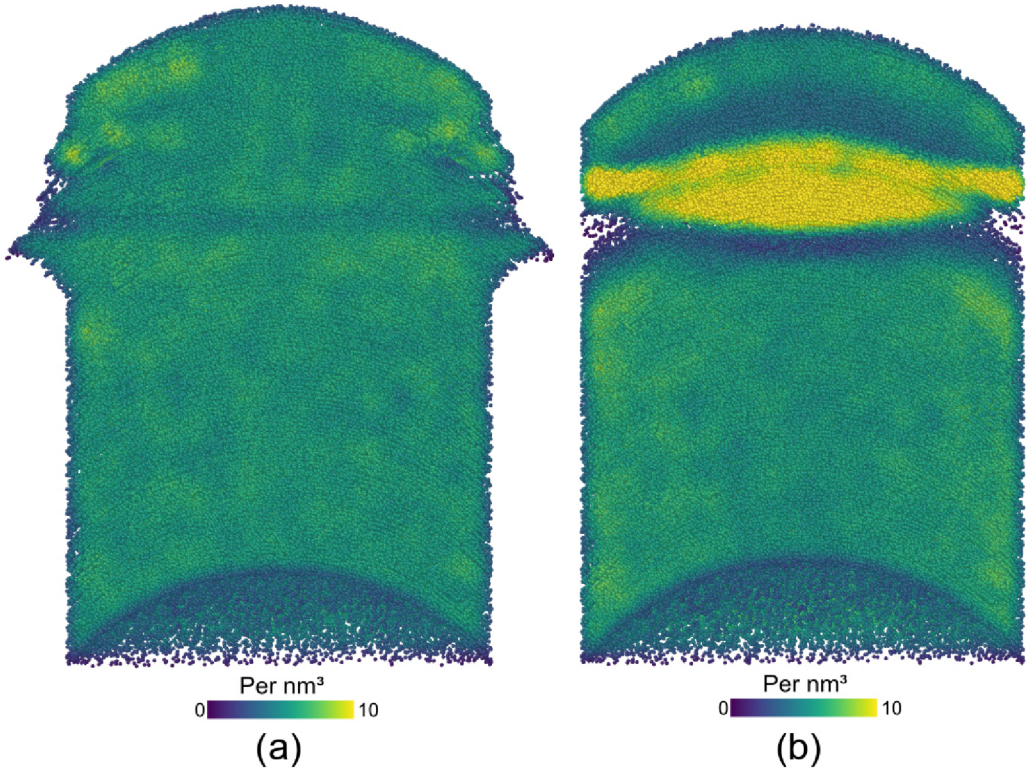

Figure 4.18.: Atomic density distribution in the reconstructed emitter volumes for the low evaporation field layer case. The plot in (a) demonstrates the homogenizing effect of the new approach on the reconstructed volume. The entire emitter shows a very constant atomic density close to the desired value of 6 atoms per cubic nanometer. In (b), the respective result achieved by the conventional point projection technique is shown.

bottom could not be avoided completely.

In general, it can already be stated that the here proposed algorithm indeed has the potential to be used routinely for the reconstruction of experimental data. The data set containing approximately 600000 atoms could be processed within a few seconds, which yields the conclusion that even for larger data sets, the presented technique would deliver a result within an absolutely acceptable time.

In the following, the influence of a more realistic detector efficiency is investigated, since this issue turned out to be important in section 3.1.

4.1.6. The influence of a limited detector efficiency

So far, the reconstructions shown in this section have all been carried out assuming a detector efficiency ρ_{Det} of 100%. In section 3.2 it was shown that a more realistic detector efficiency below 100% causes distortions and potentially destabilizes the reconstruction process. In the following, the performance of the above presented reconstruction technique

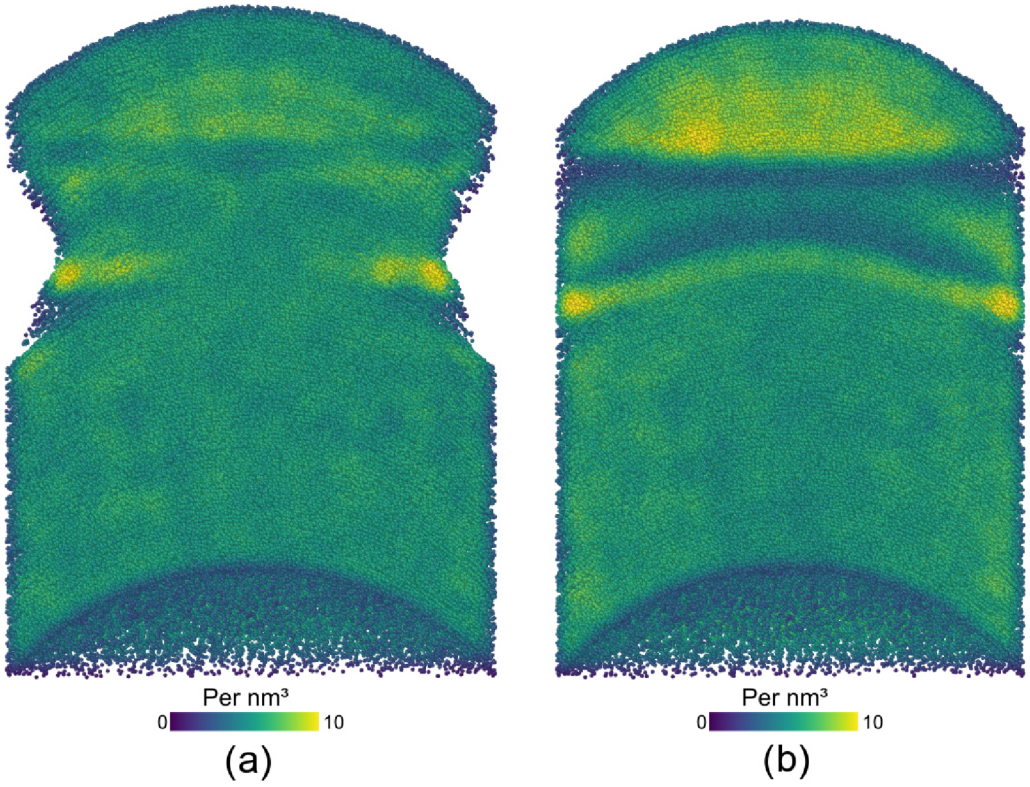

Figure 4.19.: Atomic density distribution in the reconstructed emitter volumes for the high evaporation field layer case. The atomic density of the reconstructed emitter volume could be improved by applying the new approach to the high field case in (a). For comparison, the resulting volume after the application of the Bas et al. approach is illustrated in (b).

under such more realistic conditions shall be demonstrated.

To this end, the detector efficiency ρ_{Det} is varied from 100% down to 50% in steps of 10%. The limited efficiency could be "simulated" after the simulated field evaporation by simply deleting a certain percentage of the measured detector events randomly. The reconstruction of the precipitate microstructure from figure 4.4 has been carried out again for all different values for ρ_{Det} and for both cases (the low field and the high field case). In order to deal with an imperfect efficiency ($\rho_{Det} \neq 100\%$), the missing volume needs to be accounted for in equation (4.12). Every time a segment of the surface profile is lifted, the potentially missing volume is considered:

$$\Delta z_i = \frac{\Omega}{\rho_{Det} \cdot A_i}. \tag{4.13}$$

In this way, the resulting total volume of the reconstructed emitter is the same for each efficiency value. Afterwards, the aspect ratio of the spherical particle inside the structure has been observed.

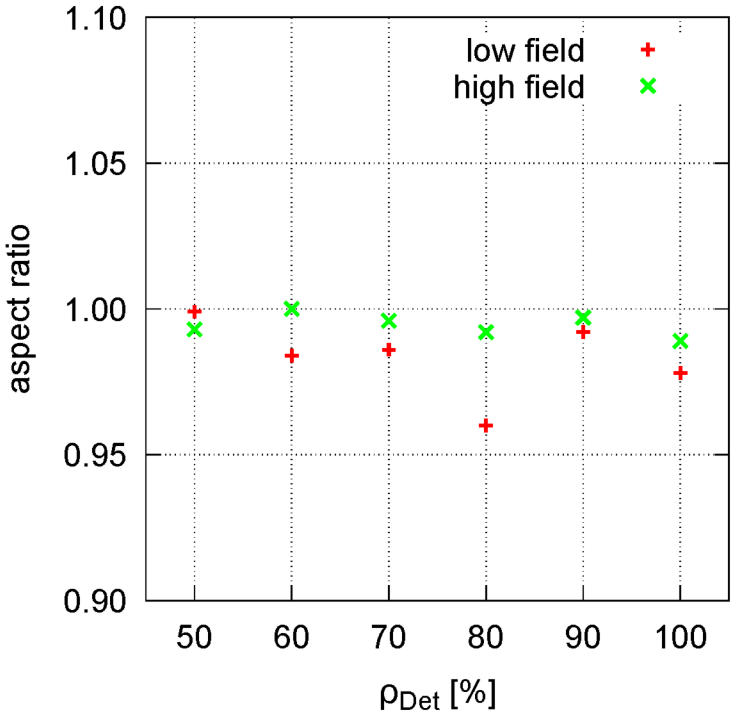

Figure 4.20.: The different values for the aspect ratio of the particle inside the reconstructed emitter volume are plotted against the assumed detector efficiency. The reconstruction has been done for the low field case (red) as well as for the high field case (green).

In figure 4.20, the obtained values for the particles aspect ratio are plotted over the corresponding detector efficiency. The main conclusion that can be drawn from figure 4.20 is that the aspect ratio of the particle embedded into the amorphous matrix is impressively stable and close to 1.0 for all tested cases. This finding becomes even more clear by comparing these values to the observed aspect ratio achieved with the help of the point projection approach (1.92 for the low field case and 0.63 for the high field case). Interestingly, for $\rho_{Det} = 80\%$, the value for the aspect ratio drops down to 0.96 in the low field case. The reason for this drop could be the coincidental deletion of slightly more detector events belonging to the precipitate compared to the other cases with different values for ρ_{Det}. In other words, the most likely explanation might be a statistical variation during the process of deletion of measured events. Nevertheless, a value of 0.96 is still impressively close to the value for a perfect sphere. In the appendix, the corresponding reconstructed tip volumes are shown (see figures B.1 and B.2).

Another important characteristic of this numerical experiment is the preserved homogeneity regarding the atomic density of the reconstructed volume in both cases and for all considered detector efficiencies (see figures B.3 and B.4). Naturally, the atomic density

decreases with a decreasing ρ_{Det}, since the number of reconstructed atoms becomes less.

4.1.7. Reconstruction of experimental data of an AlN/Cu multilayer structure

In this section, a final demonstration of the beneficial properties of the here developed reconstruction technique is made by applying it to real experimental data. To this end, a multilayer emitter structure is reconstructed and the result is compared to the reconstruction achieved by the conventional geometric approach. The tip contained a AlN/Cu layer structure with a layer thickness of 4 nm each. On top of the mentioned layer structure, a chromium layer has been sputtered, in order to protect the underlying layers during a focused ion beam treatment, carried out prior to the atom probe measurement. The tip has been field evaporated with a laser-assisted atom probe. The laser power was set to a relatively high value of 45 mW. The resulting data set contained approximately 16 million detected atoms.

For both approaches, the input tip radius for the reconstruction was set to 43 nm and the shank angle had a value of 10°. The image compression factor was equal to 0.7. For the new algorithm, the sampling parameters have been chosen to $N_P = 280000$ and $N_R = 90000$. A 6 nm thick slice through the middle of the reconstructed tip volumes for both techniques is shown in figure 4.21. As it can be seen, the reconstructed tip volumes differ clearly. The new algorithm delivers a varying lateral size due to the changing averaged evaporation field of the involved species. The evaporation fields become important, since the calculated surface profiles are scaled according to equation (4.11). The lateral scaling of the emitter profile helps finding reasonable and relatively constant layer thicknesses.

Since the exact value for the evaporation field of aluminum nitride is unknown, it was estimated to 40 V/nm. This large value was chosen because the density distribution of events on the detector in the end of the measurement indicated that the evaporation field of AlN must be higher than the evaporation field of silicon, which has a value of 36 V/nm.

The main difference between the two reconstructed volumes is the appearance of the AlN/Cu interfaces and the AlN/Cr interface at the top. In figure 4.21a), the interfaces look sharper, while in b), some of the copper layers intermix with the respective underlying AlN layer in the center of the volume. The thicknesses of the copper layers in b) is overall strongly varying in the direction perpendicular to the tip axis. In the center, the Cu layers have their maximum thickness, but further away from the tip axis they appear to be significantly thinner. At the edge of the volume, the thicknesses increase again. This increase goes along with a diffuse interface shape. In general, the AlN layers seem to be much thicker than the copper layers. In addition, the interface between the chromium layer

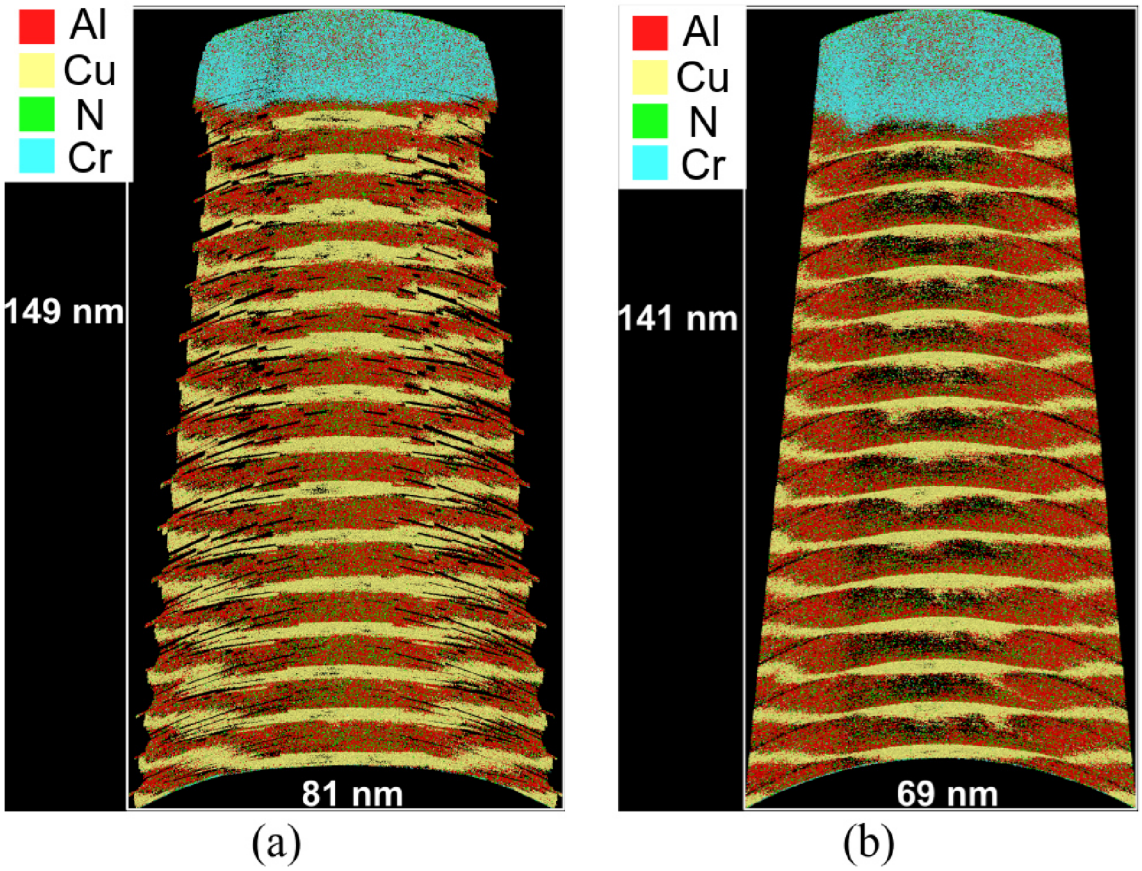

Figure 4.21.: Comparison of the two results for the reconstruction of an AlN/Cu layer structure. The pictures show a 6 nm thick slice through the middle of the reconstructed volumes. The outcome of the new approach is shown in (a) and the respective result of the conventional geometric approach is illustrated in (b). (Courtesy of Johannes Juteraeng)

and the AlN layer below is not flat, although flat layers could be expected in this particular case.

In contrast to these observations, the interface between chromium and AlN as well as the interfaces between Cu and AlN are more flat close to the tip axis in a). Furthermore, intermixing between the layers is hardly visible in the inner region of the tip volume. The layer thicknesses are more homogeneous and the difference between the thicknesses of the Cu layers and the AlN layers do not seem to be as large as in b). In the outer part, the layers also become more indefinite and seem to be bent upwards.

The beneficial effect of the new reconstruction approach becomes more obvious by evaluating the atomic density in the reconstructed volumes. As it can clearly be seen in figure 4.21, the center of the reconstruction in b) shows a strongly varying density. Especially, the AlN layers appear to be very sparse compared to the copper layers and the outer part of the tip volume. In contrast to this observation, the atomic density in the center

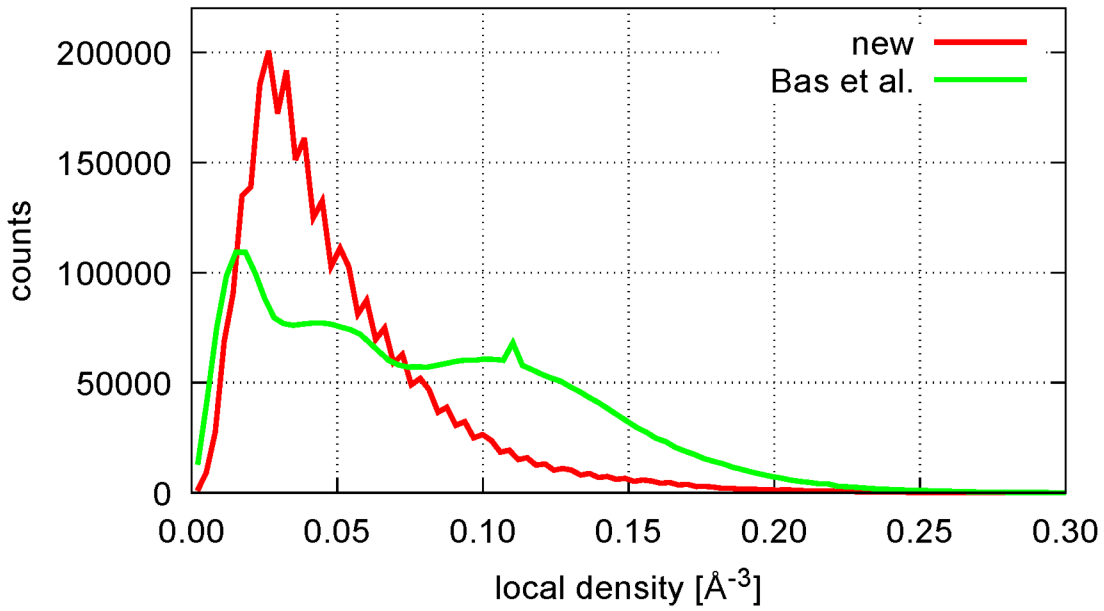

Figure 4.22.: The atomic density inside a cylinder around the tip axis with a radius of 15 nm. The plot shows the number of atoms with a certain atomic density in their vicinity (0.8 nm).

of the reconstruction belonging to the new approach looks significantly more homogeneous (see figure 4.21a)). Only in the outer parts of the volume, density fluctuations can be seen.

In order to underline the observation of an improved density in figure 4.21a), figure 4.22 shows a histogram of the atomic density, calculated in a cylinder located symmetrically along the tip axis with a radius of 15 nm for both approaches. The plot clearly proves that the new technique delivers a significantly more homogeneous atomic density. The well-known density fluctuations between different layers in the conventional point projection approach could successfully be improved, as it was already demonstrated in figures 4.18 and 4.19.

The density profile along the tip axis is illustrated in figure 4.23. Here, the improvement of the local density is again clearly visible. Despite a few peaks close to -1000 and -700 $\mathring{A}$, the fluctuations of the atomic density for the new method are not as severe as the fluctuations, which can be observed in the case of the conventional method. The profile corresponding to the point projection approach allows to distinguish between the copper layers (high density) and the sparse AlN layers.

The concentration profiles for both volumes are illustrated in figures 4.24 and 4.25. These profiles have been observed within a cylinder volume with a radius of 12 nm, located around the tip axis. Both profiles reveal a clearly oscillating behavior regarding the copper, the aluminum, and the nitrogen content. Differences can be identified close to the chromium layer at the top. The copper layers in figure 4.25 are becoming thinner towards the top.

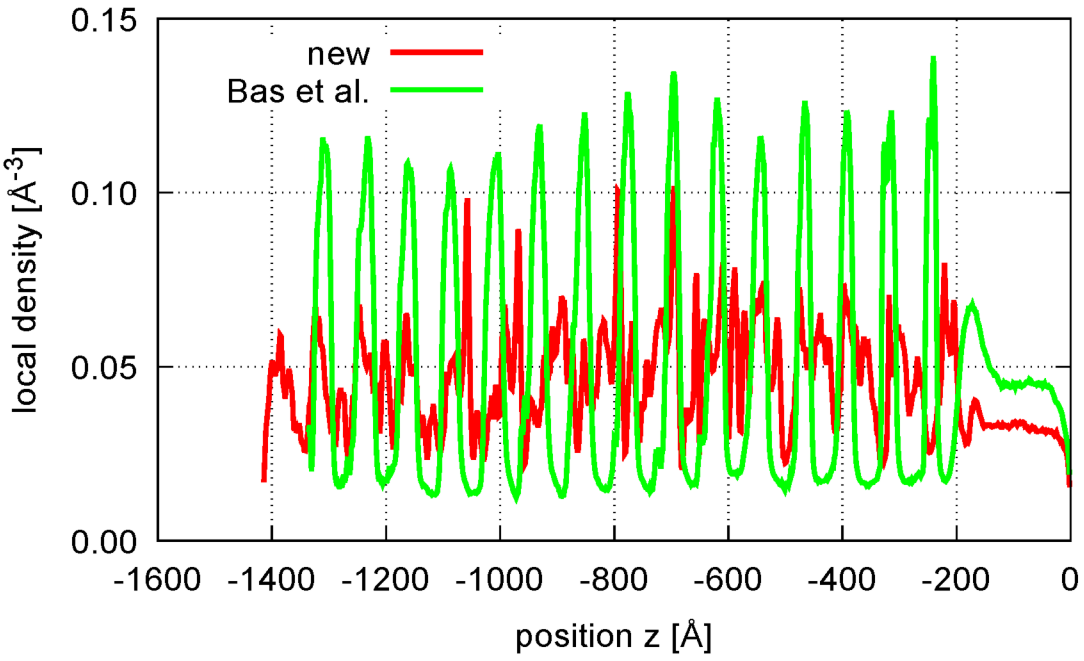

Figure 4.23.: Comparison of the density profiles for the reconstructed volumes shown in figure 4.21. Like in figure 4.22, the analysis has been carried out in a cylinder volume with a radius of 15 nm around the tip axis. The presented values have been derived by averaging the density values within intervals of 2 *Å*.

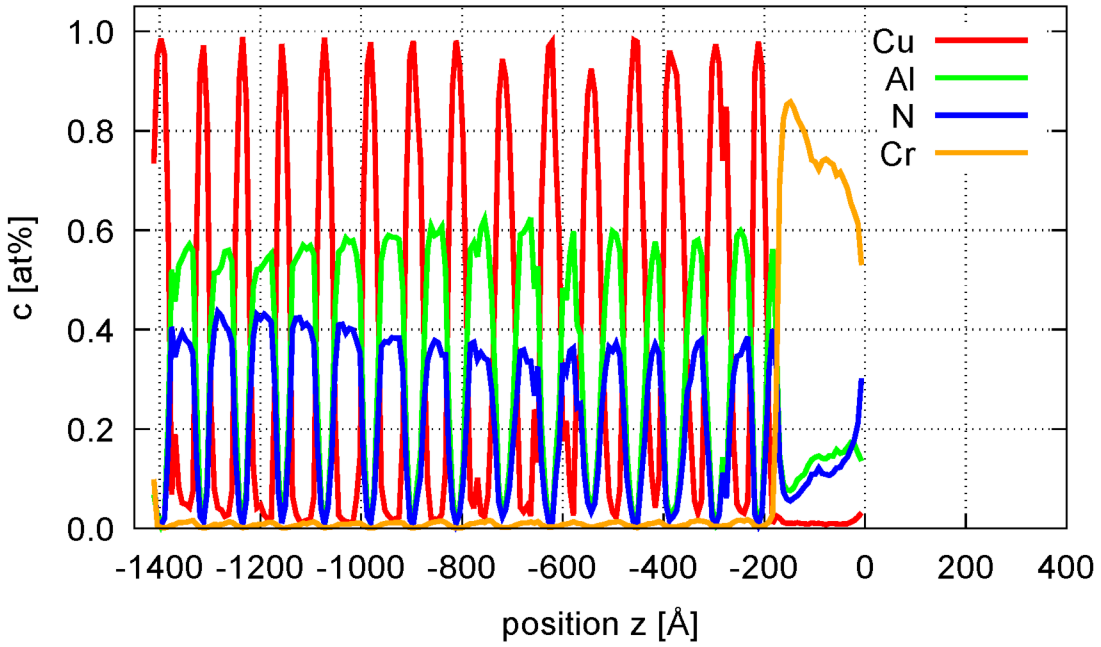

Figure 4.24.: Concentration profile of the reconstruction of the AlN/Cu layer structure resulting from the new algorithm. The volume has been shifted along the tip axis so that the top is located at a height of 0 *Å*.

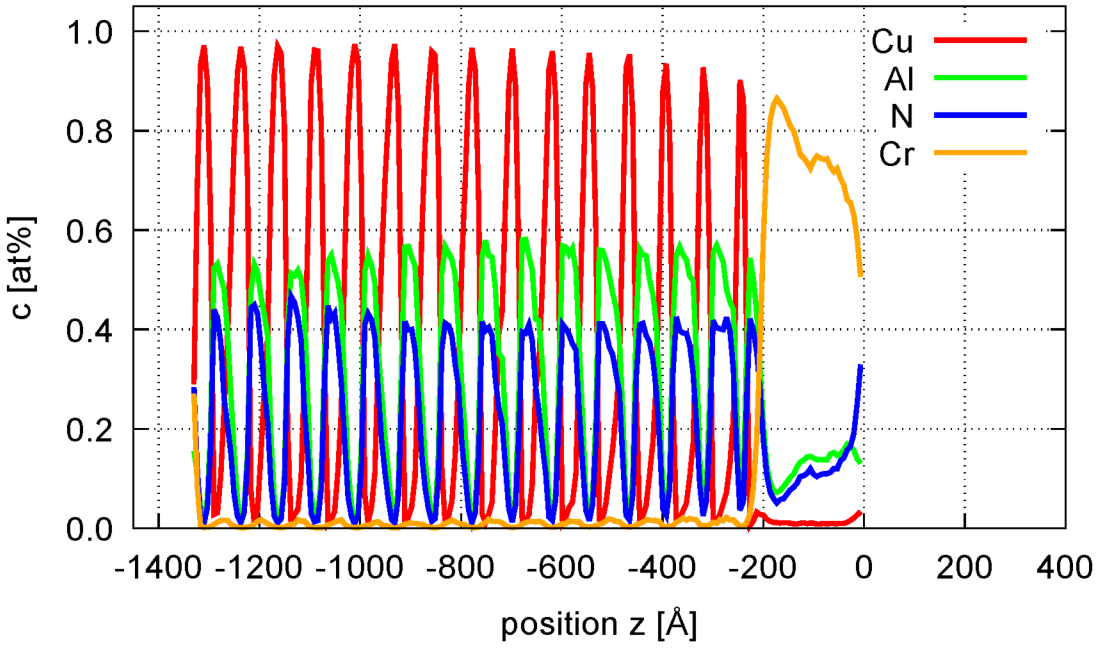

Figure 4.25.: Concentration profile of the reconstruction of the AlN/Cu layer structure resulting from the point projection algorithm.

Here, the thicknesses of the AlN layers are approximately twice as large as the thicknesses of the copper layers. Further away from the top, the thicknesses of the copper become almost equal in comparison to the AlN. However, the concentration profiles are misleading in this regard, since the atomic density fluctuations shown in figure 4.23 are severe. Due to the sparse density of the AlN layers below the copper, the copper layers at the bottom appear slightly thicker than they really are.

The thicknesses in figure 4.24, showing the concentration profile in the reconstruction with the new method, are more constant at the top. The copper layers in this region have almost the same thicknesses as the AlN layers, except for the layer at the very top. At the bottom, the thicknesses of the AlN layers increase. Here they are approximately twice as thick as the copper layers.

Before the experiment it was already known that the layers within the structure had a thickness of 4 nm. 15 individual layers can be identified in the measured data set. This means that a total thickness of approximately 1200 $\AA$ of the entire layer structure without the chromium coating can be expected. In figure 4.25, the AlN/Cu layers are visible from $-200\,\AA$ to approximately $-1300\,\AA$ regarding their height, yielding a total thickness of $1100\AA$. In comparison, the thickness of the whole layer stack in figure 4.24 is $1200\,\AA$, ranging from $-200\,\AA$ to approximately $-1400\,\AA$. The discrepancy can be explained by the rigid movement of the spherical emitter surface in the conventional reconstruction. The

strong compression in the case of the conventional method could be avoided by the new reconstruction approach. The improvement is mainly achieved by the local lifting of the individual profile rings, as it is described in section 4.1.4.

In both composition profiles a lack of nitrogen is observed. An overall calculation of the amount of the different species delivers 56.1 at% of copper, 23 at% of aluminum, 7.1 at% of chromium and only 13.8 at% of nitrogen. From stoichiometry, one would expect the same amount of nitrogen as of aluminum. However, this lack of nitrogen is not related to a failure of both reconstruction methods.

One reason for the lack of nitrogen could be the increasing temperature of the tip during the experiment. Especially the copper could be heated up significantly due to the absorption of energy from the laser. This would consequently yield an indirect heating of the AlN and therefore, the amount of detected nitrogen decreases.

In the composition profile belonging to the conventional approach (figure 4.25), the nitrogen content in the AlN layers is higher than in the reconstruction performed with the new approach. But this observation can be explained by the clearly decreased density of atoms in these layers, which can be seen in figure 4.21b). Since the amount of atoms in the AlN layers is decreased, statistical fluctuations have a larger impact on the composition and might therefore lead to seemingly more reasonable results. Nevertheless, because of the low and inhomogeneous density, the reliability of the composition profile shown in figure 4.25 has to be questioned and the result achieved with the help of the new approach should be considered as more reliable.

However, beside the impressive improvements of the here presented approach, some drawbacks are still visible. In the outer part of the reconstructed volume, the layers are bent upwards and the interfaces are not as clear as in the center. Additionally, also the atomic density appears to be more inhomogeneous. At this point, it has to be emphasized again that the new approach assumes a steady-state situation of the field evaporation process, where the surface shape is constant for a certain amount of time. Unfortunately, the field evaporation of a layer structure with thin layers and atomic species with strongly varying evaporation fields never reaches a steady state. Due to the differences regarding the evaporation field, the surface is constantly changing and therefore, the here presented approach cannot be expected to yield perfectly flat layers.

Nevertheless, the quality of the reconstruction might still be further improved by a more elaborated choice of the sampling parameters N_P and N_R. At this moment, the two parameters are chosen to be constant during the reconstruction. Possibly, an oscillating value for N_P and N_R could yield even better results for layer structures similar to the here discussed example. In this way, the lack of a constant surface curvature might be moderated and even the outer part of the volume might reveal more defined interfaces between the

layers.

In conclusion, this section demonstrated the capability of the new reconstruction technique to improve well-known artifacts of the conventional approach for the case of emitter structures with rotational symmetry. For those cases, the new algorithm provides a reasonable alternative to the established point projection technique and can easily be applied to realistic data sets containing several millions of detected ions.

Of course, a more versatile technique, which would improve the reconstruction of any kind of emitter structure regardless its degree of symmetry, is desired for the evaluation of modern atom probe experiments. Since the above described concept has proven to yield promising results in a reasonable time, the basic idea of extracting the emitter shape from the measured density of detected events needs to be extended. In the next chapter, as a final step of this work, such an approach is described and tested in a similar way, as it has been done in this section.

Chapter 5.

Remaining steps towards a general reconstruction approach

In chapter 4, the clear improvement given by the new reconstruction algorithm has been demonstrated. Nevertheless, those achievements are not yet the end of the story. Since the approach introduced in section 4.1 is based on the assumption of the presence of rotational symmetry, the technique is still not applicable to the reconstruction of arbitrary field emitter structures. However, structures without rotational symmetry are very common. A simple example of such a case is already given by a mono-atomic atom probe tip that is field evaporated using laser pulses. Since the light hits the tip perpendicular to the axis, one side of the tip will be illuminated (i.e. heated) more than the other [44]. This enhanced introduction of heat at one side will very likely lead to a preferred desorption of material [97].

Consequently, the field emitter will develop a shape, which has no rotational symmetry and so the corresponding density of detector events can be expected to be biased. As an example for such a situation, a snapshot of the simulation of a field emitter, which develops an asymmetric shape similar to a laser-illuminated tip, is shown in figure 5.1. In figure 5.2, the corresponding detector pattern is plotted. It is obvious that the presented algorithm in chapter 4 cannot be applied in this case. A tip surface as shown in figure 5.1 is clearly representing a very common situation, where the steady state can be described by an asymmetric emitter shape. The radius of curvature in the direction of the laser illumination is shown in figure 5.3, in order to support this statement. Left from the center, the curvature is rather small, yielding a large radius of curvature. At the maximum of the surface, the curvature has its highest value and consequently, the radius of curvature is significantly smaller than the initial curvature radius of 30 nm.

The detector pattern belonging to the steady-state situation of the illustrated tip shown in figure 5.2 underlines the influence of the asymmetric tip shape. If the density of events is

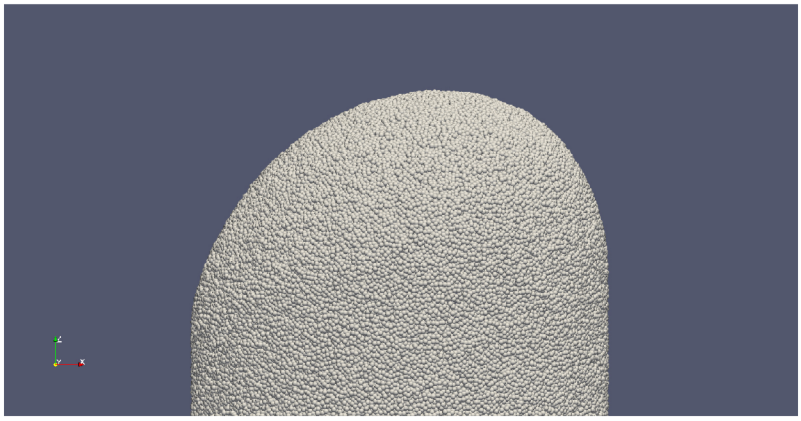

Figure 5.1.: Surface shape of a tip with an amorphous structure and an inhomogeneous evaporation behavior. It is clearly visible that the shape has no radial symmetry. The illustrated situation is intended to model the field evaporation induced by a laser pulse.

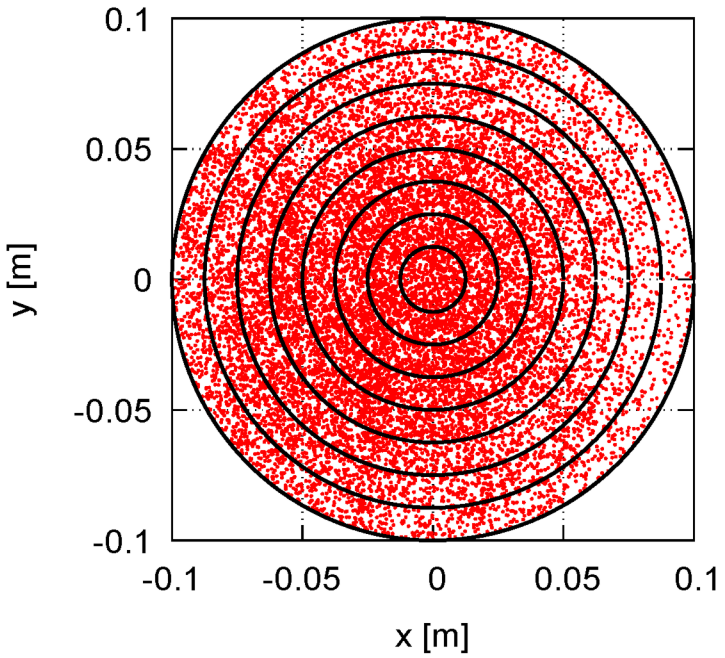

Figure 5.2.: The detector pattern corresponding to a steady-state situation of the field evaporation of the tip shape illustrated in figure 5.1. The rings divide the detector into several parts representing a certain range of detection angles.

examined along the azimuth φ in each of the illustrated rings of the detector, the enhanced amount of evaporated material on one side of the tip can be obtained. As an example, in figure 5.4, the density of events in the second, fifth, and seventh ring is plotted over the corresponding angle φ. In the plot, the influence of the strongly biased emitter shape becomes obvious. In the 5^{th} and 7^{th} ring, the density of detected events is significantly

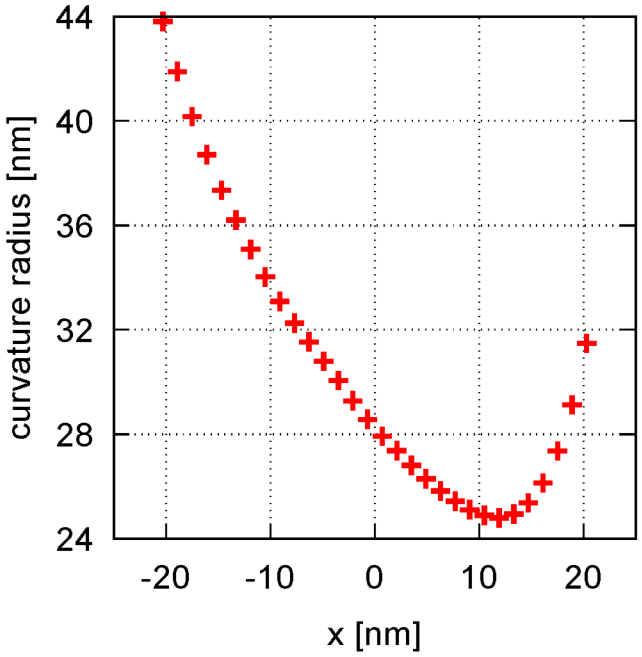

Figure 5.3.: Radius of curvature of the tip surface after one-sided laser illumination.

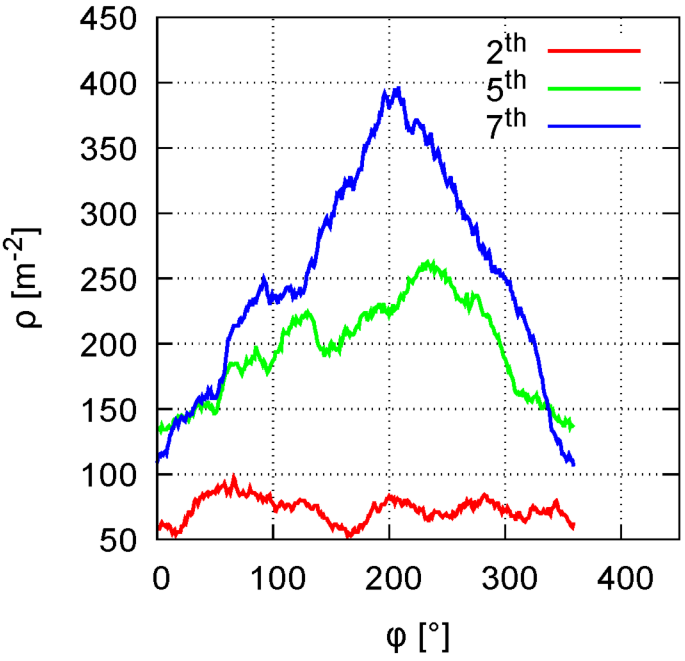

Figure 5.4.: The local density of measured ion impacts along the azimuthal direction for different rings in figure 5.2.

smaller at 0° than at the opposite side at around 180°. This effect becomes smaller in the vicinity of the detector center, as it can be seen for the event density of the second ring.

In order to deal with a detector pattern like this, the reconstruction algorithm needs to be able to identify the shape and location of the lines of constant emission angle θ around the entire emitter surface. In the algorithm presented in section 4.1, these lines of constant emission angle were simply given by circles, due to the assumed rotational symmetry. In a situation, as it is shown above in figures 5.2 and 5.4, the description of these lines by a circle no longer applies.

In the following, a technique designed to treat cases like the one described above is discussed. In this concept, the idea of determining the emitter surface shape from the event distribution is maintained. As a major improvement step, a relation between the event density on the detector and the Gaussian curvature at the surface is derived, which helps to find a reasonable description of the emitter surface shape.

5.1. A reconstruction approach for asymmetric emitter structures

In the following, a general approach for the reconstruction of arbitrary emitter structures will be presented. This approach is designed to calculate the emitter surface shape, which shall be described by cylindrical coordinates. This means, the tip surface is described by a radius r and an azimuth angle φ at each point. In order to define the surface, one needs to know the radius $r(\varphi)$ and the corresponding height $h(r, \varphi)$. The approach still assumes convexity of the emitter surface and a cylindrical shaft. Apart from that, no further assumptions for the tip shape are required. The concept for the tip shape calculation has been submitted within the scope of this work [13].

Like in the previous approach for the reconstruction of structures with rotational symmetry, this technique also relies on the local density of detected events on the detector. Furthermore, it is again assumed that the amount of evaporated material from a specific location on the emitter surface is directly proportional to the projected area a_i of this particular surface region onto the emitter base. In contrast to the concept described in section 4.1, the detector and the tip surface cannot be divided into rings. For a generalization of the approach, detector and tip surface need to be divided into segments with a constant angle increment $\Delta\theta$ and $\Delta\Phi$ on the detector, and $\Delta\theta$ and $\Delta\varphi$ on the tip surface (see figure 5.5a) and b)). Since no rotational symmetry can be assumed, it is very important to distinguish between the azimuthal emission angle φ and the azimuthal detection angle Φ. In cases without rotational symmetry, the assumption that these angles are the same no

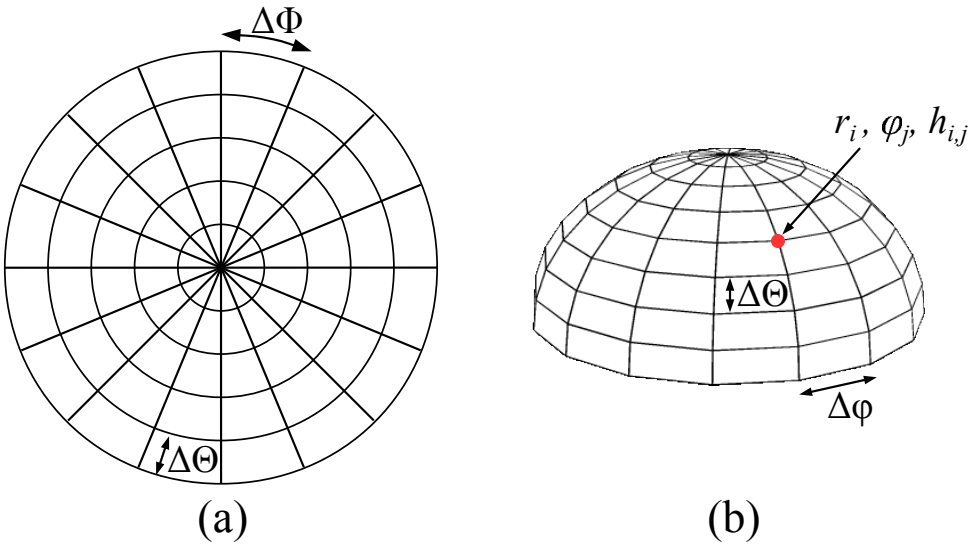

Figure 5.5.: For the generalized approach, a predefined segmentation of the detector and the tip surface is required. In (a), the segmentation of the detector is illustrated. The sketch in (b) shows the segmentation of the emitter surface into nodes with coordinates $(r_i, \varphi_j, h_{i,j})$.

longer applies.

Due to the fixed segmentation of the surface, in the following, the radius at the angle θ_i and φ_j will be denoted $r(\theta_i, \varphi_j) = r_{i,j}$ and the height will be denoted $h(r_i, \varphi_j) = h_{i,j}$. The radius of the individual surface points remains fixed, which means $r_{i,j} = r_i$. The task of the generalized reconstruction technique is the determination of the height $h_{i,j}$ at each surface node. To this end, a relation between the local value for the Gaussian curvature $K(\theta, \Phi)$ at the tip surface and the event density at the corresponding region on the detector is needed. Given the knowledge about the curvature at discrete positions on the surface, the corresponding heights can be adjusted accordingly.

First, the algorithm needs to identify the value for the local Gaussian curvature $K(\theta, \Phi)$, which is needed at the emitter surface at a position with a specific angular direction (θ, Φ). In general, the Gaussian curvature is defined as the inverse of the product of the two main curvature radii R_1 and R_2 of a curved surface:

$$K = \frac{1}{R_1 \cdot R_2}. \tag{5.1}$$

In practical terms, the Gaussian curvature of a convex emitter can also be seen as the ratio between the "angular" surface $dS = d\alpha\, d\beta$ (with the small angle increments $d\alpha$ and $d\beta$) and the corresponding area dA related to a certain surface segment, which yields

$$K = \frac{dS}{dA}. \tag{5.2}$$

As already mentioned in section 4.1.1, the number dN of evaporated ions from a surface segment in a steady state is proportional to the projected area $da = dA \cdot \cos(\theta)$ onto the emitter base:

$$dN = \frac{\Delta z \, dA}{\Omega} \cdot \cos(\theta). \tag{5.3}$$

Here, Ω stands for the atomic volume (assumed to be constant in this case), and Δz represents the emitter shrinkage after the evaporation of N atoms.

Rearranging equation (5.3) for dA and inserting it into equation (5.2) yields

$$K = \frac{\Delta z \cdot \cos(\theta)}{\Omega} \frac{dS}{dN} = \frac{\Delta z \cdot \cos(\theta)}{\Omega} \frac{1}{\rho_D}. \tag{5.4}$$

This equation represents a relation between the measured density of events $\rho_D(\theta, \Phi)$ on the detector and the Gaussian curvature $K(\theta, \Phi)$ of the corresponding surface segment. This relation can now be used for the determination of the height $h_{i,j}$ of each surface node (represented by the red dot in figure 5.5b)).

In the following, an iterative algorithm developed for this task is described [13].

5.1.1. Iterative calculation of the surface profile

The relation between the Gaussian curvature and the density of events on the detector is now used for the determination of a height profile, which describes the field emitter. As it is shown in figure 5.5, detector and surface profile are split into individual nodes. The density $\rho_D(\theta, \Phi)$ is measured at each node on the detector. For any position between the nodes, a simple linear interpolation is made.

The height values $h_{i,j}$ at each of the nodes need to be found, in order to describe the emitter surface correctly. To this end, the emitter shape is initially described by a hemisphere. The normal vector, given at each node on the surface, points into a specific direction (θ_i, Φ_j) towards the detector. Consequently, at each node on the surface, a certain target value for the Gaussian curvature $K(\theta_i, \Phi_j)$ can be found with the help of equation (5.4) and a continuous function for the detector density $\rho_D(\theta_i, \Phi_j)$ (given by linear interpolation). Once all target values for the curvature are known, the calculation of the heights $h_{i,j}$ can start. This height calculation is done in cylindrical coordinates r and φ. The cylindrical coordinates are linked to the detector coordinates θ and Φ via the normal

vector $\vec{n} = (n_x, n_y, n_z)^T = \partial h/\partial r \times \partial h/\partial \varphi$ at each node on the surface:

$$\tan(\theta) := \frac{\sqrt{n_x^2 + n_y^2}}{n_z} \tag{5.5}$$

$$\tan(\Phi) := \frac{n_y}{n_x} \tag{5.6}$$

With the help of differential geometry considerations and the description of the height by $h = h(r, \varphi)$, the Gaussian curvature can then be expressed by [98]:

$$K(\theta, \Phi) = \frac{r^2 \frac{\partial^2 h}{\partial r^2} \left(\frac{\partial^2 h}{\partial \varphi^2} + r \frac{\partial h}{\partial r} \right) - \left(\frac{\partial h}{\partial \varphi} - r \frac{\partial^2 h}{\partial r \partial \varphi} \right)^2}{\left(r^2 \left(1 + \left(\frac{\partial h}{\partial r} \right)^2 \right) + \left(\frac{\partial h}{\partial \varphi} \right)^2 \right)^2}. \tag{5.7}$$

The derivatives in equation (5.7) can further be expressed by the following approximations:

$$\frac{\partial h}{\partial r} \approx \frac{h_{i+1,j}^{(l)} - h_{i-1,j}^{(l)}}{2\,\Delta r}; \qquad \frac{\partial h}{\partial \varphi} \approx \frac{h_{i,j+1}^{(l)} - h_{i,j-1}^{(l)}}{2\,\Delta \varphi} \tag{5.8}$$

$$\frac{\partial^2 h}{\partial r^2} \approx \frac{h_{i+1,j}^{(l)} + h_{i-1,j}^{(l)} - 2\,h_{i,j}^{(l+1)}}{\Delta r^2}; \qquad \frac{\partial^2 h}{\partial \varphi^2} \approx \frac{h_{i,j+1}^{(l)} + h_{i,j-1}^{(l)} - 2\,h_{i,j}^{(l+1)}}{\Delta \varphi^2} \tag{5.9}$$

$$\frac{\partial^2 h}{\partial r\,\partial \varphi} \approx \frac{h_{i+1,j+1}^{(l)} + h_{i-1,j-1}^{(l)} - h_{i+1,j-1}^{(l)} - h_{i-1,j+1}^{(l)}}{\Delta r\,\Delta \varphi}. \tag{5.10}$$

The indices l and $l + 1$ in these expressions represents the height value at the iteration step l or $l + 1$ of the height calculation process. It is very important to mention that the height value at the following step $l + 1$ (which needs to be determined) only appears in the unmixed second derivatives in (5.9). The insertion of equations (5.8-5.10) into (5.7) yields a quadratic equation for the height $h_{i,j}^{(l+1)}$ in iteration step $l + 1$. This quadratic equation has the solution

$$h_{i,j}^{(l+1)} = -\frac{\delta}{2} + \sqrt{\frac{\delta^2}{4} - \xi + \beta + \alpha \cdot \hat{K}(\theta_i, \Phi_j)}. \tag{5.11}$$

The Gaussian curvature values $\hat{K}(\theta_i, \Phi_j)$ in (5.11) are the result of a normalization given by $\hat{K}(\theta_i, \Phi_j) = \gamma \cdot K(\theta_i, \Phi_j)$ (for the normalization factor γ see below). Furthermore, in

this solution several abbreviations have been used:

$$\alpha := \frac{\Delta r^2\,\Delta\varphi^2}{4\,r_i^2}\cdot\left(r_i^2\left(1+\left(\frac{h_{i+1,j}^{(l)}-h_{i-1,j}^{(l)}}{2\,\Delta r}\right)^2\right)+\left(\frac{h_{i,j+1}^{(l)}-h_{i,j-1}^{(l)}}{2\,\Delta\varphi}\right)^2\right)^2 \tag{5.12}$$

$$\beta := \frac{\Delta r^2}{4\,r_i^2}\cdot \left(\frac{h_{i,j+1}^{(l)}-h_{i,j-1}^{(l)}}{2}-r_i\,\frac{h_{i+1,j+1}^{(l)}+h_{i-1,j-1}^{(l)}-h_{i+1,j-1}^{(l)}-h_{i-1,j+1}^{(l)}}{\Delta r}\right)^2 \tag{5.13}$$

$$\xi := \frac{\left(h_{i+1,j}^{(l)}+h_{i-1,j}^{(l)}\right)\cdot\left(h_{i,j+1}^{(l)}+h_{i,j-1}^{(l)}\right)}{4}+\frac{\Delta\varphi^2\,r_i}{8\,\Delta r}\cdot\left(\left(h_{i+1,j}^{(l)}\right)^2-\left(h_{i-1,j}^{(l)}\right)^2\right) \tag{5.14}$$

$$\delta := -\frac{\left(h_{i+1,j}^{(l)}+h_{i-1,j}^{(l)}+h_{i,j+1}^{(l)}+h_{i,j-1}^{(l)}\right)}{2}-\frac{r_i}{4}\cdot\frac{\Delta\varphi^2}{\Delta r}\cdot\left(h_{i+1,j}^{(l)}-h_{i-1,j}^{(l)}\right) \tag{5.15}$$

The value for the Gaussian curvature $\hat{K}(\theta_i,\Phi_j)$ can be obtained with the help of equation (5.4) and the measured event density

$$\rho(\theta_i,\Phi_j) := \frac{N(\theta_i,\Phi_j)}{\sin(\theta_i)\cdot\Delta\theta\,\Delta\Phi} \tag{5.16}$$

Since the tip radius R_0 is fixed and the overall projected surface area is given by $\pi\cdot R_0^2$, a normalization step is required, so that the projected surface area matches the correct value. To this end, the Gaussian curvature values given by equation (5.4) have to be multiplied with a constant normalization factor γ, before the evaluation of the height values can be performed. This normalization factor is given by

$$\gamma = \left[\int_0^{2\pi}\int_0^{\pi/2}\frac{\cos(\theta)\,\sin(\theta)}{K(\theta,\Phi)}\,d\theta\,d\Phi\right]\cdot\left(\pi\,R_0^2\right)^{-1}. \tag{5.17}$$

Starting with a hemispherical shape, in every iteration step, the height $h_{i,j}^{(l+1)}$ at each position of the surface grid is evaluated with the help of equation (5.11). To this end, the direction of the normal vector at each surface node position needs to be recalculated, in order to enable the evaluation of the corresponding event density, which is required. Once all new height values have been determined, these new values are set and the evaluation of equation (5.11) for every node is repeated. This scheme is applied repeatedly, until the height values have converged towards the equilibrium configuration with a sufficient accuracy.

The here presented scheme cannot be applied to surface location for which no event

density is measured. Since the FOV of an atom probe device is limited (to about 45° in modern instruments), a reasonable boundary condition for these surface nodes is needed. Two possibilities exist. Either the heights of the nodes at the boundary of the field-of-view are fixed, or the directions of the respective surface normals at the boundary positions are set to a constant value. In any case, it is difficult to choose a reasonable value for either the heights or the normal directions at a maximum detection angle of 45°, since these values are unknown prior to the reconstruction.

To this end, it is reasonable to extend the number of nodes considered in the iterative algorithm described above, so that all nodes until the maximum emission angle $\theta_{max} = 90°$ are included. The boundary condition for the normal directions at an angle of 90°, which means at the very edge of the surface, is known at any time. At the edge of the surface, one can be sure that the surface normals point into the direction with $\theta_i = 90°$.

The remaining question is how to deal with the unknown values for the Gaussian curvature at the positions of the surface nodes outside the FOV. In this work it is assumed that the Gaussian curvature for these nodes is given by the average curvature value of the nodes inside the FOV. With this assumption, the iterative algorithm for the height value calculation can be performed for every node at the surface, regardless, whether its normal direction lies inside or outside the field-of-view.

5.1.2. Example calculation for an asymmetric emitter structure

In this section, the technique for the identification of the emitter surface shape described above shall be tested. To this end, the FEV of an example emitter structure has been simulated. The tip has an amorphous structure with a constant atomic density of 6 atoms per cubic nanometer. In addition, the tip contains a cylinder volume with a different atom type compared to the surrounding matrix. This cylinder has a radius of 8 nm and is shifted 8 nm away from the tip axis in lateral direction (see figure 5.6). In the following example, the evaporation field of the atoms inside the cylinder volume (called “type 2” atoms in the following) has been chosen to be 32 % higher than the evaporation field of the matrix atoms (red atoms in figure 5.6).

Consequently, once the steady-state configuration of the tip surface has been reached, the cylinder forms a protrusion at the tip apex. Due to this “defect” in the emitter shape, local magnification occurs and the type 2 atoms reaching the detector cover a relatively large area on the detector. At the same time, the density distribution on the detector in the steady state clearly shows a reduced density of events, where the type 2 atoms are detected. The density of measured events in the steady state of the field evaporation is shown in figure 5.7. As it can be seen, the local magnification caused by the higher evaporation

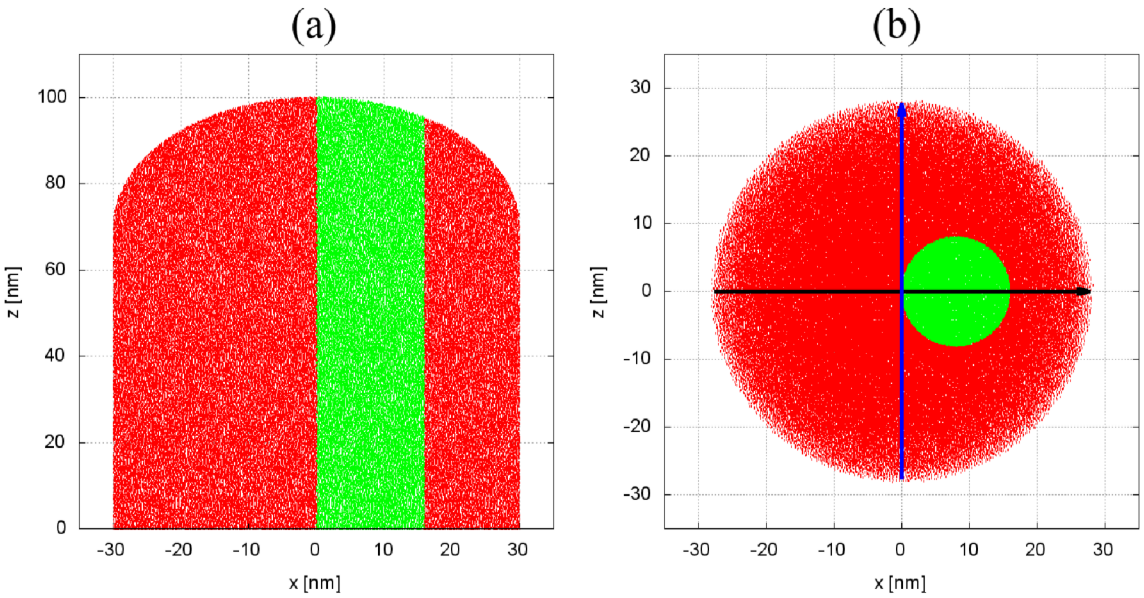

Figure 5.6.: In (a), a slice through the middle of the emitter structure is shown. In green, the cylinder containing a different atom type (named "type 2" in the text) is illustrated. The same structure is shown from the top in (b). The arrows define two analysis directions for the calculated emitter profiles.

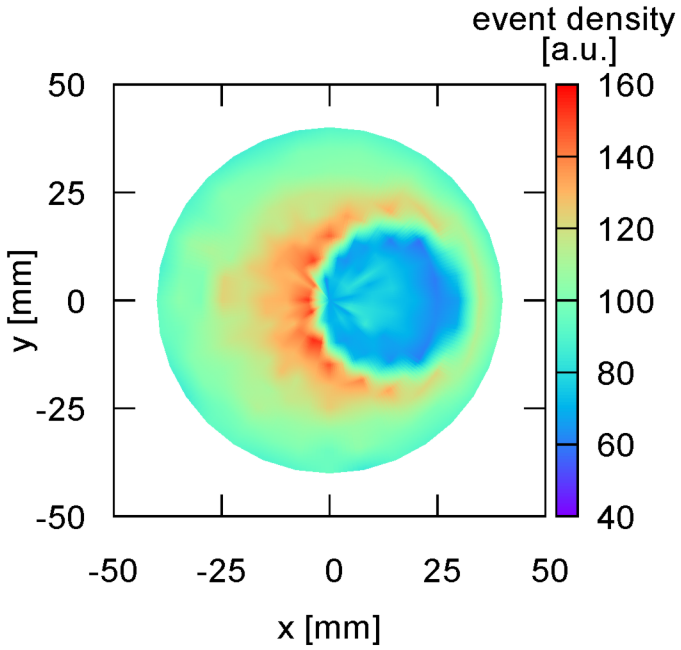

Figure 5.7.: The measured density of detected ions in the steady state of the field evaporation of the emitter structure illustrated in figure 5.6 is shown. Due to the higher evaporation field of the type 2 atoms, the density is lower, where these atoms are detected. The region with a decreased density has a circular shape, which can be explained by the circular cross section of the cylinder structure inside the tip. The low density region is surrounded by a steep increase of the density.

field of the cylinder atoms yields a circular shaped area with a decreased density. A closer look to this low density area reveals a small density gradient towards the center of the detector. Furthermore, the density at the interface between this circular area and the rest of the detector rises sharply, which is mainly caused by the outward deflection of trajectories at the interface between the cylinder and the matrix on the tip surface.

The clearly non-symmetric event density has now been taken into account, in order to test the above presented concept for the shape calculation. The detector and the emitter surface were divided into 18×32 nodes according to figure 5.5 (18 nodes in radial direction and 32 nodes in azimuthal direction). As a first guess, the algorithm started with an initial hemispherical shape of the surface. Then the curvature calculation and the subsequent recalculation of the height of each node has been carried out. Meanwhile, the lateral positions of the surface nodes have been kept constant. The process was stopped, as soon as the largest observed height difference between iteration step l and $l + 1$ among all nodes became smaller than a predefined threshold value of 0.1 %.

The resulting emitter shape is now compared to the original surface in the investigated steady state. In figure 5.8, the calculated surface profile in the direction cutting through the cylinder (the direction of the black arrow in figure 5.6b)) is plotted in red. For comparison, the corresponding slice through the original tip surface is plotted in green. As it can be seen, the asymmetric shape of the profile could be extracted from the detector density since the calculated profile shows a slight protrusion on the right beside the tip axis. Nevertheless, the result doesn't match perfectly. Further improvements might be possible by finding a more suitable boundary condition, which will be discussed later.

The capability of the new concept can be further underlined by the comparison of the calculated profile shown in figure 5.8 with the profile in the perpendicular direction (blue arrow in figure 5.6b)). In figure 5.9, this profile is shown and it is again plotted together with the original surface profile. As it can be seen, the calculated profile in this direction is symmetric to the tip axis. This could be expected, since the cylinder containing the atoms with a higher evaporation field is not present in this direction. The most important observation, which can be made in the figures 5.8 and 5.9, is the capability of the concept to yield a realistic surface shape in different directions regardless the presence of symmetry in the corresponding event density on the detector.

The improvement given by the new concept is better pointed out by the comparison of the radii of curvature of the calculated and the original profile (see figure 5.10). The plot in figure 5.10 impressively shows the similarity of the curvature radii of both the calculated and the original surface profiles at different positions along the direction of the black arrow in figure 5.6b). As it can be seen, left from the tip axis the curvature is lower than on the right. It is even slightly lower than the initial curvature, which would yield a curvature

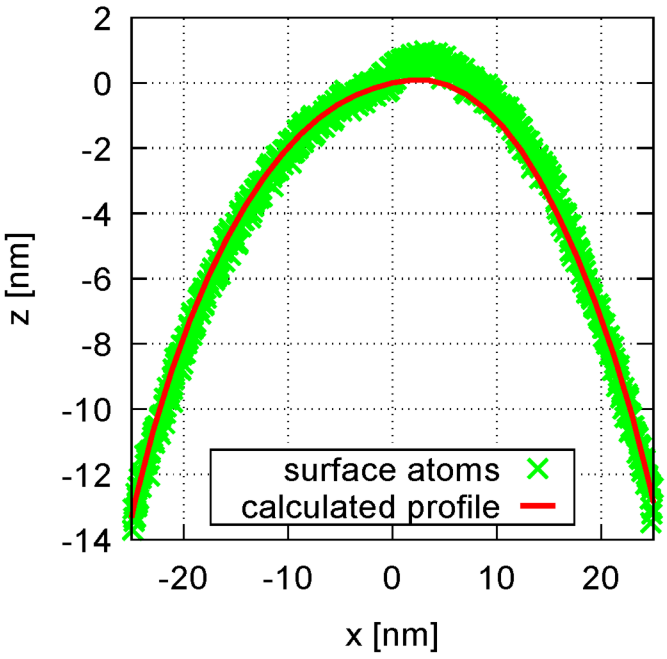

Figure 5.8.: The calculated surface profile (red line) matches well to the original surface profile (green). The asymmetric shape caused by the cylinder can be identified.

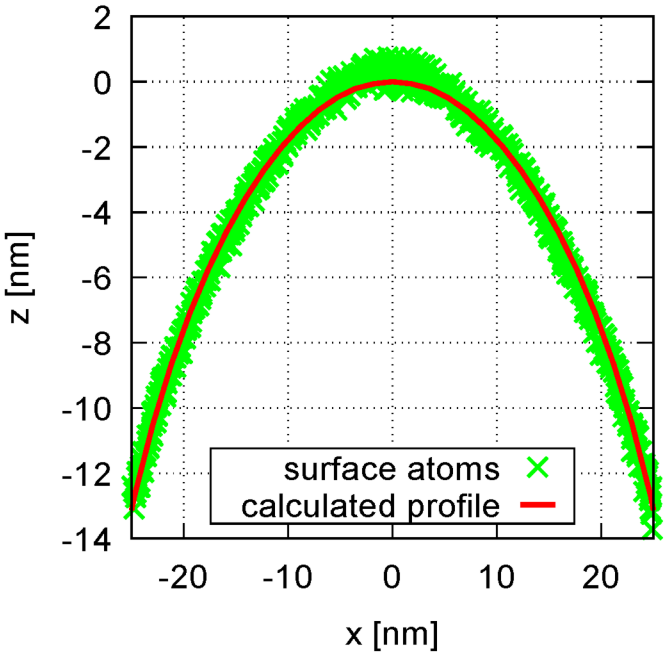

Figure 5.9.: The calculated surface profile (red line) in the perpendicular direction compared to figure 5.8. The red curve matches sufficiently to the original surface shape, plotted in green.

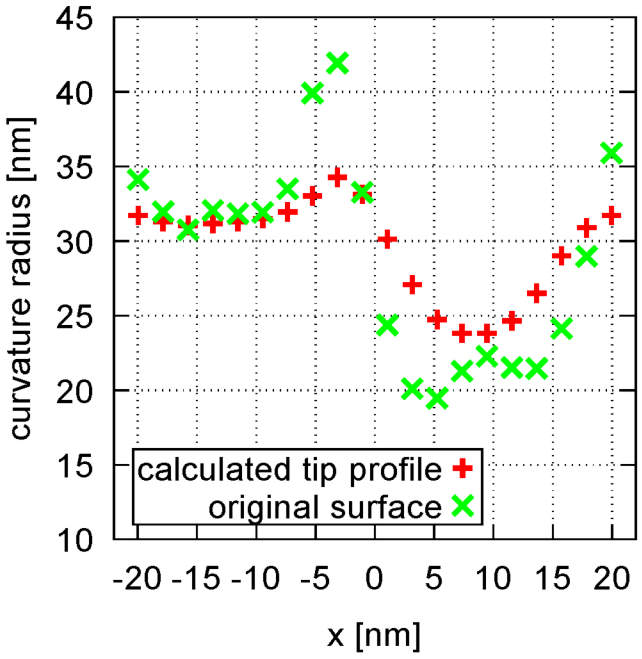

Figure 5.10.: The radii of curvature for the calculated profile and the original emitter surface are shown. The curvature radii have been evaluated in the same direction as in figure 5.8. In this way, the effect of the cylinder containing the type 2 atoms becomes obvious.

radius of 30 nm. Right from the tip axis, the curvature rises very abruptly (the curvature radius drops) as soon as the protrusion caused by the cylinder of material 2 is processed. The drop of the curvature radius takes place at the tip axis and the plateau value on the right is given by (24 ± 2) nm. On the left, a plateau value of (31 ± 2) nm can be identified.

The largest deviation of the curvature in the calculated profile from the original surface curvature can be found near the tip axis. At this position, the curvature radius of the original surface sharply increases. This increase might be explained by the atomic roughness of the surface, which naturally complicates the evaluation of the curvature and might lead to a decreased accuracy.

In conclusion, the here presented enhanced concept for the identification of the emitter profile with the help of the event density on the detector yields promising results. The capability of finding a reasonable description of the tip shape without rotational symmetry could be demonstrated with the help of the simulated emitter structure shown in figure 5.6. The new concept is no longer relying on the assumption of rotational symmetry, as it has been the case in section 4.1, and might therefore be a versatile and easy to use alternative to the conventional point projection approach. Since the calculation of an individual surface profile is sufficiently fast (a few seconds in this example), the technique should be well suitable for the application to measured data sets. With the help of the new shape extraction,

the impact of local magnification effects and the issue of a strongly varying atomic density can be improved in comparison to the standard technique.

The remaining task after the identification of the surface shape is the positioning of the measured atoms on the surface. This can be done with the help of the previously described Delaunay triangulation (see section 2.3).

First, for each node on the previously calculated emitter surface, the corresponding detector position has to be identified with the help of the normal vectors. These normal vectors are already known, since the surface profile calculation required their knowledge. The detector positions, given by the linear projection of the normal vectors onto the detector, can be connected by a Delaunay triangulation. The change of curvature on the surface automatically translates into a varying size of the Delaunay triangles. The effect of the low density of events on the triangulation caused by the cylinder contained in the emitter volume, which is shown in figure 5.7, can be seen in figure 5.11. Due to the low density of measured events, the curvature of the corresponding region on the tip surface increases. This leads to a relatively large average distance of the projected points on the detector, and therefore, to larger triangles in the resulting triangulation.

Once the mesh on the detector is known, it is a straightforward task to identify the embedding triangle for every detected ion. Since each vertex of the Delaunay triangulation is related to one of the nodes of the tip surface profile, it is immediately clear that each individual detected ion needs to be positioned between the surface profile nodes belonging to the respective Delaunay triangle. The final position $\vec{r}_i$ for the atom i on the emitter surface is given by a weighted sum of the positions $\vec{p}_j$ of the surface nodes related to the involved triangle in the detector mesh shown in figure 5.11.

$$\vec{r}_i = \sum_{j=0}^{2} \omega_j \cdot \vec{p}_j. \tag{5.18}$$

The weight factors ω_j can be obtained in the same way as for the electric potential in equation (2.31), using barycentric coordinates (see figure 5.12). To this end, the triangle embedding a certain measured impact position (black triangle in figure 5.12) on the detector, is divided into three smaller triangles (blue). These triangles are defined by two vertices belonging to the black triangle and the impact position (red cross). For example, the small triangle corresponding to the vertex p_1 is given by the impact position and the two opposite vertices p_2 and p_3. Given the overall surface area of the black triangle A_{tri} and the areas of the smaller triangles (T_1, T_2 and T_3), the weight factors are simply obtained by calculating the ratio values $\omega_j = T_j / A_{tri}$.

In the given example, the triangles inside the area indicated by the red dashed circle in

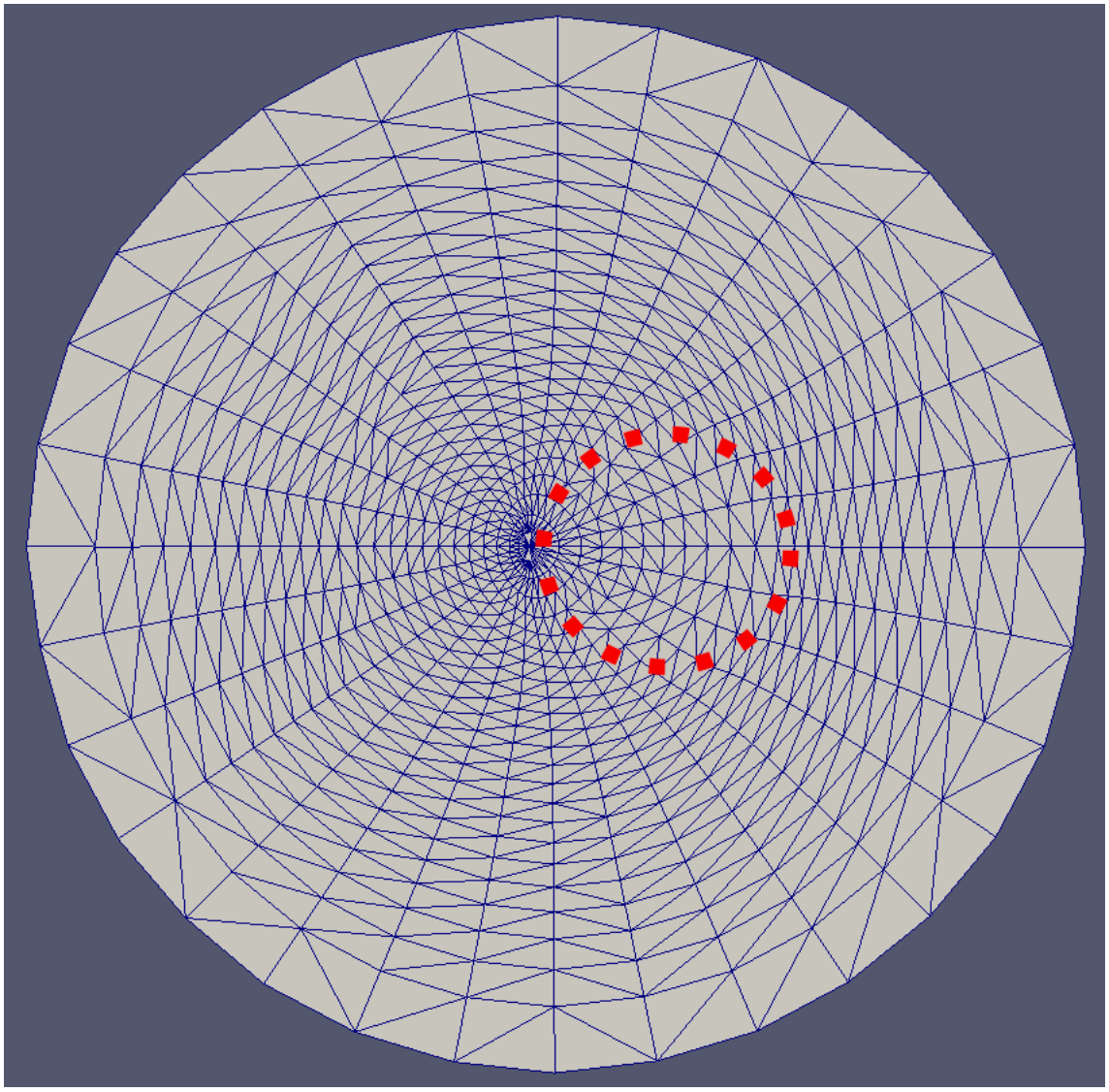

Figure 5.11.: Delaunay triangulation of the detector mesh, resulting from the linear projection of the normal vectors from the calculated emitter surface onto the detector. The influence of the low density region on the triangle sizes can be seen inside the red dashed circle.

figure 5.11 are clearly larger than the triangles left from this area. The increased triangle sizes help to balance the influence of the reduced density of detected ions in this region of the detector (see figure 5.7). Due to the larger sizes, more detected ions will be embedded inside these triangles. Consequently, more atoms will be distributed to the corresponding region in the reconstructed volume (see figure 5.13).

The result of a reconstruction of the emitter structure shown in figure 5.6 for the case of a 32 % higher evaporation field of the type 2 atoms is illustrated in figures 5.13a) and b). The reconstruction has been performed by dividing the data set into smaller portions as it has been proposed in section 4.1.2. The parameters N_P and N_R have been set to 200.000 each

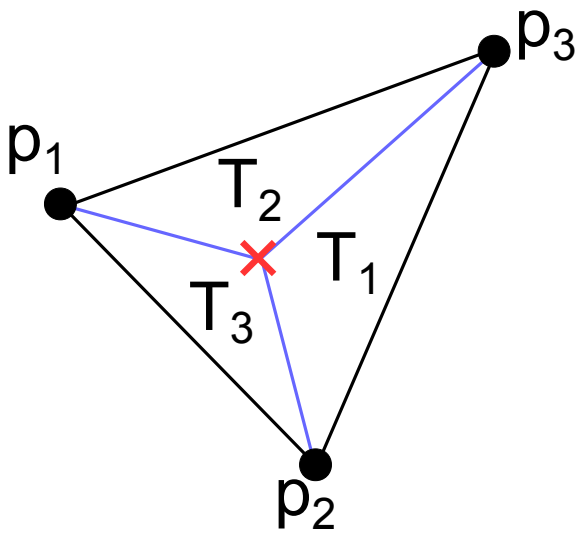

Figure 5.12.: Illustration of the determination of barycentric coordinates in a triangle. The weight factors in equation (5.18) are given by the ratio of the areas of the triangles T_1, T_2 and T_3 and the surface area A_{tri} of the black tiangle, embedding the detected ion impact position (red cross).

(the whole data set contained approximately 600.000 atoms). In this example calculation, the emitter surface has been lifted rigidly according to equation (4.8), since the scheme for the local lift of the surface presented in section 4.1.4 cannot be directly applied in the absence of rotational symmetry. As the light blue bar in figures 5.13a) and b) indicates, the width of the reconstructed cylinders varies significantly in both volumes. For the new approach, the width amounts to 17.1 nm, whereas the point projection approach delivers a width of 19.5 nm. As it can be seen in figure 5.6, the correct width is given by 16 nm.

A further look at the local atomic density in both reconstructions supports the beneficial influence of the improved surface shape calculation included in the here presented approach. In figure 5.14, a slice through both reconstructions from figure 5.13 is shown. The atoms are colored according to the local atomic density at their respective position inside the volume. In figure 5.15, the local density along the direction defined by the black arrow in figure 5.6 is shown for both reconstructions. As it can be seen in figure 5.14b) and figure 5.15, the conventional point projection approach yields a reconstructed volume with a significantly lower atomic density in the cylinder volume, caused by local magnification. In addition, the atomic density is increased in the center, next to the cylinder containing the type 2 atoms, which is another consequence of the local magnification effect. In contrast to this observation, the reconstruction in figure 5.14a), representing the result of the here presented technique, has a much more homogeneous atomic density close to the desired value of 6 atoms per cubic nanometer. Especially in the cylinder containing the type 2 atoms, the density does not drop as severely as in the case of the conventional reconstruction

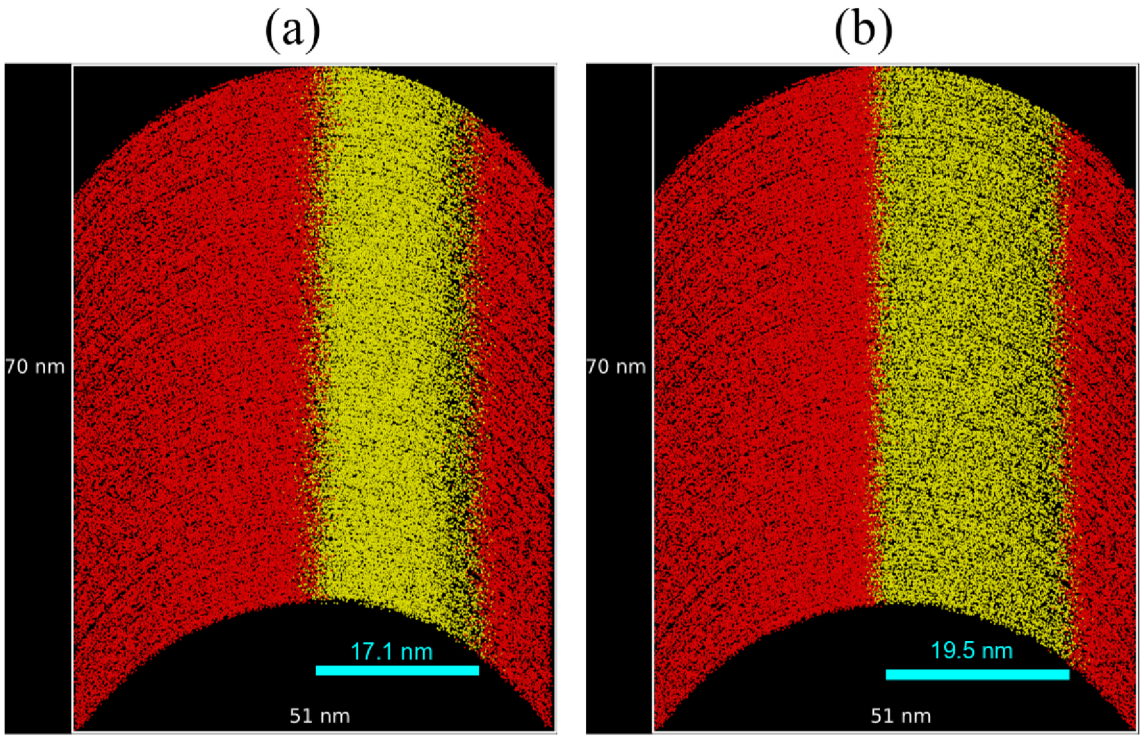

Figure 5.13.: Slice through the center of the reconstruction of the emitter structure shown in figure 5.6. In (a), the result achieved by the application of the here presented technique is shown. For comparison, the result of the point projection approach is given in (b).

approach (red curve in figure 5.15). Apart from two very narrow regions at the interface between matrix and cylinder, the density has been impressively improved. The density drop at the interface might be reduced by a refinement of the discretization of the mesh on the detector. To some extend it is also caused by trajectory overlaps, which cannot be taken into account.

It has to be mentioned that the density in both volumes is overall slightly too low (the target value is given by 6 atoms per cubic nanometer). In figure 5.15 it can be seen that the density drops at the edge of the volume, which can be explained by the missing atoms beyond the surface of the tip volume. But also in the center, the local density is lower than 6 atoms per cubic nanometer. This deviation from the original atomic density might be caused by the choice of the boundary condition in the calculation of the emitter shape. The assumption of a constant curvature outside the field-of-view probably leads to a slight broadening of the reconstructed volume, which consequently yields a decreased atomic density. In the future, a more suitable choice regarding the boundary condition can be expected to deliver a more accurate atomic density.

Nevertheless, it turns out that the here presented approach improves the reconstruction in terms of the reduction of local magnification effects caused by the varying evaporation

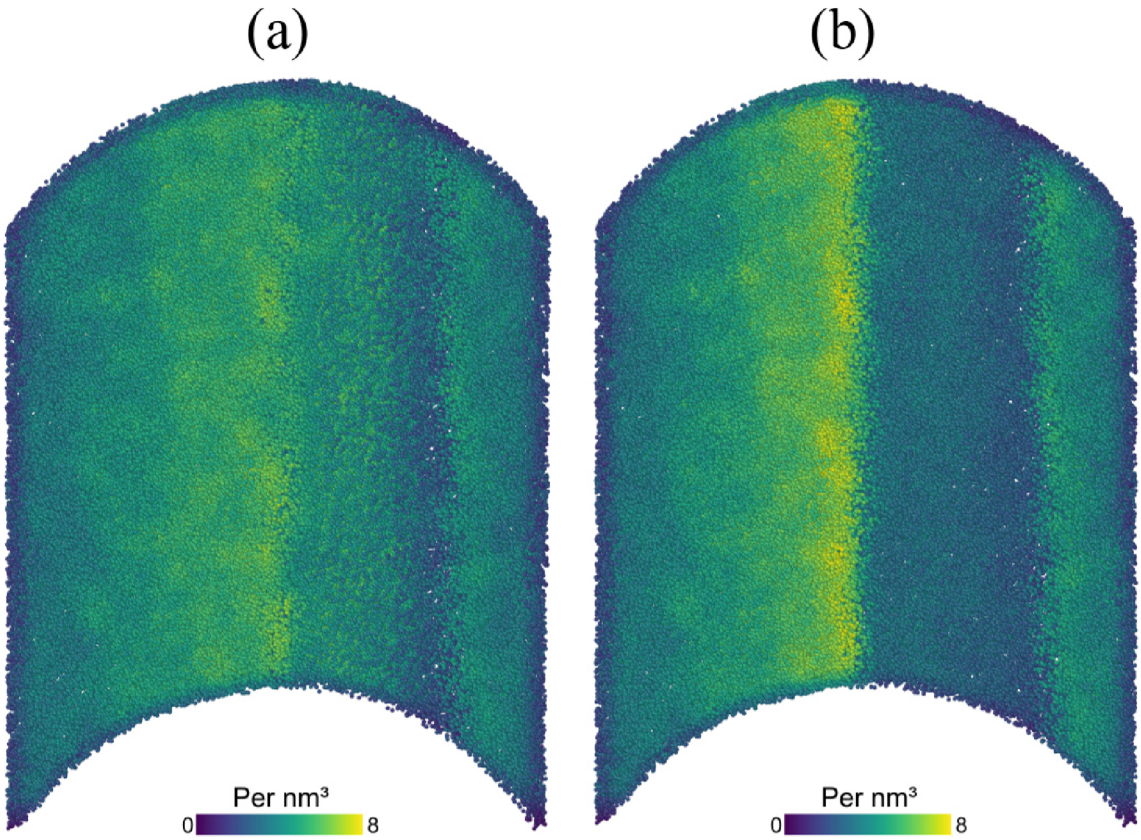

Figure 5.14.: Comparison of the atomic density in the reconstructed asymmetric volumes. In (a), the result of the reconstruction technique, introduced in this chapter is shown. The result for the conventional point projection algorithm is illustrated in (b).

fields. The remaining difference in the lateral size of the cylinder most probably stems from the discretization of the detector and the surface. This discretization might be further refined, but a refinement is naturally limited by the increase of noise in the local density of detected events. Furthermore, the boundary condition with a constant Gaussian curvature outside the field-of-view is possibly too simple. At this moment, a general concept for a suitable boundary condition does not exist yet. To this end, one would have to develop a reasonable boundary condition for every case, in order to achieve reasonable results. For example, the constant curvature condition outside the field-of-view might be replaced by a linearly increasing/decreasing curvature, which approaches the value of a perfect cylinder towards the outer edge of the volume.

Of course, it might also be possible to solve this problem on the experimental side. If future atom probe designs would have a larger field-of-view, it might be possible to learn more about the requirements for the boundary condition. In addition, the enlargement of the field-of-view would probably also reduce the influence of the boundary condition on the surface calculation.

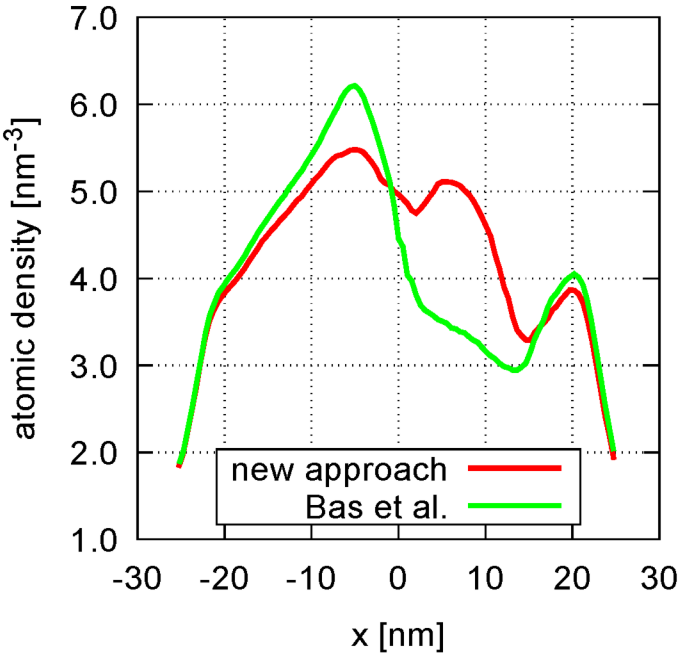

Figure 5.15.: Local atomic density for both reconstructions in figure 5.13 along the direction given by the black arrow in figure 5.6b). The densities have been obtained in a cylindrical volume with a radius of 10 nm.

Similar to the concept presented in section 4.1.4, a further improvement of the atomic density distribution in the reconstructed volume could be achieved by lifting the emitter surface locally, but keeping the orientation of an individual surface segment fixed. In the general case, these surface segments can no longer be described by rings. Due to the lack of symmetry, the surface needs to be described as a composition of small pieces with the shape of a trapezoid (see figure 5.5). This modification makes the realization of a local lift concept more complex. In order to avoid extremely large fluctuations regarding the height of neighboring segments, the area of the cross section of an individual surface segment should not become too small. Such a concept has not yet been implemented, but since it yields a significant improvement of the reconstruction in the rotationally symmetric case, similar improvements can also be expected for a general atom probe tip.

By the time of this work, the issue of ambiguity is still a challenge. For some exceptional cases, it cannot be excluded that a particular detector pattern can be "produced" by only one well-defined field emitter with a characteristic shape, or if their might be more than one emitter shape yielding a specific density distribution on the detector. Numerical experiments carried out in the course of this study at least indicate that significantly different emitter shapes might yield very similar density distributions in some situations. For example, in the case of tips with an elliptical shape, the density distributions achieved

by different tip shapes might be difficult to distinguish. To this end, a further criterion beside the local density of measured events on the detector might be needed in these rare exceptional cases, in order to extract a reasonable description of the tip surface from the measurement data.

Another open question is the possible consideration of calculated ion trajectories in the reconstruction approach. Since it has been observed that effects caused by trajectory overlaps can be repaired to some extent with the help of calculated ion trajectories, a more complete technique should somehow include this feature.

One possibility might be the usage of trajectories in order to replace the projection of the surface normals onto the detector, in order to observe the Delaunay mesh as it is shown in figure 5.11. In this way, the problem of a rising instability of the reconstruction might be sufficiently tamed, since the underlying surface is relatively smooth and extreme deflections should be avoided. The trajectories could be expected to improve the volume reconstruction slightly, especially in the vicinity of material interfaces.

Furthermore, the determination of the optimum sampling parameters N_P and N_R is requiring a clear strategy. In the presented example cases, it turned out that a relatively small value for N_R is beneficial for the later reconstruction. However, a universal recipe regarding the choice of these parameters is still not known.

Chapter 6.

Summary

In this work a new reconstruction algorithm for the evaluation of atom probe tomography data has been developed. The development process was split up into several different parts.

In a first test stage described in chapter 3, it was confirmed that the simulated field evaporation process can be inverted by calculating realistic ion trajectories starting from various positions on the current emitter surface. The possibility to perform a reconstruction in a reversed form starting with the last detected atoms could be confirmed in section 3.1 for two very typical emitter structures, namely a layer structure and a structure containing a spherical particle. In a first approach, the reconstruction has been done on a rigid lattice, where a predefined selection of possible three-dimensional coordinates existed in each reconstruction step. In this way, the possibility of misplacing an atom was effectively discretized, which means that an atom could either be positioned at the exact former position in the lattice or it could have been placed at one of the immediate neighbor positions.

Since this selection of predefined candidate positions cannot be easily made in the general case without any information about the lattice structure of the specimen, the reconstruction technique was enhanced in section 3.2. At this stage, the algorithm was allowed to position the atoms everywhere on the tip surface without the restriction of a discretized lattice. Due to numerical inaccuracies, which are inevitable to some extent, this approach delivered unphysical results as it can be seen in figure 3.5. In order to avoid the appearance of strong surface roughness and self-amplifying protrusions, a guidance was needed, informing the algorithm about the quality of a possible reconstruction site.

To this end, a simple Lennard-Jones potential has been used in order to identify surface position with a high number of neighboring atoms. In the following reconstruction step, the algorithm choses the final resulting position from this set of local minimum values of the inter-atomic potential. The application of this improved technique delivered very promising results for small emitter structures as shown in figures 3.9 and 3.10. Despite the severe difference regarding the evaporation fields of the involved atomic species, the layer structure as well as the spherical precipitate could be reconstructed successfully. In addition, it

turned out that the former fcc lattice structure could be recovered, even in the case of the layer structure in figure 3.9, where the information got lost in the very beginning of the reconstruction process (the bottom of the reconstructed volume respectively). Nevertheless, a further investigation of the effect of the limited detector efficiency on the reconstruction revealed serious challenges. The reconstructed volume of the precipitate structure from figure 3.10, observed after randomly removing only 1% of the detected atoms from the data set, already appears to be strongly distorted. The particle is still visible but the lattice structure is already affected very strongly by the missing information, since the fcc structure is lost, even at regions located pretty deep inside the bulk (see figure 3.10d)). Given the fact that the detector efficiency in a realistic atom probe experiment is in the range of 50% – 80%, dealing with the issue of missing atoms in the data set seems to be a very complicated if not impossible challenge. In addition, the computational effort of the improved technique presented in section 3.2 is to high by the time of this study, since the amount of data from an APT measurement could easily reach numbers of a few hundred million atoms.

Therefore, the second larger part of this thesis worked towards an alternative approach, which is simply faster and less sensitive to missing information. In a first step, a complete solution for a special kind of emitter structures could be developed. It is exclusively intended to be applied to emitter structures given a rotational symmetry regarding the tip axis. The approach doesn't include the calculation of ion trajectories and simply assumes a projection law for the ions according to equation (4.1). The most important difference between this approach and the point projection approach by Bas and coworkers is the capability of identifying a reasonable emitter surface shape with the help of the measured event density on the detector. In other words, this technique is no longer based on the assumption of a constant spherical emitter shape.

The surface is composed of a fixed number of pieces (rings) with a constant orientation angle for which the lateral size needs to be adjusted according to the local detector density. The procedure of building a reasonable description for the tip surface is performed several times for different portions of data with a predefined size, which ensures the consideration of changes regarding the emitter shape during field evaporation.

In a first version of this approach, the whole emitter surface is shifted upwards after each reconstructed atom and the final atom position is defined by the equations (4.5), (4.6) and (4.7). The approach turned out to represent a remarkable improvement of the reconstruction of an amorphous structure with a spherical particle with either a substantially lower or higher evaporation field than the surrounding matrix. The size aspect ratio of the particle could be recovered impressively well in all cases, especially in direct comparison with the result of the traditional point projection approach (see figures 4.7 and 4.8).

Nevertheless, the atomic density of the reconstructed volume still varied significantly in the vicinity of the particle/matrix interface. The reason for these density fluctuations is most probably the assumption of a steady state of the tip shape, which is clearly not true during a transition stage, when the particle covers a growing (or shrinking) amount of the full emitter surface.

Therefore, the approach has finally been improved in order to better account for these transition situations occurring during field evaporation. The calculated emitter profiles, initially intended to be rigid, were broken up. Consequently, each segment of the height profile was allowed to be lifted independently and just according to its lateral size and the amount of associated detected material. Meanwhile, the orientation angle of each segment is kept constant. This approach can be seen as a compromise because on the one hand, it slightly contradicts the basic concept of the new approach, but on the other hand, it turned out to improve the homogeneity of the atomic density drastically as it is illustrated for example in figure 4.14.

The outlined reconstruction approach is sufficiently fast, which means it could routinely be used for the reconstruction of experimental data sets with an expected rotational symmetry (for example layer structures). This has been shown for the experimental example of a Cu/AlN layer structure in section 4.1.7. Even the well-known experimental challenge of a limited detector efficiency (typically in the range between fifty to eighty percent) does not diminish the capability of the technique to deliver reliable reconstructions. This claim is supported by numerical experiments carried out in section 4.1.6.

Lastly, the limitation of the algorithm to emitter structures with rotational/axial symmetry has been overcome in section 5.1. A new approach for general tip structures has been developed. This technique also calculates the emitter surface profile from the local event density on the detector. In contrast to the rotational symmetry approach, this technique uses a direct relation between the local event density and the Gaussian curvature of the emitter surface in a particular angular direction.

With the help of a finite difference method, the required Gaussian curvature is iteratively set at each surface position. This iterative procedure yields a reasonable result for the description of the emitter surface. The final reconstruction can be performed by the linear projection of the the normal vectors on the calculated surface onto the detector. The intersections of these projection lines with the detector plane yield a mesh, which can be connected by Delaunay triangles. Finally, for every detected ion, the surrounding triangle is identified and the position of the detected atom in the reconstructed volume is given by a weighted sum of the surface nodes belonging to the corresponding Delaunay triangle on the detector.

In summary, the presented reconstruction technique can be judged as a significant

improvement. Apart from minor adjustments, e.g. the issue of a local lift of the emitter volume in the final reconstruction approach described in section 5.1, the algorithm is ready to be used as a new standard technique. Once these refinements have been done, the conventional point projection approach can be fully replaced by the new concept and the issue of local magnification effects and strong density fluctuations could be drastically reduced in practical atom probe work.

Bibliography

[1]T. Tsong, S. McLane, and T. Kinkus, "Pulsed-laser time-of-flight atom-probe field ion microscope", Review of Scientific Instruments **53**, 1442–1448 (1982).

[2]G. Kellogg, and T. Tsong, "Pulsed-laser atom-probe field-ion microscopy", Journal of Applied Physics **51**, 1184–1193 (1980).

[3]A. Cerezo, P. H. Clifton, M. J. Galtrey, C. J. Humphreys, T. F. Kelly, D. J. Larson, S. Lozano-Perez, E. A. Marquis, R. A. Oliver, G. Sha, et al., "Atom probe tomography today", Materials Today **10**, 36–42 (2007).

[4]M. Gilbert, W. Vandervorst, S. Koelling, and A. K. Kambham, "Atom probe analysis of a 3d finfet with high-k metal gate", Ultramicroscopy **111**, 530–534 (2011).

[5]J. Barnes, A. Grenier, I. Mouton, S. Barraud, G. Audoit, J. Bogdanowicz, C. Fleischmann, D. Melkonyan, W. Vandervorst, S. Duguay, et al., "Atom probe tomography for advanced nanoelectronic devices: current status and perspectives", Scripta Materialia **148**, 91–97 (2018).

[6]A. K. Kambham, J. Mody, M. Gilbert, S. Koelling, and W. Vandervorst, "Atom-probe for finfet dopant characterization", Ultramicroscopy **111**, 535–539 (2011).

[7]F. Vurpillot, and C. Oberdorfer, "Modeling atom probe tomography: a review", Ultramicroscopy **159**, 202–216 (2015).

[8]C. Oberdorfer, S. M. Eich, and G. Schmitz, "A full-scale simulation approach for atom probe tomography", Ultramicroscopy **128**, 55–67 (2013).

[9]F. Vurpillot, A. Bostel, and D. Blavette, "Trajectory overlaps and local magnification in three-dimensional atom probe", Applied Physics Letters **76**, 3127–3129 (2000).

[10]F. Vurpillot, A. Bostel, E. Cadel, and D. Blavette, "The spatial resolution of 3d atom probe in the investigation of single-phase materials", Ultramicroscopy **84**, 213–224 (2000).

[11]D. Beinke, C. Oberdorfer, and G. Schmitz, "Towards an accurate volume reconstruction in atom probe tomography", Ultramicroscopy **165**, 34–41 (2016).

[12]D. Beinke, and G. Schmitz, "Atom probe reconstruction with a locally varying emitter shape", Microscopy and Microanalysis **25**, 280–287 (2019).

[13]D. Beinke, F. Bürger, and G. Schmitz, "Extracting the shape of nanometric field emitters", Nanoscale (submitted).

[14]E. W. Müller, J. A. Panitz, and S. B. McLane, "The atom-probe field ion microscope", Review of Scientific Instruments **39**, 83–86 (1968).

[15]D. N. Seidman, and K. Stiller, "An atom-probe tomography primer", Mrs Bulletin **34**, 717–724 (2009).

[16]T. Tsong, "Pulsed-laser-stimulated field ion emission from metal and semiconductor surfaces: a time-of-flight study of the formation of atomic, molecular, and cluster ions", Physical Review B **30**, 4946 (1984).

[17]M. K. Miller, and R. G. Forbes, *Atom-probe tomography - the local electrode atom probe* (Springer, New York, Heidelberg, Dordrecht, London, 2014).

[18]B. Gault, M. P. Moody, J. M. Cairney, and S. P. Ringer, *Atom probe microscopy* (Springer Science + Business Media, New York, Heidelberg, Dordrecht, London, 2012).

[19]M. K. Miller, A. Cerezo, and M. G. Hetherington, *Atom probe field ion microscopy* (Clarendon Press, Oxford, 1996).

[20]W. Lefebvre, F. Vurpillot, and X. Sauvage, *Atom probe tomography - put theory into practice*, 1. edition (Academic Press, Amsterdam, Boston, 2016).

[21]D. J. Larson, T. J. Prosa, R. M. Ulfig, B. P. Geiser, T. F. Kelly, and P. S. C. J. Humphreys, *Local electrode atom probe tomography - a user's guide* (Springer Science + Business Media, New York, Heidelberg, Dordrecht, London, 2013).

[22]E. W. Müller, and K. Bahadur, "Field ionization of gases at a metal surface and the resolution of the field ion microscope", Physical Review **102**, 624 (1956).

[23]R. G. Forbes, "Field-ion imaging old and new", Applied surface science **94**, 1–16 (1996).

[24]R. Gomer, "Field desorption", The Journal of Chemical Physics **31**, 341–345 (1959).

[25]R. Gomer, and L. W. Swanson, "Theory of field desorption", The journal of chemical physics **38**, 1613–1629 (1963).

[26]D. Brandon, "On field evaporation", The Philosophical Magazine: A Journal of Theoretical Experimental and Applied Physics **14**, 803–820 (1966).

[27]T. T. Tsong, "On the mechanism of field evaporation", Surface Science **10**, 102–117 (1968).

[28]A. Menand, and D. Blavette, "Temperature dependence of iridium field evaporation rate", Le Journal de Physique Colloques **47**, C7–17 (1986).

[29]D. R. Kingham, "Model calculations of tunnelling and thermal evaporation rate constants relating to field evaporation", Journal of Physics D: Applied Physics **15**, 2537 (1982).

[30]R. G. Forbes, "Charge hopping and charge draining: two mechanisms of field desorption", Surface Science **102**, 255–263 (1981).

[31]C. Sánchez, A. Lozovoi, and A. Alavi, "Field-evaporation from first-principles", Molecular Physics **102**, 1045–1055 (2004).

[32]E. W. Müller, "Field ionization and field ion microscopy", in *Advances in electronics and electron physics*, Vol. 13 (Elsevier, 1960), pp. 83–179.

[33]F. Vurpillot, B. Gault, A. Vella, M. Bouet, and B. Deconihout, "Estimation of the cooling times for a metallic tip under laser illumination", Applied physics letters **88**, 094105 (2006).

[34]J. Panitz, "Imaging atom-probe mass spectroscopy", Progress in Surface Science **8**, 219–262 (1978).

[35]A. Cerezo, T. Godfrey, and G. Smith, "Application of a position-sensitive detector to atom probe microanalysis", Review of Scientific Instruments **59**, 862–866 (1988).

[36]B. Deconihout, A. Bostel, A. Menand, J. Sarrau, M. Bouet, S. Chambreland, and D. Blavette, "On the development of a 3d tomographic atom-probe", Applied surface science **67**, 444–450 (1993).

[37]D. Blavette, B. Deconihout, A. Bostel, J. Sarrau, M. Bouet, and A. Menand, "The tomographic atom probe: a quantitative three-dimensional nanoanalytical instrument on an atomic scale", Review of Scientific Instruments **64**, 2911–2919 (1993).

[38]T. F. Kelly, P. P. Camus, D. J. Larson, L. M. Holzman, and S. S. Bajikar, "On the many advantages of local-electrode atom probes", Ultramicroscopy **62**, 29–42 (1996).

[39]T. F. Kelly, and D. J. Larson, "Local electrode atom probes", Materials Characterization **44**, 59–85 (2000).

[40]P. Stender, C. Oberdorfer, M. Artmeier, P. Pelka, F. Spaleck, and G. Schmitz, "New tomographic atom probe at university of muenster, germany", Ultramicroscopy **107**, 726–733 (2007).

[41]R. Schlesiger, C. Oberdorfer, R. Würz, G. Greiwe, P. Stender, M. Artmeier, P. Pelka, F. Spaleck, and G. Schmitz, "Design of a laser-assisted tomographic atom probe at münster university", Review of Scientific Instruments **81**, 043703 (2010).

[42]B. Gault, F. Vurpillot, A. Vella, M. Gilbert, A. Menand, D. Blavette, and B. Deconihout, "Design of a femtosecond laser assisted tomographic atom probe", Review of Scientific Instruments **77**, 043705 (2006).

[43]R. Smith, and J. Walls, "Ion trajectories in the field-ion microscope", Journal of Physics D: Applied Physics **11**, 409 (1978).

[44]A. Vella, "On the interaction of an ultra-fast laser with a nanometric tip by laser assisted atom probe tomography: a review", Ultramicroscopy **132**, 5–18 (2013).

[45]A. Cerezo, P. H. Clifton, S. Lozano-Perez, P. Panayi, G. Sha, and G. D. Smith, "Overview: recent progress in three-dimensional atom probe instruments and applications", Microscopy and microanalysis **13**, 408–417 (2007).

[46]P. Bas, A. Bostel, B. Deconihout, and D. Blavette, "A general protocol for the reconstruction of 3d atom probe data", Applied Surface Science **87**, 298–304 (1995).

[47]F. Vurpillot, A. Bostel, and D. Blavette, "The shape of field emitters and the ion trajectories in three-dimensional atom probes", Journal of microscopy **196**, 332–336 (1999).

[48]S. Gerstl, B. Geiser, T. Kelly, and D. Larson, "Evaluation of local radii of atom-probe-tomography specimens", Microscopy and Microanalysis **15**, 248–249 (2009).

[49]A. Shariq, S. Mutas, K. Wedderhoff, C. Klein, H. Hortenbach, S. Teichert, P. Kücher, and S. Gerstl, "Investigations of field-evaporated end forms in voltage-and laser-pulsed atom probe tomography", Ultramicroscopy **109**, 472–479 (2009).

[50]D. Larson, B. Geiser, T. Prosa, R. Ulfig, and T. Kelly, "Non-tangential continuity reconstruction in atom probe tomography data", Microscopy and Microanalysis **17**, 740–741 (2011).

[51]B. Geiser, D. Larson, E. Oltman, S. Gerstl, D. Reinhard, T. Kelly, and T. Prosa, "Wide-field-of-view atom probe reconstruction", Microscopy and Microanalysis **15**, 292–293 (2009).

[52]B. Gault, D. Haley, F. De Geuser, M. Moody, E. Marquis, D. Larson, and B. Geiser, "Advances in the reconstruction of atom probe tomography data", Ultramicroscopy **111**, 448–457 (2011).

[53]S. Walck, T. Buyuklimanli, and J. Hren, "Extended depth profiling with the iap", Le Journal de Physique Colloques **47**, C2–451 (1986).

[54]F. Vurpillot, D. Larson, and A. Cerezo, "Improvement of multilayer analyses with a three-dimensional atom probe", Surface and Interface Analysis: An International Journal devoted to the development and application of techniques for the analysis of surfaces, interfaces and thin films **36**, 552–558 (2004).

[55]F. De Geuser, W. Lefebvre, F. Danoix, F. Vurpillot, B. Forbord, and D. Blavette, "An improved reconstruction procedure for the correction of local magnification effects in three-dimensional atom-probe", Surface and Interface Analysis: An International Journal devoted to the development and application of techniques for the analysis of surfaces, interfaces and thin films **39**, 268–272 (2007).

[56]D. J. Larson, B. Gault, B. P. Geiser, F. De Geuser, and F. Vurpillot, "Atom probe tomography spatial reconstruction: status and directions", Current Opinion in Solid State and Materials Science **17**, 236–247 (2013).

[57]F. Vurpillot, B. Gault, B. P. Geiser, and D. Larson, "Reconstructing atom probe data: a review", Ultramicroscopy **132**, 19–30 (2013).

[58]B. Gault, M. P. Moody, F. de Geuser, G. Tsafnat, A. La Fontaine, L. T. Stephenson, D. Haley, and S. P. Ringer, "Advances in the calibration of atom probe tomographic reconstruction", Journal of Applied Physics **105**, 034913 (2009).

[59]B. Gault, F. De Geuser, L. T. Stephenson, M. P. Moody, B. C. Muddle, and S. P. Ringer, "Estimation of the reconstruction parameters for atom probe tomography", Microscopy and Microanalysis **14**, 296–305 (2008).

[60]S. T. Loi, B. Gault, S. P. Ringer, D. J. Larson, and B. P. Geiser, "Electrostatic simulations of a local electrode atom probe: the dependence of tomographic reconstruction parameters on specimen and microscope geometry", Ultramicroscopy **132**, 107–113 (2013).

[61]S. K. Suram, and K. Rajan, "Calibration of reconstruction parameters in atom probe tomography using a single crystallographic orientation", Ultramicroscopy **132**, 136–142 (2013).

[62]D. Haley, T. Petersen, S. Ringer, and G. Smith, "Atom probe trajectory mapping using experimental tip shape measurements", Journal of microscopy **244**, 170–180 (2011).

[63]I. Mouton, T. Printemps, A. Grenier, N. Gambacorti, E. Pinna, M. Tiddia, A. Vacca, and G. Mula, "Toward an accurate quantification in atom probe tomography reconstruction by correlative electron tomography approach on nanoporous materials", Ultramicroscopy **182**, 112–117 (2017).

[64]P. Felfer, and J. Cairney, "A computational geometry framework for the optimisation of atom probe reconstructions", Ultramicroscopy **169**, 62–68 (2016).

[65]D. F. Watson, "Computing the n-dimensional delaunay tessellation with application to voronoi polytopes", The computer journal **24**, 167–172 (1981).

[66]C. Oberdorfer, and G. Schmitz, "On the field evaporation behavior of dielectric materials in three-dimensional atom probe: a numeric simulation", Microscopy and Microanalysis **17**, 15–25 (2011).

[67]N. Rolland, F. Vurpillot, S. Duguay, and D. Blavette, "A meshless algorithm to model field evaporation in atom probe tomography", Microscopy and Microanalysis **21**, 1649–1656 (2015).

[68]G. Robin, "Sur la distribution de l'électricité à la surface des conducteurs fermés des conducteurs ouverts", in Annales scientifiques de l'école normale supérieure, Vol. 3 (1886), pp. 3–58.

[69]H. Kreuzer, L. Wang, and N. Lang, "Self-consistent calculation of atomic adsorption on metals in high electric fields", Physical Review B **45**, 12050 (1992).

[70]T. Ono, T. Sasaki, J. Otsuka, and K. Hirose, "First-principles study on field evaporation of surface atoms from w (0 1 1) and mo (0 1 1) surfaces", Surface science **577**, 42–46 (2005).

[71]C. Oberdorfer, S. M. Eich, M. Lütkemeyer, and G. Schmitz, "Applications of a versatile modelling approach to 3d atom probe simulations", Ultramicroscopy **159**, 184–194 (2015).

[72]J. R. Cash, and A. H. Karp, "A variable order runge-kutta method for initial value problems with rapidly varying right-hand sides", ACM Transactions on Mathematical Software (TOMS) **16**, 201–222 (1990).

[73]M. P. Moody, B. Gault, L. T. Stephenson, R. K. Marceau, R. C. Powles, A. V. Ceguerra, A. J. Breen, and S. P. Ringer, "Lattice rectification in atom probe tomography: toward true three-dimensional atomic microscopy", Microscopy and Microanalysis **17**, 226–239 (2011).

[74]A. J. Breen, M. P. Moody, A. V. Ceguerra, B. Gault, V. J. Araullo-Peters, and S. P. Ringer, "Restoring the lattice of si-based atom probe reconstructions for enhanced information on dopant positioning", Ultramicroscopy **159**, 314–323 (2015).

[75]B. P. Geiser, T. F. Kelly, D. J. Larson, J. Schneir, and J. P. Roberts, "Spatial distribution maps for atom probe tomography", Microscopy and Microanalysis **13**, 437–447 (2007).

[76]J. A. Nelder, and R. Mead, "A simplex method for function minimization", The computer journal **7**, 308–313 (1965).

[77]E. Stiefel, "Über einige methoden der relaxationsrechnung", Zeitschrift für angewandte Mathematik und Physik ZAMP **3**, 1–33 (1952).

[78]A. Stukowski, "Visualization and analysis of atomistic simulation data with ovito–the open visualization tool", Modelling and Simulation in Materials Science and Engineering **18**, 015012 (2009).

[79]J. D. Honeycutt, and H. C. Andersen, "Molecular dynamics study of melting and freezing of small lennard-jones clusters", Journal of Physical Chemistry **91**, 4950–4963 (1987).

[80]D. Faken, and H. Jónsson, "Systematic analysis of local atomic structure combined with 3d computer graphics", Computational Materials Science **2**, 279–286 (1994).

[81]C. Kittel, *Introduction to solid state physics*, 8. edition (Wiley, New York, 2004).

[82]A. Cerezo, P. Warren, and G. Smith, "Some aspects of image projection in the field-ion microscope", Ultramicroscopy **79**, 251–257 (1999).

[83]T. Al-Kassab, H. Wollenberger, G. Schmitz, and R. Kirchheim, "Tomography by atom probe field ion microscopy", in *High-resolution imaging and spectrometry of materials* (Springer, 2003), pp. 271–320.

[84]F. De Geuser, and B. Gault, "Reflections on the projection of ions in atom probe tomography", Microscopy and Microanalysis **23**, 238–246 (2017).

[85]N. Rolland, F. Vurpillot, S. Duguay, and D. Blavette, "Dynamic evolution and fracture of multilayer field emitters in atom probe tomography: a new interpretation", The European Physical Journal Applied Physics **72**, 21001 (2015).

[86]F. Vurpillot, A. Cerezo, D. Blavette, and D. Larson, "Modeling image distortions in 3dap", Microscopy and Microanalysis **10**, 384–390 (2004).

[87]F. Vurpillot, M. Gruber, G. Da Costa, I. Martin, L. Renaud, and A. Bostel, "Pragmatic reconstruction methods in atom probe tomography", Ultramicroscopy **111**, 1286–1294 (2011).

[88]D. J. Larson, B. P. Geiser, T. J. Prosa, and T. F. Kelly, "On the use of simulated field-evaporated specimen apex shapes in atom probe tomography data reconstruction", Microscopy and Microanalysis **18**, 953–963 (2012).

[89]D. Larson, B. Geiser, T. Prosa, and T. Kelly, "Toward automated optimization of reconstruction of atom probe data", Microscopy and Microanalysis **17**, 724–725 (2011).

[90]D. Larson, T. Prosa, B. Geiser, and W. Egelhoff Jr, "Effect of analysis direction on the measurement of interfacial mixing in thin metal layers with atom probe tomography", Ultramicroscopy **111**, 506–511 (2011).

[91]T. Jeske, and G. Schmitz, "Influence of the microstructure on the interreaction of al/ni investigated by tomographic atom probe", Materials Science and Engineering: A **327**, 101–108 (2002).

[92]D. Larson, A. Petford-Long, A. Cerezo, and G. Smith, "Three-dimensional atom probe studies of metallic multilayers", Acta materialia **47**, 4019–4024 (1999).

[93]E. Marquis, B. Geiser, T. J. Prosa, and D. Larson, "Evolution of tip shape during field evaporation of complex multilayer structures", Journal of microscopy **241**, 225–233 (2011).

[94]N. Rolland, F. Vurpillot, S. Duguay, B. Mazumder, J. S. Speck, and D. Blavette, "New atom probe tomography reconstruction algorithm for multilayered samples: beyond the hemispherical constraint", Microscopy and Microanalysis **23**, 247–254 (2017).

[95]D. Larson, B. Geiser, T. Prosa, S. Gerstl, D. Reinhard, and T. Kelly, "Improvements in planar feature reconstructions in atom probe tomography", Journal of Microscopy **243**, 15–30 (2011).

[96]B. Gault, S. T. Loi, V. J. Araullo-Peters, L. T. Stephenson, M. P. Moody, S. L. Shrestha, R. K. Marceau, L. Yao, J. M. Cairney, and S. P. Ringer, "Dynamic reconstruction for atom probe tomography", Ultramicroscopy **111**, 1619–1624 (2011).

[97]S. Koelling, N. Innocenti, A. Schulze, M. Gilbert, A. Kambham, and W. Vandervorst, "In-situ observation of non-hemispherical tip shape formation during laser-assisted atom probe tomography", Journal of Applied Physics **109**, 104909 (2011).

[98]E. Abbena, S. Salamon, and A. Gray, *Modern differential geometry of curves and surfaces with mathematica* (Chapman and Hall/CRC, 2017).

Appendix A.

Geometric reconstruction of important example structures

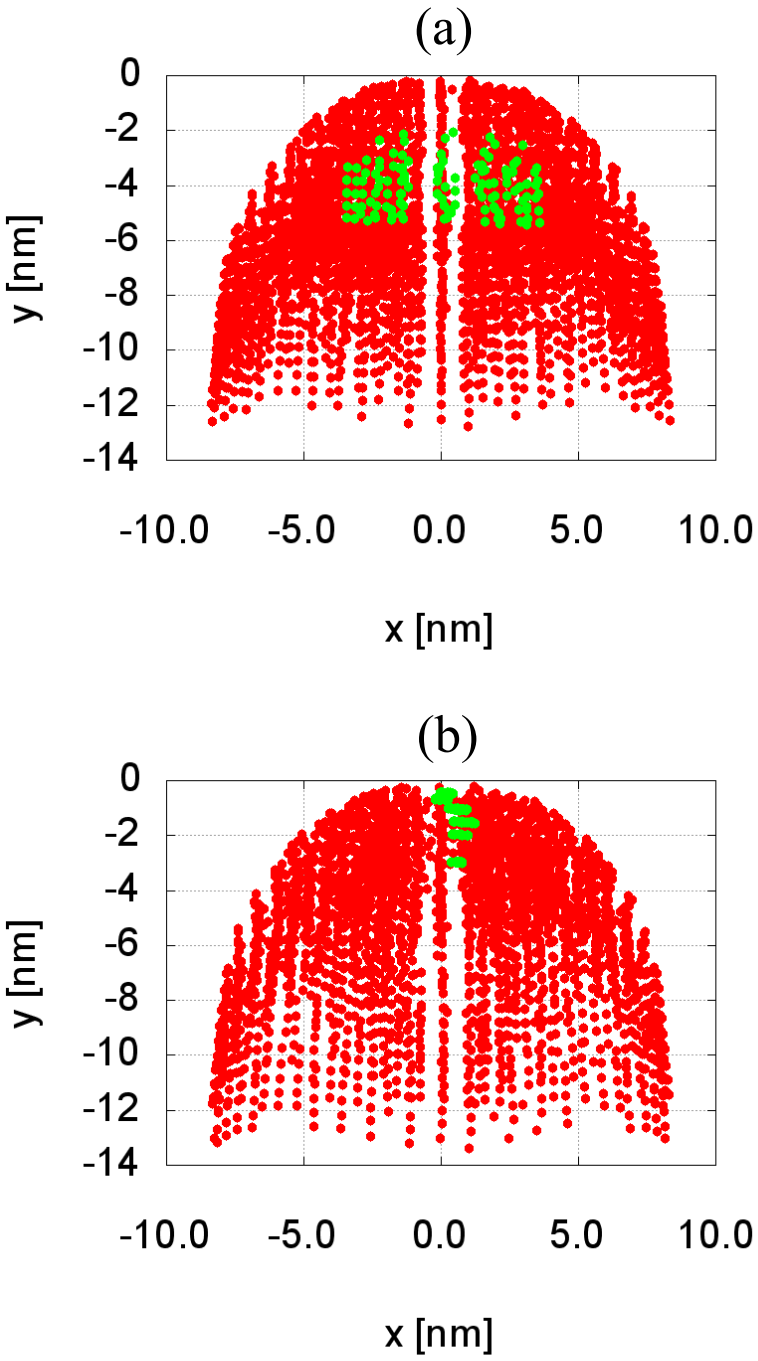

Figure A.1.: Results for the reconstruction after applying the standard geometric approach to the precipitate structure shown in fig. 3.2 for the high field precipitate case in a), and the low field precipitate case in b).

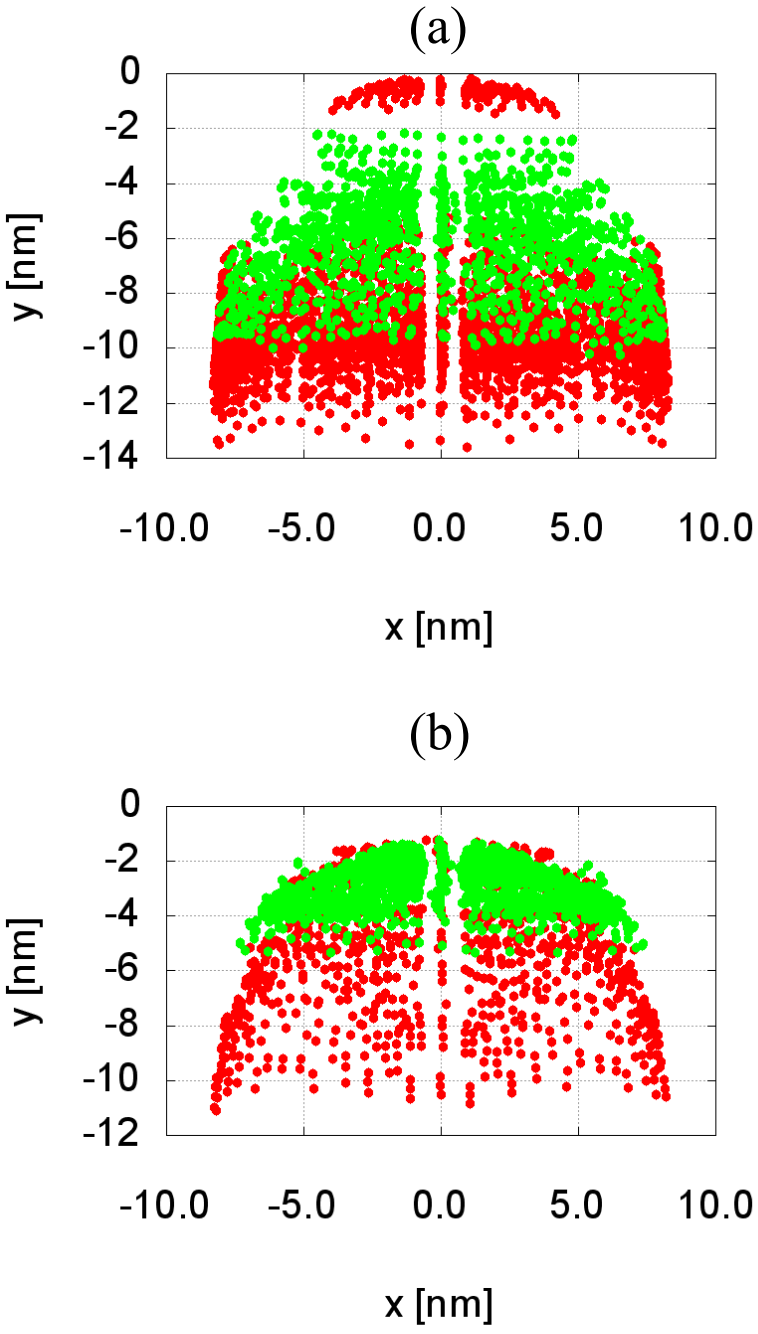

Figure A.2.: Results for the reconstruction of the layer structure shown in fig. 3.2 for the high field case in a), and the low field case in b).

Appendix B.

Influence of the limited detector efficiency

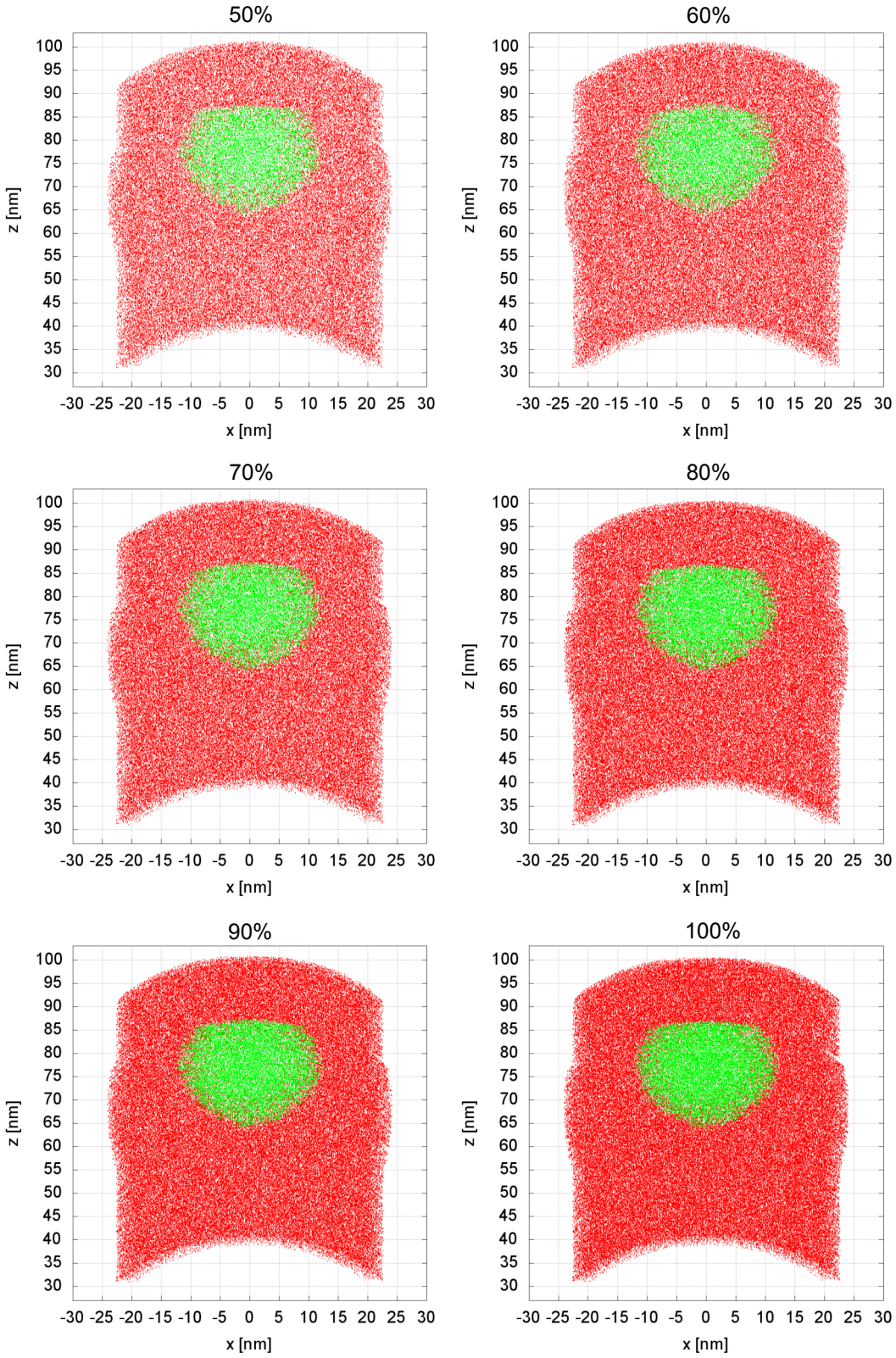

Figure B.1.: Reconstructions for different detector efficiencies in the low field case described in 4.1.6.

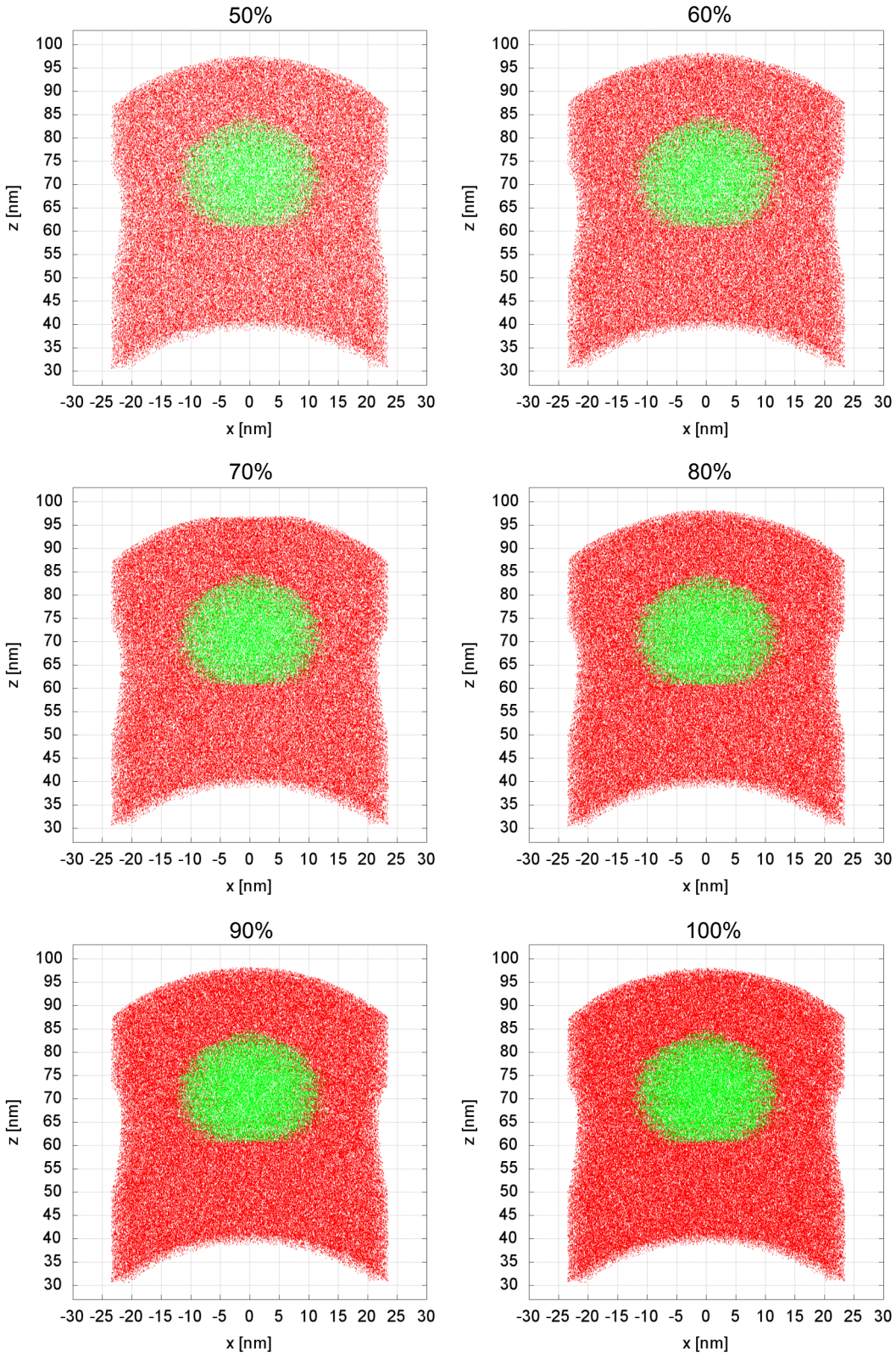

Figure B.2.: Reconstructions for different detector efficiencies in the high field case described in 4.1.6.

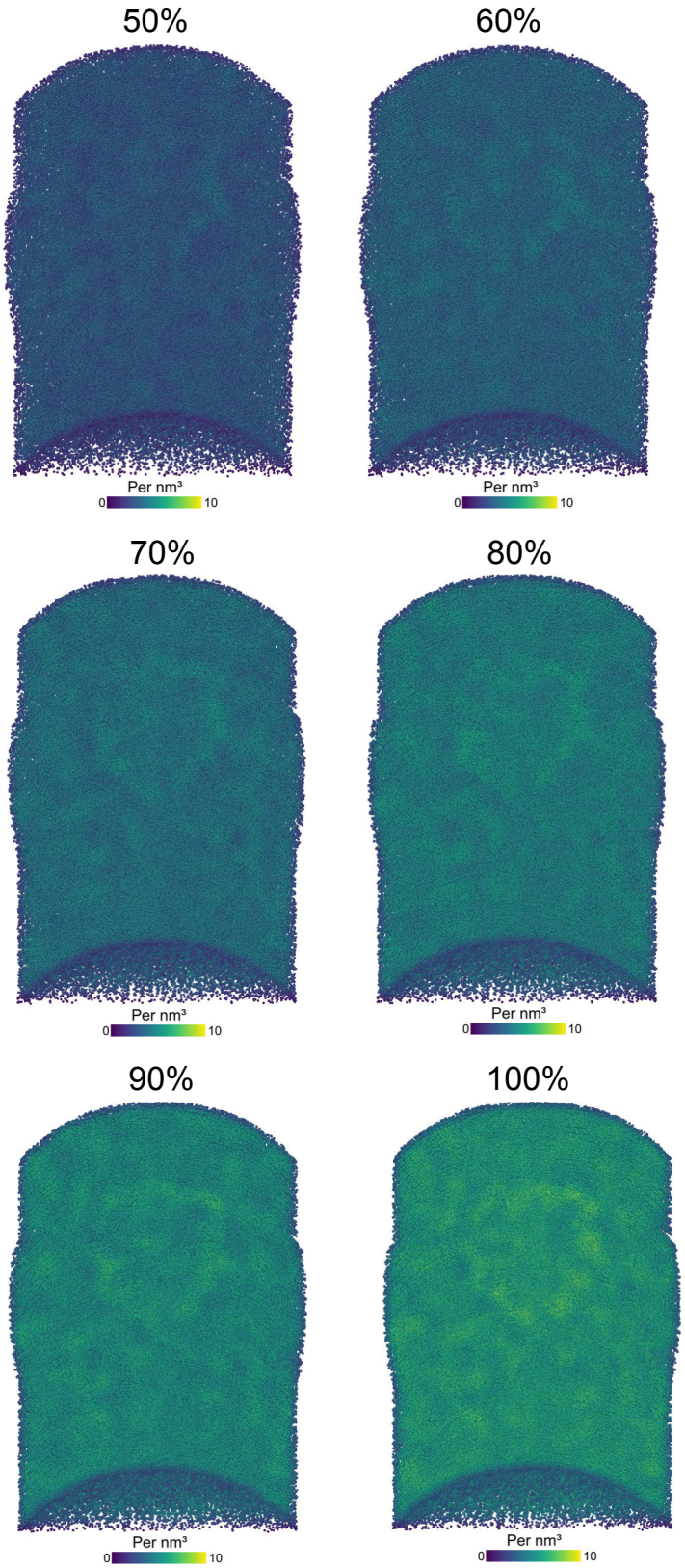

Figure B.3.: Atomic densities for the reconstructed volumes in the low field case described in 4.1.6.

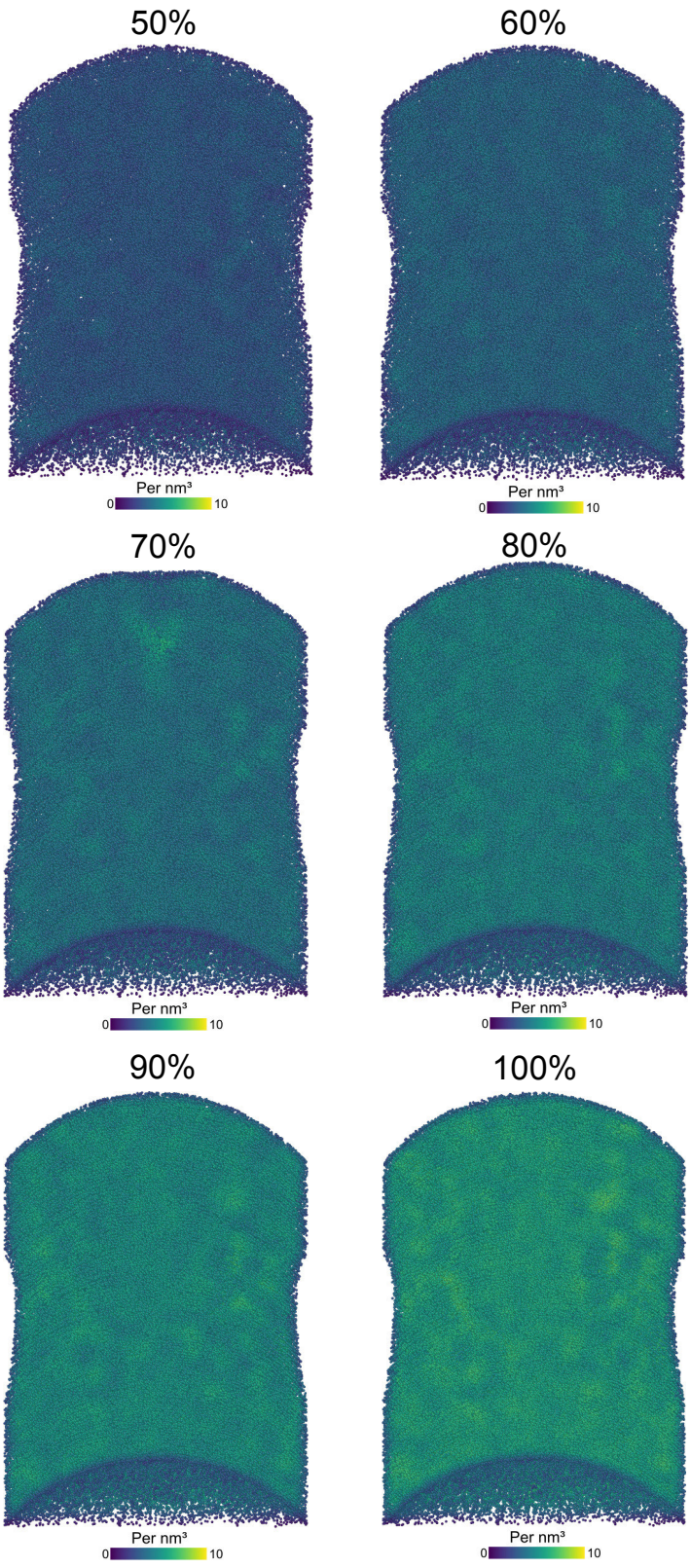

Figure B.4.: Atomic densities for the reconstructed volumes in the high field case described in 4.1.6.